

5 Optical design

5.1 Description

Responsible: WP3 coordinator, A. Freise

Put here the description of the content of the section ...

5.2 Executive Summary

Responsible: WP3 coordinator, A. Freise

Put here a summary of the main achievement/statements of this section ...

5.3 Review on the geometry of the observatory

Author(s): Andreas Freise, Stefan Hild

This section briefly reviews the reasoning behind the shape of current gravitational wave detectors and then discusses alternative geometries which can be of interest for third-generation detectors. We will use the terminology introduced in the review of a triangular configuration [220] and discriminate between the *geometry*, *topology* and *configuration* of a detector as follows:

- The *geometry* describes the position information of one or several interferometers, defined by the number of interferometers, their location and relative orientation.
- The *topology* describes the optical system formed by its core elements. The most common examples are the Michelson, Sagnac and Mach-Zehnder topologies.
- Finally the *configuration* describes the detail of the optical layout and the set of parameters that can be changed for a given topology, ranging from the specifications of the optical core elements to the control systems, including the operation point of the main interferometer. Please note that the addition of optical components to a given topology is often referred to as a change in configuration.

5.3.1 The L-shape

Current gravitational wave detectors represent the most precise instruments for measuring length changes. They are laser interferometers with km-long arms and are operated differently from many precision instruments built for measuring an absolute length. Viewed from above they resemble an L-shape with equal arm length. This geometric form follows directly from the nature of gravitational waves: gravitational waves are transverse, quadrupole waves, thus a change measured along any axis occurs with opposit sign along the axis orthogonal to the previous and the direction of propagation. This key feature allows to make a differential measurement between two orthogonal interferometer arms, yielding twice the amplitude of a single arm. More importantly a differential measurement allows us to potentially discriminate between gravitational wave signals and those types of noise common to both arms, such as, for example, laser amplitude noise. To achieve this the interferometer arms generally have to have approximately the same length. The most simple L-shaped interferometer allowing to do this type of measurement is the symmetric Michelson interferometer, on whose topology all current interferometric detectors are based.

The long arm length of the detectors represents the simplest way to increase the signal-to-noise ratio in the detector because the 'tidal' effect of the gravitational wave increases with the base length over which the measurement is taken, while the fundamental noises are connected to the interaction of light with the optical components or the photo detection and thus do not scale with the length of the interferometer arms. We can summarise, provided specifications of the vacuum system housing the interferometer and the performance of

mirror position control systems are good enough, an increase in arm length will increase the sensitivity of the detector proportionally.

Using the framework developed in [286] we can compute the sensitivity of a laser interferometer with two arms to gravitational waves, taking into account the geometry of the detector, the location of the source and the changes of both over time. The equations show directly that the arms of the detector do not have to be perpendicular, the right angle, however, provides the maximum response of an ideal detector to gravitational waves, which more generally can be written as

$$h(t) = F_+(t)h_+(t) + F_\times(t)h_\times(t) = \sin \zeta f(t, \psi, \dots) \tag{155}$$

with ζ the opening angle of the interferometer arms, F_+ and F_\times the beam pattern functions and $f(t, \psi, \dots)$ a functions of the remaining parameters describing the geometry (the location of the detector and of the source in space and time and the wave polarisation angle).

In summary we can say that for a gravitational wave of given direction and polarisation, a properly aligned symmetric L-shape is an ideal optical layout for an interferometric detector; the arms should be as long as possible and the sensitivity is maximised for an opening angle of 90° . It should be noted that this does not put severe constraints on the type of interferometer topology used. In fact, most common interferometer types can be used in a form that features two large symmetric arms in an L-shape while potential other interferometer arms or sections are shortened such that they can be considered as part of one corner of the detector.

5.3.2 Interferometer Topologies

To date no laser interferometer topology other than the Michelson has been used for gravitational wave detection. However, some very advanced noise reduction techniques proposed for future detectors are based on topologies of the Sagnac interferometer, the Fox-Smith cavity or the Mach-Zehnder interferometer [158, 160, 184].

It is worth noting that a triangular geometry as discussed above is conceivable with different interferometer topologies. In particular it is possible to use different topologies while maintaining the L-shape of the single interferometers as displayed in figure 143. Therefore, for example, three Sagnac interferometers or three cavities could be used to form a triangle. Such detector designs can provide similar benefits as described above for the triple Michelson geometry so that the triangular geometry is largely independent of the topology of the individual interferometers.

The case for alternative topologies is largely based on ideas for the reduction of quantum noise. In general, the signal-to-noise ratio of a single interferometer is different for each topology, with the actual difference depending also on the type of noise under investigation. However, it is not possible to identify a topology with a meaningful signal-to-noise ratio or sensitivity since these vary dramatically with the interferometer *configuration*.

During the design and construction of the first generation of detectors the Sagnac topology has been investigated and prototypes have been built [501] but eventually it did not show significant advantages over the Michelson topology [366]. More recently it has been proposed to use the Sagnac topology as a *speed meter* [158] to reduce the quantum noise. The Sagnac topology can be hosted in different ways in a triangular geometry: each Sagnac as an equilateral triangle, or as an L-shaped zero-area Sagnac. Noise couplings due to the Sagnac effect favor the zero-area Sagnac topology: it can be shown that for a typical choice of optical parameters this extra noise couplings do not impose stringent new requirements in the case of a zero-area Sagnac interferometer.

We note that Michelson-based detectors currently offer the advantage of using the experience as well as the advanced optical technologies of the first two detector generations.

5.3.3 The triangle

At any given moment an L-shaped detector can only detect one linear combination of polarisations of a gravitational wave. However, for estimation of source parameters from the measured signal, the full polarisation

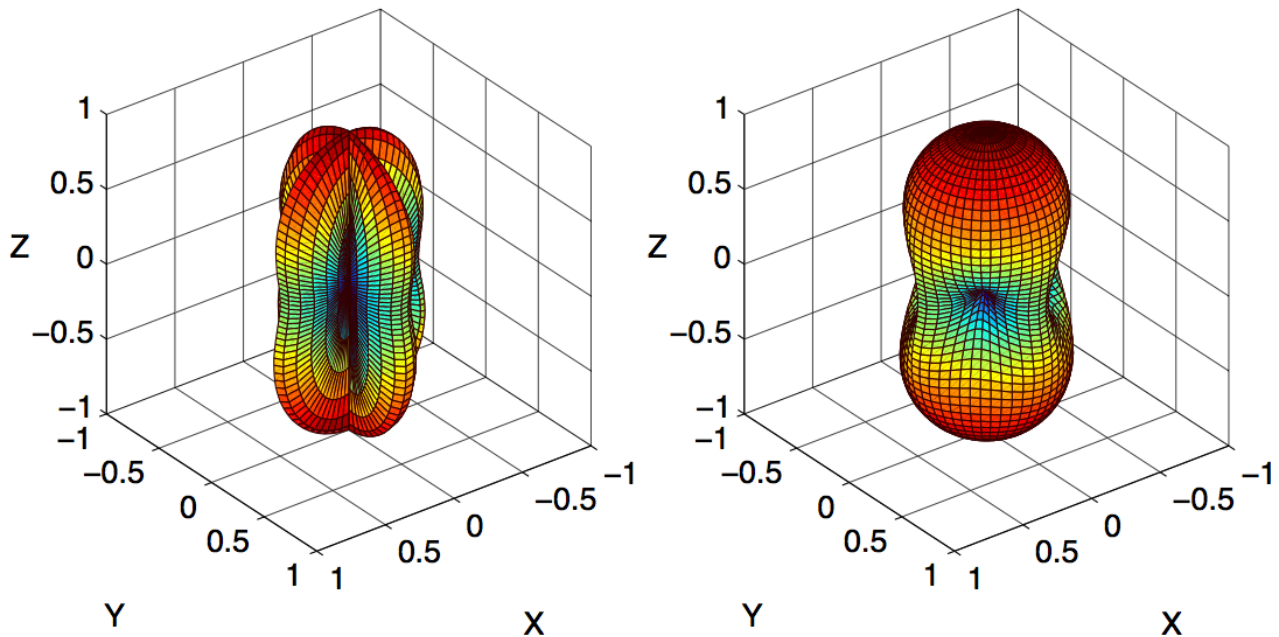


Figure 141: The response of a detector to a linear polarised gravitational wave as a function of the detector orientation. Both plots show the normalised sensitivity to a wave travelling along the z-axis. Each data point represents the sensitivity of the detector for a specific detector orientation defined by the detector normal passing the respective data point and the origin. The colour of the data point as well as its distance from the origin indicate the magnitude of the sensitivity. The left plot depicts the response of a single Michelson, while the right plot gives the response of a set of three interferometers in a triangular geometry.

information can be essential. Thus it is of considerable interest to design a detector able to detect both polarisations (and thus the full content) of a gravitational wave at all times. This can be achieved by combining two co-located L-shaped detectors which are positioned at 45° to each other. Already more than 20 years ago it was recognised that a triangular geometry would provide the same sensitivity to both polarisations as detectors at 45° while requiring less enclosed space and fewer end stations [567]. In particular, the sensitivity of the two geometries shown in Figure 142 differs only by 6% [220]. The difference in the sensitivity to different polarisations between a single L-shape and a triangular geometry can be best illustrated with a plot of the so-called antenna pattern as shown in Figure 141.

Using co-located detectors yields another advantage. Both layouts shown in Figure 142 represent detectors with redundancy. Redundancy here can be understood in relation to the continuous operation of the detector as an observatory, or as a feature of the data streams generated by the full system. Redundancy in operation is achieved by having multiple detectors which generate an equal or similar response to gravitational waves. This is desirable in observatories which are expected to produce a quasi-continuous stream of astrophysical meaningful data over an substantial amount of time. Typically laser interferometers cannot produce science data during upgrades and maintenance work. Thus only alternate upgrading and data taking of redundant detectors can avoid long down-times, for example during detector upgrades.

Such redundancy is obviously provided in the case of the 4 L-shaped detectors, where two detectors are always identical but can be operated independently. However, one can easily show that the triangular geometry provides exactly the same redundancy [220]. For example, for three equal L-shaped interferometers oriented at 0° , 120° and 240° , one obtains:

$$-h_{0^\circ} = h_{240^\circ} + h_{120^\circ}, \quad (156)$$

where the sign of the operation is defined by which ports of the interferometers are used to inject the laser light.

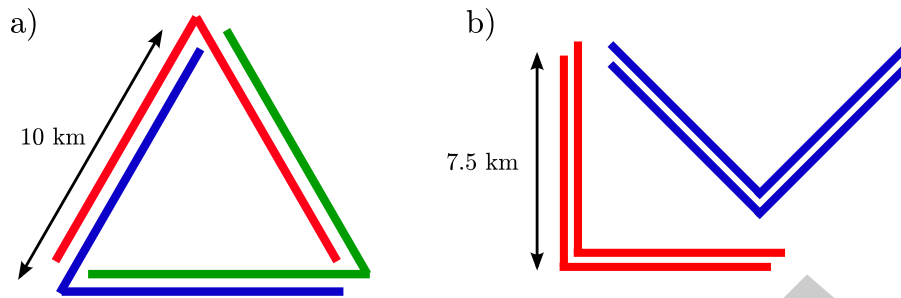


Figure 142: a) Triangle geometry: three L-shaped detectors with 10 km arm length are positioned in an equilateral triangle. b) Four L-shaped detectors at 0° and 45° . The integrated length of all interferometer arms in both configurations is 60 km and two interferometer arms can share the same structure. Note that for avoiding noise correlations between two detectors the neighbouring interferometer arms would probably be housed in a separate vacuum tubes.

Thus the two interferometers at 120° and 240° create exactly the same response as the one at 0° . This allows to construct so-called null-streams (or null-data streams) [248]. Null-streams are a powerful data analysis method that allows to identify noise which is uncorrelated between the detectors. Even though this does not increase the sensitivity of a detector, it can add significantly to the robustness of the data processing pipelines and thus lead, for example, to shorter delays between an event and the generation of a trigger for follow-up searches with optical telescopes. The triangular geometry represents the minimal setup in one plane that can resolve both polarisations and provides redundancy for the generation of null-streams.

5.4 Review on the topology of the detector

Author(s): *Helge Mueller-Ebhardt, Keiko Kokeyama*

The topology of a gravitational-wave detector is determined by the optical system formed by its core elements [220]. Examples of basic topologies are the Michelson interferometer, the Sagnac interferometer and the Mach-Zehnder interferometer. The specific optical layout of a detector includes more details about the actual realization, i.e. lenses, telescopes, folding mirrors, mode cleaners, control system, injection system, detection system. Those issues are addressed in Sec. ???. Finally, the configuration fixes the set of parameters that can be changed for a given topology, ranging from circulating optical power, bandwidths and detunings of cavities to the detection angle of a homodyne detection (cf. Sec. ???). In a laser-interferometric gravitational-wave detector, there are different types of noise sources, which are usually categorized into quantum noise sources (cf. Sec. 5.4.2) and classical noise sources (cf. Sec. 5.4.3). In terms of the noise, the main difference in the sensitivity of the different topologies comes from the spectral distribution of the quantum noise, as it is described in details in Sec. 5.5.1, even though there could also arise differences in the susceptibility to the classical noise, due to the fact that there are e.g. a different number of mirrors or different shapes of cavities.

5.4.1 Different topology options

In the following we will list the different main interferometer topologies that can be used for gravitational-wave detection and describe their basic optical systems. A full gravitational-wave detector could actually consist of more than one of those main interferometers and could also be equipped with additional techniques in order to achieve a specific susceptibility to the quantum noise as it will be described in Sec. 5.5.1. Note that in principle all of the mentioned interferometer topologies can be fitted into a L-shape or into another two-arm shape under an arbitrary angle, as shown in Fig. 143.

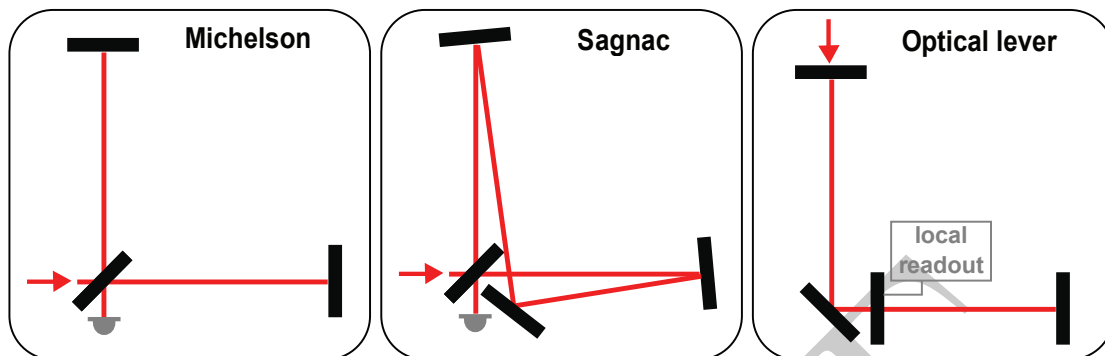


Figure 143: Different (basic) topology options: simple Michelson interferometer topology (left panel); zero-area Sagnac interferometer topology (middle panel); optical bar topology (right panel)

- **Michelson interferometer** (basic): a laser beam is split at a beam splitter and send along two perpendicular interferometer arms (cf. left panel of Fig. 143). The ends of these arms (north and east) are marked by highly reflective identical end mirrors, which reflect the beams back into themselves so that they can be recombined at the beam splitter. Generally, the Michelson interferometer has two outputs, namely the so far unused (south) port and the (west) input port. Both output ports can be used to obtain interferometer signals, however, most setups are designed in such a way that the signals are detected at the south port. For the detection of gravitational waves, the Michelson interferometer has to be sensitive to small perturbations in the difference of the two arm lengths and the phase relation is chosen in such a way that this signal interferes constructively at the south port. Usually the south port is kept nearly dark, with all light reflected back to the west input port, then also called the bright port of the interferometer. A power-recycling mirror can be positioned at the bright port in such a way that it forms a resonant cavity for the carrier light together with the mirrors of the two interferometer arms. Furthermore, each interferometer arm can be replaced by equal Fabry-Pérot cavities, formed by an input mirror and an end mirror. An additional mirror can also be placed at the interferometer's south port, known as the signal-recycling mirror. Another possibility is to send the output signal at the west port into an additional resonator, a so-called sloshing cavity. Furthermore, polarizing optics can be used in order to send the beam back into the interferometer. The Michelson interferometer is the standard topology for interferometric gravitational-wave detectors. The great advantage of this is, that there is a lot of experience gathered.
- **Sagnac interferometer** (basic): a laser beam is split into two beams at the beam splitter which travel both through the whole interferometer but in opposite directions. The two beams are recombined at the beam splitter. The interferometer has only one output port, namely the so far unused (south) port. A Sagnac interferometer is by construction always operated at a dark port, where all carrier light is reflected back to the input port. The arms can be folded in such a way that both beams circulate around a zero area (cf. middle panel of Fig. 143) in order to make the interferometer insensitive to rotations and forming two perpendicular interferometer arms. Those arms can be replaced by ring resonators, either of rectangular or triangular shape. For the Sagnac interferometer topology, an additional mirror at the input port can realizes power-recycling and an additional mirror at the output port can realize signal-recycling. Up to now a Sagnac interferometer has never been adopted as a large-scale interferometric gravitational-wave detector. Only some features have been tested in table-top experiments and a theoretical study has started to explore noise couplings in a Sagnac interferometer [154].
- **Optical bar:** The optical bar topology is an optical realization of a mechanical resonant bar gravitational-wave detector. It essentially consists of two coupled optical resonators, which are shape as an L and coupled through a light, partially transmissive mirror as shown in the right panel of Fig. 143. An additional local meter is applied to the central mirror, reading out its motion. The local meter could in principle be any device but its sensitivity is essentially determining the sensitivity of the optical bar detector. It is even

not obligatory for the local meter to be an optical device, moreover it could be a SQUID-based microwave meter as a speed meter, or some other high precision superconductive sensor. The optical bar topology can be transformed into an optical lever topology by inserting an additional mirror into each arm of the L, forming a resonant cavity together with the corresponding end mirror.

5.4.2 Requirements on the topology due to quantum noise

The so-called free-mass standard quantum limit (SQL) [108, 110] on high-precision measurements is imposed by the Heisenberg uncertainty principle, when it is applied to free-falling test masses. The spectral representation of this quantity, which falls off with one over frequency in amplitude and only depends on the test-mass' weight and arm length of the detector, has become a standard reference for the quantum noise of interferometric gravitational-wave detectors. With the help of this reference one is able to compare the quantum noise of different topologies and configurations having the same test-mass weight and arm length. The quantum noise of a gravitational-wave detector consists of two parts: the quantum measurement noise, i.e. the direct imprecision of the measurement, and the quantum back-action noise. For interferometric gravitational-wave detectors, the direct measurement process consists of counting the number of photons by recording the photo current of the photo diode. The photons of a coherent beam arrive according to a Poissonian distribution. The photon counting error represents the direct measurement noise, which is usually called photon shot noise. The power of this noise source is inversely proportional to the circulating laser power. The measurement's back action is clearly given by the laser light's fluctuating radiation pressure which imposes a force onto the mirror and causes the radiation-pressure noise in the measurement output. The power of this noise source is in contrast to the photon shot noise directly proportional to the circulating laser power. Since the suspended mirrors in a gravitational-wave detector can be approximated as free falling test masses in the direction of the incident laser beam – due to a very low eigenfrequency of the pendulum created by the mirror's suspension – and the two quantum noise sources are uncorrelated they result in the free mass standard quantum limit. In this case, the radiation-pressure noise dominates the spectral density of the quantum noise at lower frequencies while the shot noise dominates at higher frequencies. Therefore, one in general needs to trade-off between high optical power for a low shot noise and not too high optical power in order to cope with the radiation-pressure noise. One way out of this problem is the xylophone configuration [267], where the detection band of the gravitational-wave detector is split into two or more frequency bands, for which different configurations (or even topologies) are responsible for.

On the other hand, the SQL is actually not a real limitation on the quantum noise strength of a gravitational-wave detector. Several methods for overcoming the SQL, which are suitable for laser interferometric gravitational-wave detectors, have been proposed. They have different, and often very special, requirements on the optical topology. The quantum-noise reduction techniques can be divided into two main groups, where the classification is not chosen in terms of the topology, but by the technique of how the quantum noise is reduced: the first one is based on the principle, that the goal of the gravitational-wave detectors is not the measurement of the test-mass position, which is a quantum variable and thus cannot be measured continuously with a precision better than the SQL, but rather the detection of a gravitational-wave strain as a signal, which can be treated as a classical (tidal) force acting on the test mass mirrors [115]. It was shown that by introducing cross-correlation between the quantum measurement noise and the quantum back-action noise, arbitrary high sensitivity (in terms of the quantum noise) can be achieved [306] – assuming the absence of optical losses. The correlations are actually used here to quantum-mechanically cancel the back-action noise in the measurement output. Thus, this method relies clearly on **noise-cancellation techniques**. The second group of methods is based on the idea that the spectral distribution of the SQL itself is not a fixed constant, but depends on the test object dynamics, i.e. on the (mechanical) susceptibility of the test mass, which relates the test-mass motion to all forces acting on it. Therefore, the free-mass SQL can be beaten by using a more responsive object and increasing thus its signal displacement – the harmonic oscillator as an example has much stronger response to near-resonance forces and therefore a better sensitivity than the free-mass SQL around the resonance frequency. Therefore, the sensitivity gain is obtained not by delicate cancellation of the quantum noise, but by a classical **signal amplification**. More details about quantum-noise-reduction techniques are given in Sec. 5.5. In that section we will also see that with those topologies there are different detector options for the main interferometer: the position meter,

the optical spring interferometer, the speed meter, the optical transducer. Furthermore, all those main interferometer detectors can then be additionally equipped with the input-squeezing technique (for details cf. Sec. ???) and the variational readout technique (cf. Sec. 5.5.1).

5.4.3 Requirements on the topology due to technical noise sources

Apart from the quantum noise there are many other noise sources, usually called classical or technical noise sources, degenerating the sensitivity of a laser interferometric gravitational-wave detector. In the third generation of detectors these classical noise sources have to be dealt with different techniques which might have additional demands on the topology as we shall review in the following.

Suspension thermal noise. The suspension thermal noise will be a serious noise source in third generation gravitational-wave detectors. For more details refer to Sec. ???. Here we will only describe its influence on the topology: in order to avoid high thermal noise, the fibers of the suspended optics – especially those in a cryogenic environment – have to be as cool as possible. If the detector consists of more than one interferometer, then the question arises how the collinear interferometer arms are arranged in the tunnel. One of the interferometer arms could be placed above the other. Then it might be unavoidable that the laser beam of the interferometer lying upon the other intersects at some point with the suspension fibers of the other interferometer. In that case it is necessary that this laser field is not too strong in order not to heat up the suspension fibers and increase the thermal noise.

Mirror internal thermal noise. *Author(s): Keiko Kokeyama, Andreas Freise* The noise coming from thermal effects influencing the test-mass mirrors is dominating the noise spectrum in the mid frequency regime. There exist several different contributions to the total thermal noise of which the (coating) Brownian thermal noise is the largest in current interferometer topologies utilizing arm cavities. The obvious way of lowering thermal effects is cooling the mirrors down to cryogenic temperatures. Such cryogenic test-masses allow only for limited amount of optical power passed through the mirror substrates and coatings which influences the design of the detector. Another way to lower the thermal noise is to change the mode shape of the laser beam inside the interferometer (cf. Sec. 5.15). The higher-order Laguerre-Gauss (3,3)-mode (LG₃₃) which is proposed for thermal noise reduction in advanced gravitational-wave detectors [372, 546] requires that no triangular cavities are used because of the astigmatism issue. The optical parameters of a LG_{l,m} mode at the $2|l| + p$ order are degenerate with the other modes at the same order. As they have the identical optical parameters, they can degenerate in the resonant cavity, and they are decomposed by the astigmatism effect, i.e., when a beam experiences a non-zero angle of incident in respect to the mirror normal. Because the mode decomposition significantly degrades the mode purity inside the cavity, a two-mirror linear-cavity where the angle of incident is always zero is preferable as an optical resonator for the LG₃₃ mode.

- Parametric instability as discussed in Sec. ??? requires what in terms of the topology? *Author(s): Kazuhiro Yamamoto*

Any kind of displacement noise. *Author(s): Sergey Tarabrin* Most of the dominant noise sources in laser interferometric gravitational-wave detection can be related to the class of displacement noise: seismic noise, gravity-gradient noise, various thermal noise sources, even the quantum back-action noise. Each method of suppression or elimination of displacement noise is usually suited for control of only one kind of noise: seismic isolation, measurement and partial cancellation of gravity gradients, cryogenics, quantum-noise-reduction schemes. Displacement-noise-free interferometry (DFI) is the method of displacement noise cancellation which aims at simultaneous elimination of the information about all position fluctuations of the test masses, but leaving a certain amount of information about gravitational waves. All known DFI schemes can be divided into two categories: schemes with complete and partial displacement noise cancellation. Complete displacement noise cancellation relies on the distributed nature of gravitational waves. While displacement noise imprints on the optical phase only at the moments of the laser beam reflection at the test masses (localized effect), gravitational waves affect the laser beam along its optical path (distributed effect). From the viewpoint of some local observer the interaction of the gravitational wave with the interferometer adds up to two effects [428]: the motion of the test masses in the gravitational-wave tidal force-field (which is indistinguishable from the action of fluctuating

forces, therefore it is a localized effect) and the direct coupling between the gravitational wave and light (distributed red-shift effect). DFI implies the cancellation of displacement noises along with the localized part of the gravitational-wave effect, leaving the distributed red-shift effect in the interferometer response. Since the latter one has the order of $O[h(L/\lambda_{\text{GW}})^2]$ (where h is the gravitational-wave amplitude, L is the interferometer linear scale and λ_{GW} is the gravitational wavelength), DFI has much weaker gravitational-wave susceptibility than conventional gravitational-wave detectors in the long-wavelength regime $L \ll \lambda_{\text{GW}}$. Complete displacement noise cancellation can be achieved in an interferometer with large enough number of the test masses by properly combining several response signals [159]. For instance, 2- and 3-dimensional setups composed of two Mach-Zehnder interferometer topologies sharing the beam-splitters [162]. The gravitational-wave response of the 2-dimensional scheme has the order of $O[h(L/\lambda_{\text{GW}})^3]$, while the one of the 3-dimensional scheme is of the order of $O[h(L/\lambda_{\text{GW}})^2]$. For comparison, the gravitational-wave response of the conventional Michelson interferometer is $O[h(L/\lambda_{\text{GW}})^0]$. Implementation of the time-delay devices, while improving the strength of the gravitational-wave response, limits the sensitivity by adding the noise [497]. Another class of DFI schemes with partial displacement noise cancellation aims on keeping strong enough gravitational-wave susceptibility, with either $O[h(L/\lambda_{\text{GW}})^0]$ or $O[h(L/\lambda_{\text{GW}})^1]$ leading orders in the response. This can be achieved with linear Fabry-Perot cavities, ring cavities, etc. A single Fabry-Perot cavity, double-pumped through both mirrors, allows elimination of their displacement noise in the proper linear combination of the responses, however, the sensitivity remains limited due to laser noise and displacement noise of all the auxiliary optics [507]. Modification of this scheme with two cavities placed symmetrically allows complete displacement noise cancellation but does not allow laser noise cancellation [429]. In a symmetric double Michelson interferometer with the arm-cavities the sensitivity is limited by the noise of the local oscillators used for detection of the transmitted waves in the arms; in addition, this scheme requires placing several mirrors on a single common platform rigidly that is very impractical [508]. Double pumping of the resonant ring cavity allows cancellation of its mirrors noise and laser noise, but cannot deal with displacement noise of the mirrors and beam-splitters used to produce the pumping waves [556]. To summarize, all detectors with either complete or partial displacement noise cancellation consist of combinations of many different topologies and therefore differ in general significantly from the conventional detectors especially in terms of the complexity and either have very weak gravitational-wave susceptibility or impractical requirements (like rigid platforms) to operate or suffer from uncanceled noises, thus making them hardly advantageous over the conventional non-DFI topologies.

Holographic noise. *Author(s): Sergey Tarabrin* It is currently widely assumed that the holographic principle, developed by G. 't Hooft and L. Susskind, should be the fundamental constituent part of any unified theory of quantum gravity. It says that that the physical theory defined in the space-time of dimensionality D is equivalent to another theory defined on the boundary of dimensionality $D - 1$. The most known mathematical realization of holographic principle is the AdS/CFT correspondence by J. Maldacena: string theory in anti-de Sitter space-time is equivalent to conformal field theory on its boundary. It follows from the holographic principle that if the volumetric system can be described by the theory on the boundary, then the maximal number of volumetric degrees of freedom should not exceed the number of their "images" on the boundary. Since the "classical" theoretical informational content of the region of space is defined by its volume, such a description contains much more degrees of freedom than allowed by the holographic entropy bound. Therefore, our 3-dimensional world must be "blurry" in order to match the number of degrees of freedom inscribed on some 2-dimensional holographic surfaces. The holographic uncertainty is a particular (highly speculative) hypothesis proposed by C. Hogan about how the holographic principle works in a flat space-time [274]. He posited that in order to preserve the holographic nature of space time, it must have diffractive nature described by the wave functions of transversal position distribution of matter-energy [275], i.e. transversal coordinates of two particles (test masses) separated by a distance L in a longitudinal direction should no longer commute: $[\hat{x}_1, \hat{x}_2] = i l_P L$, where the commutator is defined on the light-like geodesics only. The corresponding uncertainty relation reads $\Delta x_1 \Delta x_2 \geq l_P L$ meaning that the relative transversal positions of two test masses cannot be measured with infinite precision. The holographic uncertainty relation implies that the measurement of the transversal position of a single test mass with the optical signals will yield uncertain results with $\Delta x \geq \sqrt{l_P L}$, where L stands for the distance the light wave travels between the two measurements. This holographic fuzziness with associated uncertainty Δx should be seen in precise interferometry, otherwise it would be possible to distinguish more test-mass configurations than is allowed by the holographic entropy bound. Thus, in a Michelson interferometer measurement of the beam-splitter transversal position relative to the direction of the incident laser beam should

yield uncertain results. Uncertain measurement results produce the fluctuating time series, i.e. the noise, called holographic noise. The minimal level of expected holographic noise corresponds to the Gaussian space-time wave functions which minimizes the holographic uncertainty relation, much like in usual quantum mechanics. In the frequency region $f \ll c/L$ holographic noise power spectral density is frequency-independent and equals to $S(f) = 2t_P L^2/\pi$, or effective metric strain $h(f) = \sqrt{S(f)/L^2} = \sqrt{2t_P/\pi} = 1.84 \times 10^{-22}/\sqrt{\text{Hz}}$ with t_P standing for Planck time. Holographic noise prediction is thus fixed with no free parameters, therefore the hypothesis can be either confirmed or ruled out experimentally. Holographic noise signatures are currently being looked for in the noise spectrum of GEO-600 interferometer. However, the available sensitivity does not allow to make unambiguous conclusions. Since the space-time wave function universally defines the transversal distribution of mass-energy, holographic noise should exhibit particular cross-correlation features. Namely, the two closely positioned interferometers should produce correlated measurements of the holographic displacement, because they occupy nearly the same space-time volume and thus holographic motion of their test masses (beam-splitter, in particular) is defined by nearly the same wave function. If the two interferometers are aligned along their arms and are displaced by $\Delta L \ll L$ along one of them, then the cross-correlation spectral density equals to $S(f) = 2t_P L^2[1 - (\Delta L/L)]/\pi$. This expected feature of the holographic noise is to be tested in the Fermilab holometer which is currently under construction [276]. For the Michelson interferometer with the arm-cavities in the arms effective metric strain equals to $h(f) = N^{-1}\sqrt{S(f)/L^2} = N^{-1}\sqrt{2t_P/\pi} = N^{-1}1.84 \times 10^{-22}/\sqrt{\text{Hz}}$, where N is the average number of photon round trips inside the cavities. The reason for the N^{-1} factor is that the cavities effectively lengthen the arms for the gravitational waves (this holds true for the frequencies $f \lesssim c/2LN$), thus amplifying the response to the gravitational waves, but do not change the beam-splitter holographic displacement spectrum [274]. With planned transmittances of the arm-cavities input mirror and the end mirror of 7000 and 10 ppm, respectively, the number of photon round-trips inside the ET cavities equals to $N \approx 277$, thus lowering the holographic metric strain to $h(f) \approx 0.66 \times 10^{-24}/\sqrt{\text{Hz}}$. The development of sound theoretical models and experimental test are under way. If it turns out that the holographic noise is a serious issue for the Einstein telescope gravitational-wave detector, the optical design (as e.g. cavity finesse) has to be adopted.

5.4.4 Alternatives to laser interferometry: atomic sensor

Author(s): Sergey Tarabrin

It is in principle also possible to utilize light pulse atom interferometry to detect gravitational waves. Light pulse atom interferometry can be thought of as a comparison of time kept by internal atom clocks and optical wave of the laser. The incoming gravitational wave changes the rate of time which can be seen in an interferometer phase shift. The major advantage of the atom-light interferometry over conventional optical interferometry is that the atoms, playing the role of inertial sensors, are not subjected to the external fluctuations in comparison with the mirrors, and thus do not require sophisticated vibration isolation techniques. A phase shift measurement in atomic interferometer consists of three steps [192]: first, the atomic cloud is prepared, cooled to sub-microkelvin temperatures and then launched. Atoms in the cloud are in the $|\text{ground}\rangle$ state and are freely falling after the launch. In the second phase light pulses are applied. The “beamsplitter” $\pi/2$ -pulse places atoms in the superposition of two states: $1/\sqrt{2}|\text{ground}\rangle + 1/\sqrt{2}|\text{excited}\rangle$. Since the internal state of the atom is correlated with its momentum, atoms in ground and excited states acquire different velocities, and thus both states become temporarily and spatially separated. After some time the “mirror” π -pulse exchanges the two components of the superposition: $|\text{ground}\rangle \rightarrow |\text{excited}\rangle$, $|\text{excited}\rangle \rightarrow |\text{ground}\rangle$, so that the atoms will finally overlap. Finally, the second “beam-splitter” $\pi/2$ -pulse makes the two branches of the atom wave function interfere, in full similarity to a Mach-Zehnder interferometer. The third phase of interferometry is detection. The interference pattern can be extracted by measuring the population of atoms in a given state, for instance, in the excited state. The measured phase shift results from both the free-fall evolution of the quantum state along each path in interferometer and from the local phase of the laser which is imprinted on the atoms at the moments laser pulses are applied. Since laser sources and atomic interferometer can be separated by a significant spatial distance, the incoming gravitational wave modulates the latter, thus causing the modulation of the arrival time of the laser pulses which enters the measured atomic phase shift. A terrestrial based gravitational-wave detection with light-atom interferometry can be realized in a vertical shaft with the linear scale of ~ 1 km. Two atomic interferometers

of the linear scale of 10 m are placed on the top and the bottom of the shaft and are operated by the common lasers. With the reasonable measurement repetition time ground-based setup will have the peak susceptibility to the gravitational waves around 1 Hz that is very interesting from the astrophysical point of view. Such a setup allows performing the differential measurement between two atomic interferometers which significantly suppresses vibrational and optical noise of the lasers. The vibration of the optical trap which leads to different launch velocities is of less importance, since the initial “beam-splitter” pulse is applied after the atoms are launched. However, spread in velocities will enter the measurement error through the gravity-gradients, since in the nonuniform gravitational field atoms moving along different trajectories experience different gravitational forces. Gravity-gradients seem to be one of the major limiting factors towards the increase of the sensitivity. Other noise sources come from the variations of the magnetic field which change the atoms energy levels, coupling of the Earth rotation to the fluctuating transversal velocity of the optical trap. One of the dominating noise sources with the technique currently available is the atomic shot noise. It can be lowered by implementation of the sources with more intense atom fluxes and/or preparation of the atoms in squeezed states. Although light pulse atom interferometry has already found applications in atomic clocks, metrology, gyroscopes, gradiometers and gravimeters, its implementation in gravitational-wave detection requires detailed and comprehensive study and further development of the noise-lowering techniques. With the current technologies available atomic interferometers cannot provide the same level of sensitivity as the well-developed optical interferometers.

5.5 Quantum noise reduction techniques

Author(s): Helge Mueller-Ebhardt, Keiko Kokeyama

Already the second generation of laser-interferometric gravitational-wave detectors (such as the Advanced LIGO detector [22] and the the Advanced VIRGO detector [163]) is expected to be limited by the quantum noise — the shot and the back-action noise — nearly within the full detection band. Within the context of the third generation of detectors this aspect becomes even more important, since there is an enormous effort in increasing the quality of the technical components of the interferometer — such as the mirror and beam splitter materials as described in Sec. ???; the suspension systems (see Sec. ???); the stability of the laser source (Sec. ???) — in order to decrease the strength of all the technical noise sources by a large amount. Beside parameters such as the circulating optical power and the test-mass weight, the spectral distribution of the quantum noise mainly depends on the topology of the detector including the injection strategy at the bright port as well as the detection strategy at the dark port of the interferometer. Therefore, the choice of the topology and configuration of the detector are severe for the design of future gravitational-wave detectors. Especially because parameters as the optical power and the test-mass weight will always be limited due to technical reasons, the design of future gravitational-wave detectors is calling for quantum-noise-reduction techniques. As we have seen in Sec. 5.4, there are different topology options available which can all be fitted into an L-shaped geometry. With the different topologies one can build up different types of detectors, having specific quantum noise features, as we have reviewed within this design study. Many of them have actually great potential in reducing the quantum noise, but there is a big discrepancy in terms of readiness: some are far away from being ready to be implemented into gravitational-wave detectors, others have been already demonstrated experimentally as a proof of principle or have been even already implemented into gravitational-wave detectors. In the following we will report on the sensitivity of

- optical-spring interferometer
- speed-meter interferometer
- optical-inertia interferometer
- optical transducer with local readout
- (frequency-dependent) input-squeezing interferometer
- variational-output interferometer

even though not all of them can be fitted into the same optical layout. It has turned out that one of these techniques is probably not able to reduce the quantum noise in the required broadband way, but certain combinations among these techniques are possible. Additionally, one is not restricted to build a detector from only a single interferometer, but from two or more interferometers covering different frequency bands as a xylophone interferometer [267]. Within the design study, there have been carried out many optimizations of the quantum noise of different detectors towards different astrophysical sources. In the following there are example noise curves given which are optimized towards the detection of neutron star binary inspirals, as carried out in Ref. [377]. Furthermore, those examples are attempts to realize the ambitious sensitivity goal of the Einstein telescope gravitational-wave detector – in terms of the quantum noise – with a single interferometer, where the total circulating optical power is limited to 3 MW, the arm length to 10 km and the test-mass weight to a few hundred kilograms.

5.5.1 Quantum noise features of different topologies

The first candidate among the different types of detectors is the **simple position meter**: here we gather the Michelson interferometer topology w/o or w/ arm cavities, w/o or w/ power-recycling, w/o or w/ tuned signal-recycling (cf. Sec 5.4.1). The installation of a power-recycling cavity (by putting an additional mirror at

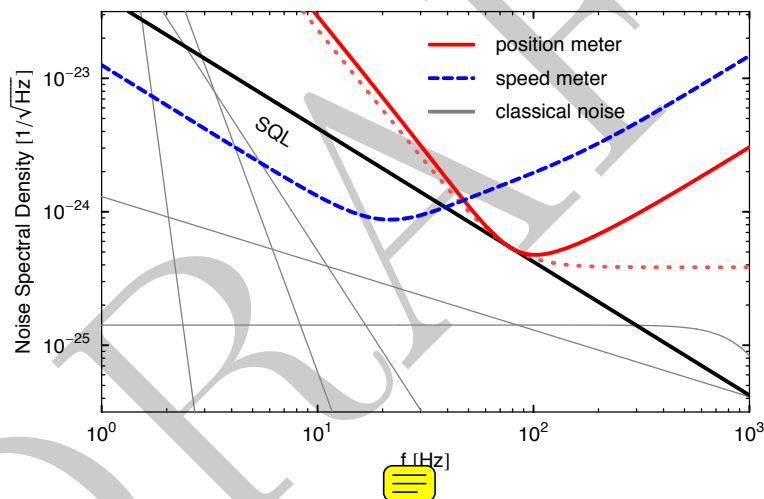


Figure 144: Example quantum noise spectral densities for position meter (solid curve), with adiabatically eliminated cavity mode (dotted curve) and for a speed meter (dashed curve): 10 km arms; 3 MW optical power; 120 kg test-masses. Example noise budget (gray curves): seismic and gravity gradient noise reduced by a huge amount compared to advanced detectors; suspension thermal noise (coating thermal noise) reduced by a factor of 10 (4.5) in amplitude compared to estimations for Advanced LIGO detector.

the bright port of the interferometer) and the use of cavities in the arms of the interferometer, both increase the circulating optical power inside the interferometer, therefore force up the interaction strength between the laser field and the test-masses and reduce the shot noise (dominating at high frequencies) but at the same time increase the radiation-pressure noise (dominating at low frequencies). From another point of view (namely when the required circulating optical power in the arms is fixed) the power-recycling technique can help to lower the required input power, while using arm cavities can additionally lower the optical power which has to pass the beam splitter, preventing thermal effects in the transmissive optics to become a major problem and also minimizing the bright port / dark port coupling due to the beam splitter motion [256]. The use of arm cavities additionally increases the signal-susceptibility within the finite bandwidth of the optical arm resonators, but decreases it above the optical bandwidth making the shot noise spectral density raise towards higher frequencies and therefore decreasing the bandwidth of the gravitational-wave detector. Signal-recycling, as proposed by Meers [359], can increase the bandwidth of the gravitational-wave detector by creating an effective bandwidth. Here an additional mirror, the so-called signal-recycling mirror, is placed at the dark output port of the interferometer, reflecting parts of the signal modulation fields back into the interferometer

and forming a signal-recycling cavity either together with the end mirrors of a simple Michelson interferometer or with the input mirrors of the interferometer's arm cavities. The signal becomes recycled which basically means that it is amplified due to an increase in interaction time between the laser field and the mirrors. If the signal-recycling cavity is tuned with respect to the laser frequency, the optical resonator (or the two coupled optical resonators in a Michelson interferometer with arm-cavities) have an (effective) bandwidth — which can be greater than the original bandwidth of the arm-cavities. In such a detector the quantum noise depends mostly on the optical power circulating in the interferometer, the bandwidth and length of the cavities and the test-mass weight, which altogether define the measurement frequency, i.e. the frequency where the quantum noise touches the standard quantum limit. The strength of the quantum noise is basically shuffled between high and low frequencies by shifting the measurement frequency towards higher frequencies. All first generation laser-interferometric gravitational-wave detectors (LIGO [9], VIRGO [212] and TAMA [39]) so far have been constructed as simple position meters. In Fig. 144 we see example quantum noise curves for a simple position meter and the standard quantum limit for such a detector with 10 km long arms and 120 kg test-masses. The quantum noise spectral densities are plotted for 3 MW circulating optical power in the arms for a detector with an effective 50 Hz cavity-bandwidth (solid curve) and for a detector with adiabatically eliminated cavity mode (dotted curve). Furthermore, the different contributions of an example classical noise budget for a third generation detector with classical noise reduction techniques as described within this design study (cf. Sec. ???) is additionally adumbrated in Fig. 144 and shows a big gap between this assumed classical noise budget and the standard quantum limit. It is obvious that such a simple position meter would be totally dominated by the quantum noise, i.e. a waste of efforts in the classical noise reduction, and therefore not suitable to reach the sensitivity goal of the Einstein Telescope gravitational-wave detector. For more details refer to e.g. Ref. [377] and references therein.

When the signal-recycling cavity is neither resonant nor anti-resonant with respect to the carrier frequency, the technique is called detuned signal-recycling. In this case the sensitivity of the interferometer is enhanced around the (effective) optical resonance frequency. The signal-recycling technique was already successfully tested in a 30 m prototype gravitational-wave detector [219, 261], in table-top experiments [365, 496] and has been implemented into the GEO600 detector [246]. Additionally, the optomechanical coupling in the arm cavities of a Michelson interferometer with detuned signal-recycling can induce a restoring force onto the differential motion of the arm-cavities mirrors — the optical spring effect [124], which can up-shift the mechanical resonance frequency into the detection band. We will call such a device an **optical spring interferometer** [124–126, 442]. Here the sensitivity of the detector is further enhanced around the second resonance, the optical spring resonance. This quantum-noise reduction technique belongs to the second group of methods as defined in Sec. 5.4.2. The optical spring effect has been demonstrated e.g. in a 40 m prototype gravitational-wave detector [365] and in several table-top experiments [170]. Furthermore, the Advanced LIGO detector [22] will very likely make use of the optical spring effect in order to improve the sensitivity. In Fig. 145 example noise curves for such an optical spring interferometer are given. For the optical spring interferometer the optimal quantum noise – optimal for the specific wave-form of neutron star binary inspirals – becomes very narrow peaked around 100 Hz [377]. Also for different astrophysical sources the optimal quantum noise spectral density is rather narrowband than broadband. Note that the concept of the optical spring interferometer can be extended to double optical spring interferometer [442] or even multiples optical spring interferometer, where a second (or multiple) additional frequency-shifted carrier is injected into the interferometer, creating additional optical springs which can be used to enhance the sensitivity and additionally stabilize the optomechanical system within the detection band.

A third detector option is to use an optical **speed meter** [299]. The idea of using speed meter detectors was to totally avoid the quantum back-action of the measurement. At first glance it seems to be very promising to reach this goal by measuring the speed of the test-masses, because it is usually proportional to the momentum, which, as a conserved quantity, cannot introduce any back-action noise. But once the detector couples to the speed, it has been shown that in this case the conjugate momentum is actually not only proportional to speed [296] of the test object. Nevertheless, a speed meter is able to surpass the standard quantum limit broadbandly by removing the (frequency-independent) radiation-pressure noise from the measurement output. The dashed curve in Fig. 144 shows a typical example for a quantum noise curve of a speed meter interferometer – here with 10 km long arms, 120 kg test-masses, 3 MW circulating optical power in a 35 Hz-bandwidth cavity. There exist different proposed designs of how to realize a speed meter with different topologies: it is possible to turn a

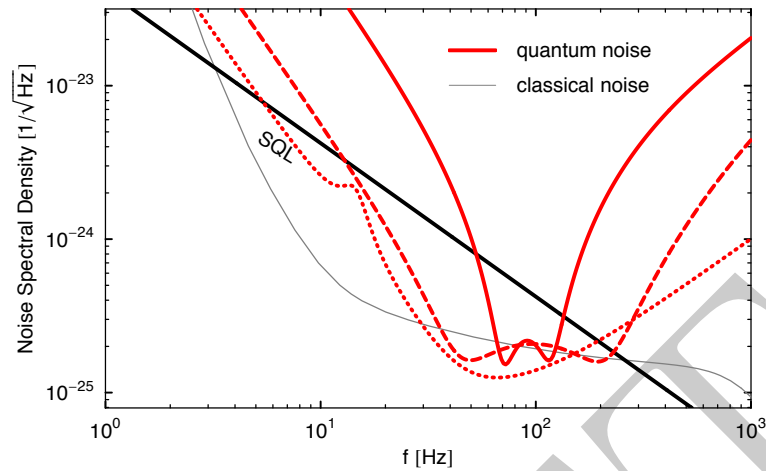


Figure 145: Example quantum noise spectral densities for Michelson interferometer with arm cavities (10 km; 3 MW optical power; 120 kg test-mass mirrors) and detuned signal-recycling (136 Hz effective detuning; 16 Hz effective bandwidth; $2\pi/3$ detection angle) – no input-squeezing (solid curve), no optical loss. Dashed curve: with 10 dB frequency-dependent input-squeezing (208 Hz effective detuning; 120 Hz effective bandwidth; 0.44π detection angle) and 75 ppm loss in each 10 km filter cavity. Dotted curve: variational output with 10 dB frequency-independent input-squeezing (4 Hz effective detuning, 180 Hz effective bandwidth) and 75 ppm loss in each 10 km filter cavity.

Michelson interferometer topology into a speed meter by adding a sloshing cavity [426, 427] to the interferometer at the dark output port, where the signal sloshes back and forth, realizing a time-delayed sensing of the test-mass position. Another option is to use polarizing optics and build up a speed meter from a Michelson interferometer topology by either re-sending the signal into the interferometer multiple times [353] or by circulating the light through the two arms [183] of the Michelson-like setup. The most obvious way to realize an optical speed meter, however, is by using a Sagnac topology (cf. Sec 5.4.1) with triangular or rectangular ring cavities in the (folded) arms [158, 201, 375]. Ignoring the influence of optical losses, all those different speed meter realizations have the same quantum noise performance [158] even though they have different technical advantages and disadvantages. The specific quantum-noise feature of a speed meter is that it has a flat response to the radiation-pressure noise at low frequencies [158], providing a constant back-action free detection quadrature. The measurement can therefore be made shot-noise limited at lower frequencies but with a decreasing signal transfer [501] (cf. Fig. 144). A detuned signal-recycling cavity turns a speed meter interferometer into an **optical inertia interferometer** [375]: the optomechanical coupling influences the dynamics of the test-masses – it modifies their dynamical mass by introducing an optical inertia. In Fig. 146 we see the quantum noise of a signal-recycled Sagnac interferometer, which provides high sensitivity mainly in the low-frequency regime, due to the speed meter effect, while the detuned signal-recycling broadens the sensitivity curve by opening it a little more to the high-frequency regime [377]. Note that the optical inertia can become in principle even negative and then can cancel the mechanical inertia. The hope is that in this way one can create a test object which has a high resonance-type mechanical susceptibility in a broad frequency band. Such a situation can also be found in the double optical spring interferometer, by exploiting the frequency dependence of the two optical springs [295].

Finally, the last option for the main interferometer, which we want to review here, the **optical transducer** [109, 113, 297, 441], is totally different compared to the others in terms of the readout method: the idea of such schemes is not to measure the phase shift of the laser field via monitoring the outgoing modulations fields at the dark port of an interferometer but to measure the redistribution of optical energy directly inside an interferometer by converting the gravitational-wave strain via radiation pressure into real mirror motion. This motion should then be sensed by an additional highly sensitive local meter. The overall sensitivity to gravitational waves for such a transducer scheme depends not only on the transducer ability of the main interferometer but also on the sensitivity of the local meter. Several optical realizations have been proposed: the initial idea was to construct an

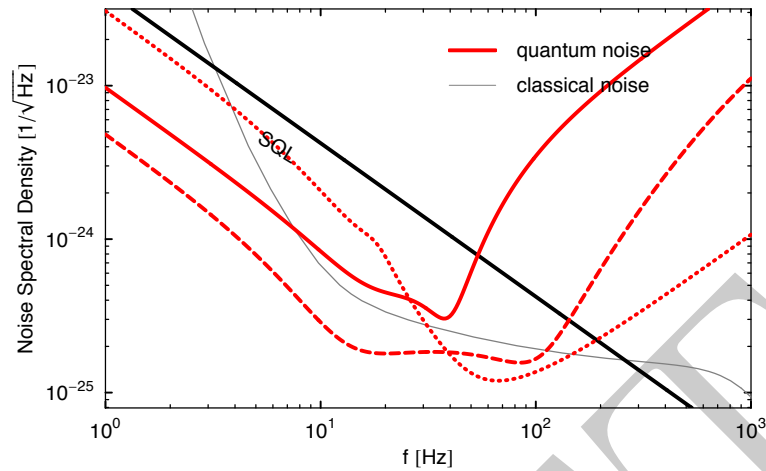


Figure 146: Example quantum noise spectral densities for Sagnac interferometer with ring cavities (10 km; 3 MW optical power; 100 Hz bandwidth; 120 kg test-mass mirrors) and detuned signal-recycling (42 Hz effective detuning; 0.475π detection angle) – no input-squeezing (solid curve), no optical loss. Dashed curve: with 10 dB frequency-dependent squeezed input (150 Hz bandwidth; 95 Hz effective detuning; 0.475π detection angle) and 75 ppm loss in each 10 km filter cavity. Dotted curve: variational output with 10 dB frequency-independent squeezed input (50 Hz bandwidth; 0.5 Hz effective detuning) and 75 ppm loss in each 10 km filter cavity.

optical bar, as an optical analog to an mechanical bar resonator. Later this topology was extended to the optical lever scheme [297], where the interaction strength is enhance by the use of arm cavities. Furthermore, it had been realized before that also a detuned signal-recycled Michelson interferometer with arm cavities effectively functions as an optical bar at low frequencies, where the gravitational-wave strain is converted into mirror motion of the input mirrors of the arm cavities. In this case even the realization of a local meter is straightforward: a second frequency-shifted carrier can be inserted into the interferometer, which is anti-resonant in the arm cavities, and therefore forming a small interferometer with the arm-cavity input mirrors as its end mirrors. This local readout scheme [441] is a combination of an optical bar interferometer and a optical spring interferometer, where the two outputs can be combined in an ideal way to enhance the sensitivity at lower frequencies (optical bar) and simultaneously at higher frequencies (detuned signal-recycled Michelson).

All these different main interferometer detectors can be equipped with a technique which is usually called **input-squeezing**. The use of squeezed states of light for improving the sensitivity of gravitational-wave detectors was first proposed in 1981 by Caves [149]. He showed that the quantum noise limited sensitivity in a shot noise dominated interferometer can be enhanced by the injection of broadband (frequency-independent) squeezed fields into the interferometers signal port. Accordingly at a point, where the interferometer performance will be limited by the amount of the achievable circulating light power and the thermal load in its optics, squeezed field injection can be used to either relax the high power requirement or increase the sensitivity further. The reduction of shot noise by the aid of squeezing was later experimentally shown in Refs. [241, 354, 572] (cf. Sec. ???). However, at first view the enhancement of an interferometers sensitivity with frequency independent squeezing (squeezed light with a fixed quadrature angle) can only be achieved in a certain frequency range. This is a direct consequence of the Heisenberg uncertainty principle. Considering a simple position meter, the quantum noise in its phase quadrature (shot noise) can be reduced by the amount of squeezing. Unfortunately, the quantum noise in the amplitude quadrature (radiation pressure noise) will be increased by the same amount enhancing the noise at low frequencies. Later it was revealed by Unruh [530] and others [284, 402, 576] that squeezed field injection with frequency dependent squeezing angle allows an overall quantum noise reduction including the radiation pressure noise. Motivated by the work of Unruh and Jackel & Reynaud the use of additional input and output optics — namely filter cavities — was proposed by Kimble *et al.* [306]. Applying these filters (commonly referred to as Kimble-filters) converts a conventional interferometer into a broadband quantum non-demolition interferometer (cf. Sec. ???). The filters allows the preparation of squeezed states providing a frequency-dependent squeezed

quadrature which is adapted to the interferometers quadrature rotation. The injection of such a prepared squeezed state leads to a quantum noise reduction over the entire detection band. The investigation of Kimble *et al.* was restricted to simple position meters. It was shown by Harms *et al.* [255] and Buonanno & Chen [129] that such filters applied to optical spring interferometers also allows a broadband quantum noise reduction by squeezed light. Unfortunately, quite generally two low-loss, narrow-bandwidth, and therefore long-baseline optical filter cavities are necessary to prepare the squeezed states in an optimum way. The generation of frequency-dependent squeezing utilizing one filter cavity was experimentally characterized by Chelkowski *et al.* [156] followed by the shot noise reduction of a table-top dual-recycled Michelson interferometer demonstrated by Vahlbruch *et al.* [534]. Another way to achieve an enhancement in the high frequency range without drastically ~~worsen~~ the low frequency sensitivity by avoiding the use of multiple long base-line filter cavities was proposed by Corbitt *et al.* [169]. Here, the use of a tuned Fabry-Perot cavity with two partly transparent mirrors was suggested acting ~~has~~ high-pass filters (termed amplitude filters within this context) for the squeezed field. In reflection of this filter cavity the squeezing at sideband frequencies beyond the filter cavity bandwidth is preserved whereas at low frequencies the squeezing is lost and replaced by ordinary vacuum noise. Since any optical loss of the filters mainly affects the transmitted part, the baseline of the filters can be chosen comparatively small. It has already been realized quite early that there is a transition region between the reduced noise at high frequencies and the non-increased noise at low frequencies, where the sensitivity is degraded. Later, this degradation was explained by information loss at the end mirror of the filter cavity and an additional homodyne detection was proposed ~~to~~ capturing this information [298]. Furthermore, it has been proposed to inject additional squeezed vacuum through the filter cavity end mirror and thus suppress also the low-frequency radiation-pressure noise [300]. However, these techniques are more useful for simple position meters and are intended to be installed as a low-cost add-on during the life cycle of the second generation detectors [301], since the rotation of the squeezing ellipse around the optical resonance of optical spring interferometers cannot be compensated by these filters leading to a ~~decreased~~ sensitivity which can be even below that of the interferometer ~~w/o~~ input-squeezing. For speed meter interferometer the quantum noise can be reduced by input-squeezing analogously to a position meter with filter cavities [427]. But here it is also possible to achieve an enhancement at lower frequencies without drastically ~~worsen~~ the high frequency sensitivity avoiding the use of filter cavities [201]. Furthermore, it has been experimentally verified that the shot-noise limited sensitivity of a zero-area Sagnac interferometer can be enhanced by input-squeezing [201]. In Fig. 145 and Fig. 146 one finds examples of quantum noise spectral densities (dashed curves) for optical spring and speed meter interferometer with frequency-dependent input squeezing in the ideal case of no optical loss.

Additionally, all main interferometer detectors can be equipped with a balanced homodyne detection and with the **variational-output** technique, which was invented conceptually in the early 1990s by Vyatchanin, Matsko and Zubova [554, 555] and later substantiated by Kimble *et al.* [306]. Here filter cavities are used to make the quadrature angle of the detected output field frequency dependent and therefore realize a broadband evasion of the radiation-pressure noise. Even though the most efficient combination of frequency-dependent input-squeezing and variational-output for the optical spring interferometer cannot be realized with Kimble-filters, different semi-optimal configurations have been found [129]. Especially at low frequencies, variational output with frequency-independent input-squeezing can in principle improve the sensitivity much more than frequency-dependent input-squeezing, but on the other hand optical losses in the filter cavities for the variational-output become even more severe [161, 306]. When the radiation-pressure noise is strong, it is required to bring enough of the quadrature without signal-content into the output in order to cancel the radiation-pressure noise and this introduces significantly higher noise due to optical losses. Moreover, optical losses in the filters remove parts of the ~~at~~ low frequencies already weak signal from the output. In Fig. 145 and Fig. 146 there are examples for quantum noise spectral densities (dotted curves) of variational readout interferometers in the ideal case of no optical loss given. For more details refer to Ref. [377].

5.5.2 Chosen design topology and configuration

The actual design topology and configuration for the Einstein telescope gravitational-wave detector has to be carefully chosen among the possible candidates. Not only the ideal quantum noise performance of the different candidates (cf. Sec. 5.5.1) has to be taken into account, also degradation due to optical loss and

technical problems in the realizability have to be considered [377]. Neither realization of an optical speed meter interferometer is actually enough explored and each has certain technical problems: INPUT FROM ANDREAS FREISE AND STEFAN HILD IS NEEDED! Moreover, theoretical studies and considerations of the feasibility of certain advanced techniques including realistic optical loss suggest that the desired sensitivity for the total observation band of the Einstein telescope gravitational-wave detector cannot be covered by a single interferometer. The variational readout technique applied to an optical spring interferometer as well as to a Sagnac interferometer with detuned signal-recycling could in the ideal situation provide a single broadband detector [377] but considering realistic values for optical losses (in particular, the quantum inefficiency of the photo detector) destroy the quantum correlation, abolish thus the quantum noise cancellation and degenerate the signal (see dotted curve in Fig. 145 and Fig. 146). Optical transducer detectors are much less sensitive to optical loss [161] and require much less power for the detection. But an important implementation issue is the fact that the actual sensitivity of the detector depends strongly on the sensitivity of the local meter, a completely not yet developed part (cf. e.g. Ref. [161] and references therein).

It has been suggested to split the detection band into two frequency bands, each covered by a single interferometer, which are optimized on that specific frequency band, forming altogether a so-called xylophone interferometer [267] covering the full detection band. Especially from the technical point of view it might be unavoidable to consider separately a low-power, cryogenic interferometer optimized for the low-frequency band and a higher-power, room-temperature interferometer covering the high-frequency band, avoiding in this way that high-power laser beams have to be transmitted through cryogenic optics (cf. Sec. ???). For the high-frequency interferometer the obvious choice is an upscaled but otherwise only moderately advanced version of a second generation interferometric gravitational-wave detector, a simple position meter. Furthermore, at the moment the most favored candidate for the low-frequency part of the full detector is, especially in terms of feasibility, an squeezed-light enhanced optical spring interferometer, which can be optimized in order to fit the low-frequency classical noise profile. This requires the injection of frequency-dependent squeezed states of light, created by two filter cavities. Filter cavities are a key feature in the development of quantum-noise-reduction methods for future gravitational-wave detectors, therefore, we will discuss technical aspects of the filter cavities in Sec. ???. For a later upgrade state of the detector, a speed meter seems to be a promising alternative for the low-frequency part – after a successful prototyping stage. More details of the chosen configuration will be given in Sec. ???.

5.6 Quantum noise reduction with squeezed states of light

Author(s): Andre Thuering, Helge Mueller-Ebhardt, Keiko Kokeyama

At first glance, quantum physics imposes a fundamental limit on metrology—the science of measurement—, and thus imposes a corresponding limit on the sensitivity of GW detectors. A fundamental problem in optical interferometry is the stochastic distribution of photons arriving at the photodiodes. This statistical fluctuations obscure the tiny power variations caused by GW signals. Fortunately, quantum physics also provides a solution to this problem via the concept of quantum entanglement.

“Quantum metrology” uses quantum entanglement to improve the measurement precision beyond the limit set by measurement counting noise. The first such proposal was made by C.M. Caves in 1981 when he suggested the use of squeezed states of light as an (additional) input for laser interferometric GW detectors [149]. Caves’s initial proposal was motivated by the limited laser power available at the time. Indeed, squeezed states allow for improvement in the sensitivity of a quantum noise limited interferometer without increasing the circulating laser power. **OVERLAP with Sec.5.5.1**

Squeezed states [117, 193, 557, 575] belong to the class of so-called *nonclassical* states of light. Generally, nonclassical states are those that cannot be described by a classical (positive valued) probability distribution using the coherent states as a basis (the P -representation) [235]. Let us first consider the coherent states. If light in a coherent state is absorbed by a photodiode, mutually independent photon ‘clicks’ (in terms of photo-electrons) are recorded, a process that is described by a Poissonian counting statistics. Due to quantum

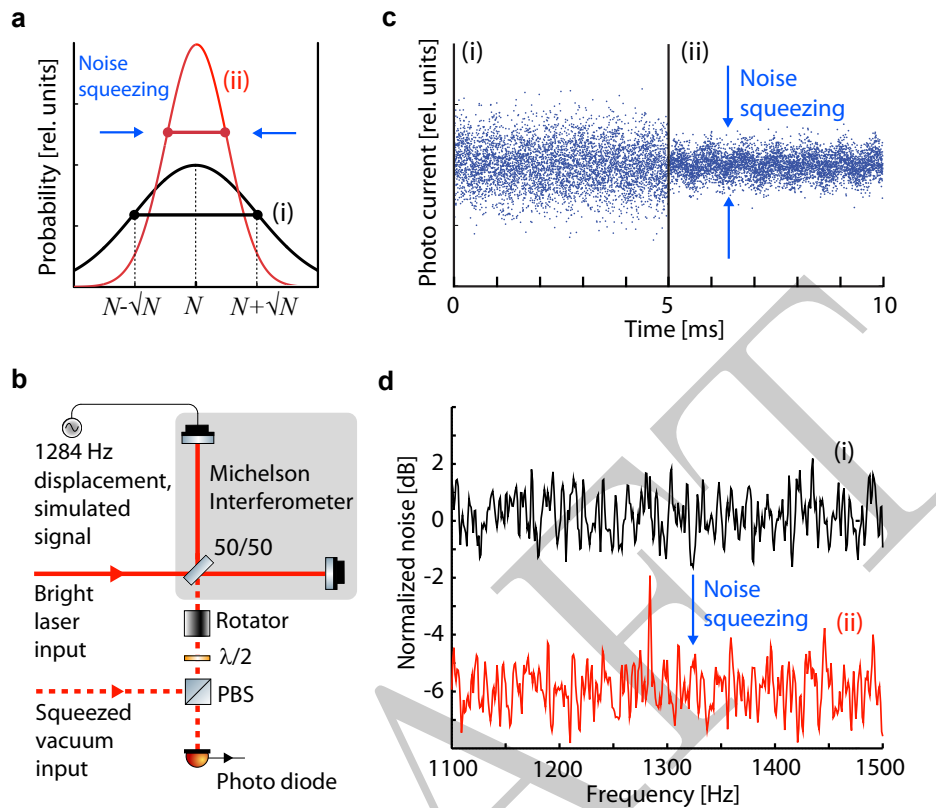


Figure 147: Squeezed light enhanced metrology (a) For large photon numbers N , squeezed light shows a photon counting statistic with a standard deviation smaller than $\pm\sqrt{N}$. In all panels, (i) correspond to shot-noise and (ii) to 6 dB squeezed noise. (b) A squeezed vacuum beam is injected into the dark signal port of a Michelson interferometer, in addition to the conventional bright laser input. The squeezed beam leads to path entanglement of the light fields in the two arms and to an improved signal to noise ratio, as shown on the right. Without squeezing, the optical path length modulation at 1284 Hz is neither visible in the time series of the photo-electron current (c, simulation by B. Hage, AEI) nor in its noise power spectrum (d, measurement, courtesy of H. Vahlbruch, AEI [533]). In (c) as well as in (d), the signal is clearly visible when squeezing is applied (ii).

mechanics, every individual ‘click’ is not predictable, but rather the result of a truly random process. If the number of photons per time interval is large ($N \gg 1$), its standard deviation is given by \sqrt{N} , see Fig. 147 a (i). This uncertainty gives rise to *shot-noise*. For a *squeezed* light beam, the detection of photons are not time-independent but instead contains quantum correlations. Nevertheless, the photon statistics still cannot be predicted by some external clock. They instead show auto-correlations that give rise to a reduced standard deviation, as shown in Fig. 147 a (ii). The correlations might be described in the following way. Whenever the quantum statistics might drive the actual photon number above the average value N , a similar number of photons destructively interferes with the main body of photons providing a (partial) compensation of the fluctuation. These quantum correlations *squeeze* the interferometer’s shot-noise below its natural value. Another complementary way of describing the properties of squeezed states is based on the phase space quasi-probability distribution using the amplitude and phase quadratures of a light wave (the Wigner function) [235, 557].

A squeezed state that contains only quantum-correlated photons with no coherent amplitude is called a *squeezed vacuum state* [235]. If such a state is overlapped with a coherent laser beam on a semi-transparent beam splitter, two beam splitter outputs are generated which are quantum correlated. As a consequence, the overall (bi-partite) quantum state cannot be written in terms of products of the two beam splitter output states. Such a quantum state is called non-separable or *entangled*. This is exactly what happens if a squeezed state is injected into the

signal output port of a laser interferometer for GW detection (Fig. 147 b). The two *high-power* light fields in the interferometer arms get entangled and the light's quantum fluctuations in the two arms are correlated with each other. Although the fluctuations are not predictable from the outside, they provide an improved signal-to-noise ratio in the interferometer. Recall that an interferometer measures the optical path length change in one interferometer arm with respect to the other arm. If the quantum noise in the two arms is correlated it will cancel out. This entanglement interpretation was not discussed in the initial proposal by Caves. Nevertheless, it shows that the application of squeezed states in interferometers is a real application of quantum metrology by its very own definition. The entanglement produced by splitting a squeezed state at a semi-transparent beam splitter was tomographically characterized and quantified in [190]. Fig. 147 c shows a simulated signal from a photodiode, without (i) and with (ii) *squeezing*. The tiny modulation in the interferometer's output light due to the (simulated) passing GW is visible only with the improved signal-to-noise ratio. Fig. 147 d shows the analogue in frequency space, i.e. after a Fourier transform of the photo current was applied.

The above paragraph shows that squeezed states can be conveniently combined with the extremely high photon numbers of coherent light to improve a laser interferometer, as proposed in [149] and shown in Fig. 147 b. In fact, the stronger the squeezing factor [235, 557] the greater the path entanglement and the signal-to-noise improvement.

Overlap with Sec. 5.5.1. Shortly after Caves proposed squeezed states of light for laser interferometers in 1981, the first experimental demonstration of squeezed light [494] and proof of principle demonstrations of quantum metrology were achieved [241, 572]. In parallel, it was theoretically discovered that squeezed states offer even more advances in metrology than 'just' reducing the quantum shot-noise. From the early days of quantum physics, when fundamental aspects of the measurement process were discussed, it was clear that, in general, a measurement disturbs the system to be measured [110]. The measurement of quantity A (say a position of a mirror) increases the uncertainty of the non-commuting quantity B (say the mirror's momentum). Both observables are linked by a Heisenberg Uncertainty relation. For repeated measurements of A , the increased uncertainty in B disturbs the measurement of A at later times. This is referred to as *quantum back-action noise*. Here, the back-action arises from the fluctuating radiation pressure due to the reflected light [151]. It is significant if the mirror's mass is low and a large photon number is reflected. In the 1970s, ideas were developed that showed how, in principle, back-action noise for continuous measurements can be avoided. Such schemes were called quantum-non-demolition (QND) measurements [111, 512]. However, for laser interferometric GW detectors using *quasi-free* falling mirrors it remained unclear if QND schemes exist. In [149, 151] it was concluded that back-action noise of a free mass position measurement can in principle not be avoided and, together with photon counting noise, defines a *standard quantum limit* (SQL). In [531, 576] it was argued, however, that measurements below the SQL of a free mass are indeed possible. The discussion remained controversial [150] until Jaekel and Reynaud [284] were able to convincingly show that ~~the cleverly~~ arranged squeezed states in a GW detector can simultaneously reduce the shot-noise and the radiation pressure noise, by almost arbitrary amounts (as long as most of the photons belong to the light's coherent displacement).

So far no experiment has achieved a position measurement with sensitivity even at, let alone below, its standard quantum limit. Eventually this will be achieved, possibly first in future gravitational wave detectors. Advanced detectors are in fact designed to have a sensitivity at or just below their SQLs. Once the SQL is reached a new level of quantum metrology is achieved, because the position-momentum uncertainty of the mirror becomes correlated with the quadrature uncertainty of the reflected optical field. In this way, entanglement between the mechanical and the optical system can be observed [550]. This is all the more remarkable from the perspective of GW detectors since we are talking about mirrors with masses of 40 kg, planned for the upcoming improvement to LIGO - the Advanced LIGO [257], and even in the order of a 100 kg concerning the envisaged LF-detector of ET. Eventually, even two such mirrors might be projected via entanglement swapping [411] into an entangled state [376]. Obviously quantum metrology opens the possibility for further studies of the peculiarities of quantum physics at a macroscopic scale.

5.6.1 Squeezed light for Gravitational wave astronomy

Laser interferometers for GW astronomy are facing extreme sensitivity requirements that can only be achieved if all available tools, inclusive of quantum metrology, are combined in an elaborate measurement device. Squeezed light must be generated in a non-linear interaction. Squeezed light was first produced in 1985 by Slusher et al. using four-wave-mixing in Na atoms in an optical cavity [494]. Shortly after, squeezed light was also generated by four-wave-mixing in an optical fibre [480] and by parametric down-conversion in an optical cavity containing a second order non-linear material [571]. In these early day experiments, squeezing of a few percent to 2 to 3 dB were routinely observed (For an overview of earlier experiments and squeezed light generation in the continuous-wave as well as pulsed regime please refer to Ref.[53]).

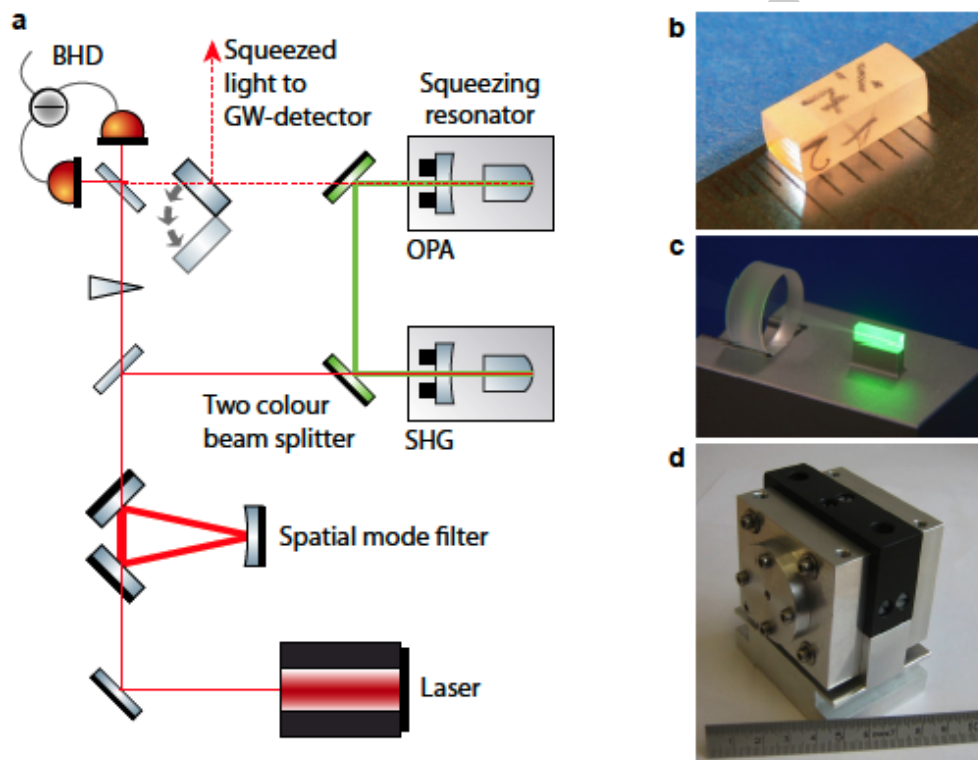


Figure 148: Generation of squeezed light (a) A continuous-wave laser beam at the GW detector wavelength is first spatially filtered and then up-converted to a field at half the wavelength (second harmonic generation, SHG). That beam is then mode-matched into the ‘squeezing resonator’ in which a tiny fraction of the up-converted photons are spontaneously down-converted by optical parametric amplification (OPA) producing a squeezed vacuum state. The squeezing factor is validated by a balanced homodyne detector (BHD). SHG as well as OPA are realized by a non-linear crystal (b), here a 6 mm long MgO:LiNbO₃ crystal, inside an optical resonator (c) formed by an external cavity mirror and the dielectrically coated crystal back surface. The two non-linear resonators may be constructed in an identical way and are put into temperature stabilized housings (d).

GW detectors are operated with high-power, quasi-monochromatic continuous-wave laser light with an almost Fourier-limited spatial distribution of a Gaussian TEM₀₀ mode. For a non-classical sensitivity improvement, squeezed light in exactly the same spatio-temporal mode must be generated and mode-matched into the output port of the interferometer [149], providing interference with the high-power coherent laser beam at the interferometer’s central beam splitter. High-power lasers for GW astronomy are based on optically pumped solid-state crystals in resonators [216], suggestive of a similar configuration for a “squeezed light resonator”. Fig. 148 (a) shows a schematic setup for generation of squeezed light that is built upon one of the very first squeezing experiments [571], a setup that has been used in many experiments thereafter [100, 224, 325, 471]. The setup uses

a solid state laser similar to those used as master lasers in high-power systems. After spatial mode filtering, second harmonic generation (SHG) in an optical cavity containing a second-order non-linear crystal is applied to produce laser light at twice the optical frequency. The second harmonic light is then mode-matched into the squeezing resonator to pump a degenerate optical parametric amplifier.

Fig. 148 (b-d) show photographs of the non-linear crystal, the optical arrangement and the housing of a squeezing resonator. The crystal is temperature stabilized at its phase matching temperature. At this temperature the first-order dielectric polarization of the birefringent crystal material with respect to the pump is optimally overlapped with the second-order dielectric polarization of the resonator mode at the fundamental laser frequency. This ensures a high energy transfer from the pump field to the fundamental Gaussian TEM₀₀ resonator mode, i.e. efficient parametric down conversion.

Initially, the resonator mode is not excited by photons around the fundamental frequency, i.e. it is in its ground state, characterized by vacuum fluctuations due to the zero point energy [235]. Note that the process is typically operated *below* oscillation threshold in order to reduce phase noise coupling from the pump [443]. This setup produces a squeezed vacuum state [235]. The down-converted photon pairs leaving the squeezing resonator exhibit quantum correlations which give rise to a squeezed photon counting noise when overlapped with a bright coherent local oscillator beam. The squeezed field is detected by interfering it with a coherent local oscillator beam, either in a balanced homodyne detector (BHD), see Fig. 148 (a), or when injected into a GW detector and detected with a local oscillator from the GW detector along with an interferometric phase signal, see Fig. 147. The closer the squeezing resonator is operated to its oscillation threshold, and the lower the optical loss on down-converted photon pairs, the greater the squeezing factor is. For instance, the observation of a squeezing factor of 2 is only possible if the overall optical loss is less than 50% [53]. **A 90% nonclassical noise reduction, i.e. a squeezing factor of 10, or 10 dB already limits the allowed optical loss to less than 10%.**

Although squeezed light was demonstrated in the 1980s shortly after the first applications were proposed [480, 494, 571], several important challenges pertaining to the application of squeezed states to GW detectors remained unsolved until recently.

First, squeezing has always been demonstrated at Megahertz frequencies, where technical noise sources of the laser light is not present. At this frequencies, the laser operates at or near the shot-noise limit. In the 10 Hz to 10 kHz band where terrestrial GW detectors operate, technical noise masked and overwhelmed the observation of squeezing. For example, acoustic, laser relaxation oscillation thermal and mechanical fluctuations can be many orders of magnitude larger than shot noise. Until recently, it was not certain that a laser field could even be squeezed and matched to the slow oscillation period of GWs. Second, it was previously not known whether squeezed light was fully compatible with other extremely sophisticated technologies employed in GW detectors, such as signal-recycling. Third, the technology to reliably produce stable and strong squeezing with large squeeze factors was lacking. Long term observation of strong squeezing was a technical challenge until recently.

These challenges have all been overcome in the past decade. All the open questions have now been satisfactorily addressed. This development is very timely since many known advanced classical interferometric techniques have almost been exhausted. Many remaining classical improvements are becoming increasingly difficult and expensive to implement.

Generation of squeezing in the audio-band A major breakthrough in achieving squeezing in the audio band was the insight that the dominant noise at audio frequencies that degrades squeezed light generation couples via the coherent laser field that was used to control the length of the squeezed light laser resonator, whereas noise coupling via the second harmonic pump field is insignificant [99, 469]. This led to the first demonstration of audio-band squeezing at frequencies down to 200 Hz [355], see Fig. 149 a. There the length of the squeezing resonator was stabilized without a bright control beam by using the phase sensitivity of the squeezing itself – a technique known as quantum noise locking [356]. Subsequently a coherent beam control scheme was invented [535] for simultaneous control of both the squeezing resonator length and the squeezing angle [235]. Shortly thereafter another noise source was identified and mitigated, which allowed for squeezing of more than 6 dB throughout the audio-band down to 1 Hz [532]. This noise source arose due to tiny numbers of

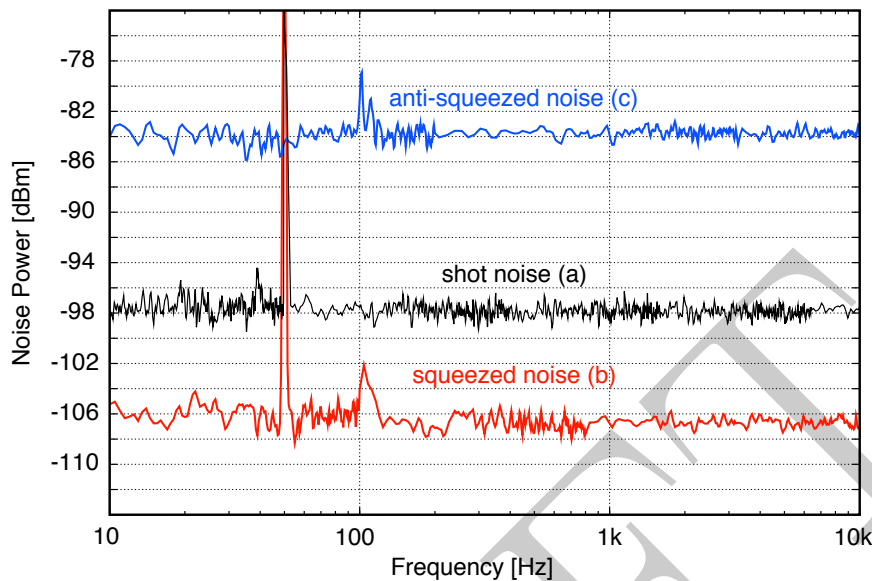


Figure 149: Quantum noise squeezing The spectral analysis of measured noise powers without (i) and with ‘squeezing’ (ii). The horizontal sections of traces (i) correspond to shot-noise, serving as reference levels (0 dB), respectively. Current best performance of a squeezed light laser for GW detection shows an up to 9 dB squeezed noise over the complete detection band of ground-based GW detectors [537].

photons that were scattered from the main laser beam and rescattered into the audio band squeezing mode after having experienced a frequency shift due to vibrations and thermal expansions of potential scattering surfaces, an effect known as *parasitic interferences*. Since bright laser beams cannot be completely avoided, the recipe for the generation of audio-band squeezing turned out to be fourfold: avoiding scattering by using ultra-clean super-polished optics, avoiding rescattering by carefully blocking all residual faint beams caused by imperfect anti-reflecting surfaces, reduce the vibrationally thermally excited motion of all mechanical parts that could potentially act as a re-scattering surface and avoid pointing fluctuations [358].

Compatibility of squeezing with other interferometer techniques Current detectors achieve their exquisite sensitivity to GWs due to their kilometre-scale arm lengths, the enormous light powers circulating in the enhancement resonators (arm, power- and signal-recycling cavities), and sophisticated pendulum suspensions that isolate the test mass mirrors from the environment (Fig. ??). When these techniques were developed, squeezing was not envisioned to become an integrated part of such a system. Building on existing theoretical work [231, 255], a series of experimental demonstrations of squeezed state injection into GW detectors were carried out. These included compatibility with power recycling, with signal recycling [354, 534], and with the dynamical system of suspended, quasi-free mirrors [238, 470].

Generation of strong squeezing Squeezing has significant impact in quantum metrology if large squeezing factors can be produced. Squeezing of 3 dB improves the signal-to-noise ratio by a factor of $\sqrt{2}$, equivalent to doubling the power of the coherent laser input. Squeezing of 10 dB corresponds to a ten-fold power increase. Remarkably, the experimentally demonstrated squeezing factors have virtually exploded in recent years [417, 505, 536], culminating in values as large as 12.7 dB [201]. All the squeezing factors above 10 dB were observed with monolithic resonators and at MHz frequencies. However, reduced optical loss in non-monolithic resonators and a careful elimination of parasitic interferences should in principle enable such factors also in the GW band. An 8 to 10 dB improvement based on strong squeezing seems realistic for future GW detectors in their shot-noise limited band [201].

So far, strong squeezing values have been reported for a wavelength of 1064 nm. However, the procedure of squeezed light generation is also applicable for the wavelength of 1550 nm that will be required for future,

cryogenic GW detectors. Recently, the generation of squeezing at a wavelength of 1550 nm was reported in a first proof-of-principle experiment [360]

The first squeezed light laser for GW detection Based on the previous achievements reviewed here, very recently, the first squeezed light laser for the continuous operation in GW detectors was designed and completed [533, 537]. Up to 9 dB of squeezing over the entire GW detection band has been demonstrated (Fig. 149b). This laser produces squeezed vacuum states and is fully controlled via co-propagating frequency-shifted bright control beams. This 9 dB squeezing factor is limited by technical effects: The squeezing resonator has to have an adjustable air gap to allow for an easy way to apply length control. The anti-reflection coated surface in the resonator introduces additional loss and reduces the escape efficiency. Moreover, a Faraday isolator has to be used in the squeezed beam path in order to eliminate parasitic interferences. This rotator produces a single pass photon loss of about 2%. This squeezed light source is designated for continuous operation in the GEO600 GW detector. A squeezed light source based on a design that should have less sensitivity to retro-scattered light [357] is being prepared for deployment on one of the most sensitive detectors, the 4 km LIGO detector in Hanford, Washington.

5.7 Filter cavities

The necessity of filter cavities for a broad band quantum noise reduction with squeezed state of lights was described in Secs 5.5.1, 5.6 and 5.6.1. In the following Sections, technical requirements for these optical filters are discussed. An important point is the required baseline length of these filter cavities in view of their optical round-trip loss (Sec. 5.7.1). The tolerances of the determined design parameters will be discussed in Sec. 5.7.2. Furthermore, in Sec. 5.7.3 the optical layout with regard to the round-trip loss that will be mainly caused by scattering at the used imperfect mirrors is treated. Finally, the degradation of the squeezing level due to noise couplings (e.g. displacement noise in the filter cavities) will be analysed in Sec. 5.7.4 leading to further estimates for the requirements.

5.7.1 Restrictions for the baseline length of the filter cavity

The required half-bandwidth γ_{fc} and detuning Φ_{fc} (note that we will define them as angular frequencies) of the filter cavities giving the optimal frequency dependent squeezing angle are determined by the interferometer configuration and its induced phase-space rotation of light fields entering the interferometers output port.

Generally, any round-trip loss will degrade the squeezing level at sideband frequencies being resonant in the filter cavity. For a given round-trip loss $l_{rt,fc}^2$ (mainly caused by scattering) the resulting loss in reflection of the filter cavity increases with a decreasing baseline length L_{fc} of the filter. As well, for a certain length L_{fc} and a certain round-trip loss $l_{rt,fc}^2$ the loss imposed on the squeezed field increases with a decreasing half-bandwidth γ_{fc} that needs to be realized. Starting from the expression for the half-bandwidth of a lossy cavity

$$\gamma_{fc} = \frac{c}{2L_{fc}} \arccos \left(1 - \frac{(1 - \rho_c \sqrt{1 - l_{rt,fc}^2})^2}{2\rho_c \sqrt{1 - l_{rt,fc}^2}} \right) \quad (157)$$

one can derive the filter cavity's coupling mirror reflectance $R_c = \rho_c^2$ that is required to achieve the targeted half-bandwidth. One obtains

$$\rho_c = \frac{1}{\sqrt{1 - l_{rt,fc}^2}} \left[2 - \cos(\mathcal{F}') - \sqrt{\cos^2(\mathcal{F}') - 4 \cos(\mathcal{F}') + 3} \right] \quad (158)$$

with

$$\mathcal{F}' = \frac{2\gamma_{fc}L_{fc}}{c} = \frac{\gamma_{fc}}{\text{FSR}_{fc}} = \frac{\pi}{\mathcal{F}_{fc}}. \quad (159)$$

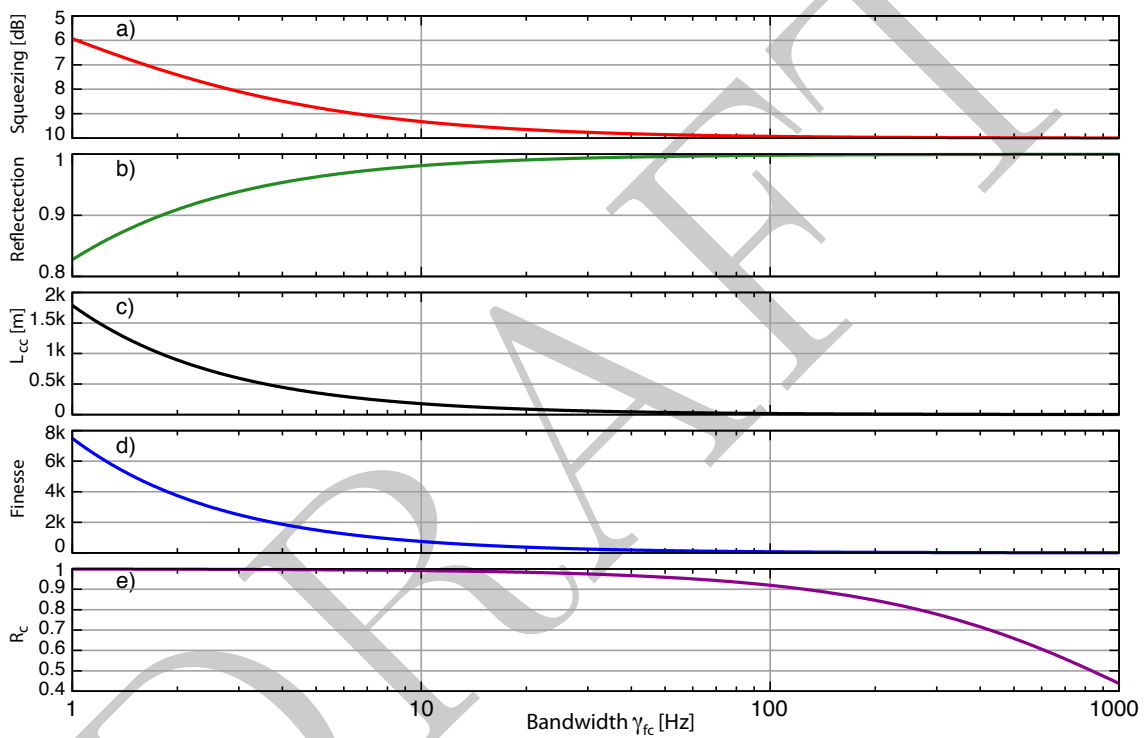


Figure 150: Filter cavity properties in dependence of its half-bandwidth γ_{fc} . a) the remaining squeezing level in reflection of the filter cavity and b) its reflectance at the frequency $\Omega = \Phi_{fc} L_{fc}/c$. In c) the value for L_{cc} is shown according to Eq. (162). Curve d) shows the Finesse and e) the coupling mirror reflectance R_c given by Eq. (158). For all traces a filter cavity length $L_{fc} = 10$ km and a round-trip loss $l_{rt,fc}^2 = 75$ ppm was assumed. The initial squeezing level was considered with 10 dB. It can be seen that the impact of the round-trip loss becomes significant for $\gamma_{fc} < 2\pi \cdot 10$ Hz.

Graph e) in Fig. 150 shows the value for $R_c = \rho_c^2$ according to Eq. (158). In the underlying calculations the baseline length L_{fc} and the round-trip loss $l_{rt,fc}^2$ were considered with 10 km and 75 ppm, respectively. The tuning of the filter cavity was exemplarily set to $\Phi_{fc} = \gamma_{fc} L_{fc}/c$. It can be seen, that for small half-bandwidths γ_{fc} the reflectance R_c comes close to unity. Correspondingly, the resulting Finesse rises as shown in Graph d). It can be seen from Eq. (158) that there are two fundamental restrictions for the choice of the filter cavity length. First, for great values of the Finesse (i.e. for small half-bandwidths) we obtain

$$\lim_{\gamma_{fc} \rightarrow 0} \rho_c = \frac{1}{\sqrt{1 - l_{rt,fc}^2}} > 1 \quad (160)$$

which does not represent a physical solution. Thus, there must exist a value L_{min} such that for $L_{min} < L_{fc}$ we always have $\rho_c < 1$. The expression for L_{min} can be derived to

$$L_{min} = \frac{c}{2\gamma_{fc}} \arccos \left[2 - \frac{2 - l_{rt,fc}^2}{2\sqrt{1 - l_{rt,fc}^2}} \right]. \quad (161)$$

Second, for $L_{fc} < L_{cc}$ we obtain $\rho_c > \sqrt{1 - l_{rt,fc}^2}$ and the filter cavity becomes under-coupled. But even in the most general case, the interferometer represents an over-coupled cavity. Hence, an under-coupled filter cavity with $L_{fc} < L_{cc}$ can not provide the phase-space rotation required for the generation of the optimal squeezing angle.

To keep $\rho_c < \sqrt{1 - l_{rt,fc}^2}$ the filter cavity length needs to be

$$L_{fc} > L_{cc} = \frac{c}{2\gamma_{fc}} \arccos \left[2 - \frac{1 + (1 - l_{rt,fc}^2)^2}{2(1 - l_{rt,fc}^2)} \right] \quad (162)$$

Please note that for $L_{fc} = L_{cc}$ the filter cavity is critical coupled (impedance matched) and the loss in its reflection is maximum. Therefore, to preserve the squeezing in reflection of the filter cavities its length should be chosen with $L_{fc} \gg L_{cc}$. This fact becomes obvious when looking at graph a) and b) of Fig. 150. They show the squeezing level in reflection of the filter cavity and the according reflectance of the filter cavity at its resonance frequency, respectively. At small half-bandwidths the value for L_{cc} (graph c)) is of the order of the filter cavity's baseline length $L_{fc} = 10$ km and hence the reflectance and accordingly the remaining squeezing level are considerably reduced.

In Fig. 151 the filter cavity performance is shown depending on its baseline length L_{fc} . In the corresponding calculations we assumed the target half-bandwidth with $\gamma_{fc} = 2\pi \cdot 1.4$ Hz and the target detuning with $\Phi_{fc_1} = 2\pi \cdot 6.6$ Hz $\cdot L_{fc_1}/c$. Note, that these values are the requirements for one of the filter cavities that need to be realised in the ET-LF detector [?]. Again, the round-trip loss was considered with 75 ppm and the initial squeezing level with 10 dB. Graph a) demonstrates, that even with a filter cavity length of 10 km the amount of squeezing is already reduced by a factor of about 3 dB. At the critical length $L_{fc} = L_{cc} \approx 1239$ m the remaining squeezing is merely about 3 dB. For even shorter filter cavities the squeezing increases again (grey shaded area II) until it reaches at $L_{fc} = L_{min}$ the initial level of 10 dB. However, in this region the filter is under-coupled and does not yield the required phase-space rotation of the squeezed field. This can be understood when considering the extrem case for $L_{fc} = L_{min}$. Here, R_c is equal to one and the filter cavity can be replaced by an ordinary mirror that has no frequency dependence. Again, it can be deduced, that a filter cavity length $L_{fc} \gg L_{cc}$ needs to be realised in order to preserve the squeezing. In addition, the high finesse of a short cavity might pose a problem for the lock acquisition in the environment of a gravitational-wave detector where the optics needs to be suspended.

So far in Figs. 150 and 151 the remaining squeezing level was shown at the resonance frequency of the considered filter cavities. Here the (frequency dependent) imposed loss is maximum. Now, for exemplification Fig. 152 shows squeezing spectra obtained after the reflection at two subsequent filter cavities FC₁ and FC₂. The

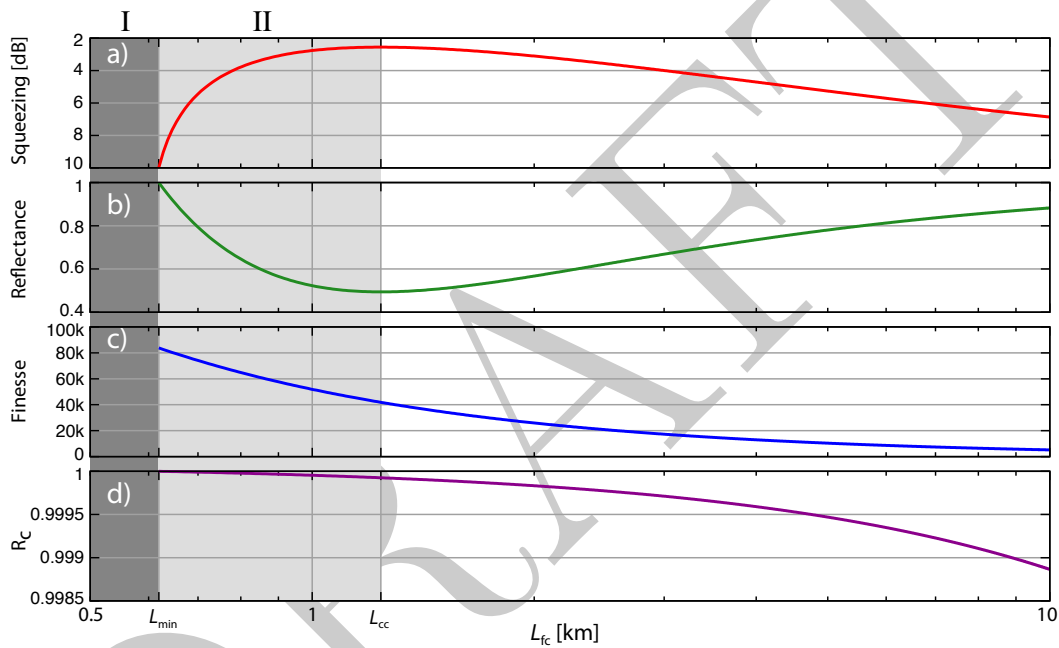


Figure 151: The figure shows the filter cavity performance in dependence of its baseline length L_{fc} . Graph a) shows the remaining squeezing level in reflection of the filter cavity at the filter cavities' resonance frequency. Graph b) shows the according reflectance of the filter cavity. Graph c) and d) show the filter cavity's Finesse and coupling mirror reflectance R_c , respectively. The two grey shaded areas highlight the region where $L_{fc} < L_{cc}$ (area II) and where $L_{fc} < L_{min}$ (area I). In the considered example ($\gamma_{fc} = 2\pi \cdot 1.4 \text{ Hz}$, $\Phi_{fc_1} = 2\pi \cdot 6.6 \text{ Hz} \cdot L_{fc_1}/c$, $l_{rt,fc}^2 = 75 \text{ ppm}$) the critical length L_{cc} is about 1335 m. At this length the squeezing level drops to about 3 dB. Furthermore it can be seen that for $L_{fc} < 5 \text{ km}$ the finesse exceeds the value of 10000. Such high-finesse suspended cavities might be difficult to stabilize.

considered half-bandwidths and tunings of these filters are those needed for the ET-LF detector. The length of the cavities were considered with $L_{fc_1} = L_{fc_2} = 2$ km (red curve), $L_{fc_1} = L_{fc_2} = 5$ km (blue curve) and $L_{fc_1} = L_{fc_2} = 10$ km (green curve), respectively.

The calculations and exemplary filter properties considered within this section imply, that in 3rd generation GWADS detectors such as the Einstein Telescope, where filter cavities with half-bandwidths in the range of $\gamma_{fc} \approx 2\pi \cdot 1 - 2\pi \cdot 5$ Hz will be required, the baseline length of these filters needs to be in the order of a few kilometers. This contrasts to the results presented in [300] for the aLIGO detector. As for the aLIGO configuration filter cavities with half-bandwidths in the order of $2\pi \cdot 50 - 2\pi \cdot 200$ Hz will be required, a considerable sensitivity increase by the injection of frequency dependent squeezed light can already be achieved if filter cavities with lengths in the order of 100 m are utilised. Certainly, our exemplary calculations are based on a conservative assumption of 75 ppm for the round-trip loss of the filter cavities, but even if optimistic values of $l_{rt,fc}^2 = 20$ ppm are considered, the corresponding values for the critical lengths will be $L_{cc,fc_1} = 330$ m and $L_{cc,fc_2} = 84$ m, respectively. As shown in Figs. 150 and 151 the respective length L_{fc} should be at least 10 times greater than L_{cc} . I.e. for the ET-LF detector the length of the two required filter cavities should be realised with 10 km. In contrast, it can be shown that for the ET-HF detector a filter with a length of about 300 m is sufficient. This filter will be required for an optimisation of the squeezed quadrature in the radiation pressure noise dominated frequency band. However, in this frequency band other noise sources dominates the quantum noise. By that it is satisfactory to adapt the squeezing level to the level of these noise sources which will be possible with a comparatively short filter cavity.

The foregone investigation demonstrated that the round-trip loss ultimately restricts the minimal allowed baseline length and consistently the performance of the filter cavities. As it is expected that the round-trip loss of the filters will be dominated by scattering at imperfect mirror surfaces, the optical layout needs to be designed such that the amount of scattering is as much as possible reduced. The scattering in different optical layouts is treated in Sec. 5.7.3.

5.7.2 Robustness of the design parameters

In this Section we illustrate the effect of a deviation of the determined design parameters. We will concentrate on the most obvious quantities, that will potentially change the properties of the filter, i.e.

1. the reflectance factors of the used mirrors,
2. the round-trip loss,
3. the macroscopic length and
4. the resonance frequency.

The first three quantities affect the bandwidth of the filter cavity and thus the required phase-space rotation around the targeted resonance frequency. A deviation from the design values of these quantities could not be compensated if the filter cavity is realised as single resonator. An adaption of the filters bandwidth would be possible if coupled resonators– e.g. a linear coupled three-mirror cavity– are utilised. Although it should be always possible to tune the filter cavity to the required resonance frequency, for the sake of completeness we treat a potential mismatch within this section. From the results the requirements for the length stabilisation with regard to displacement noise could be determined. This will be described in Sec. 5.7.4 in detail.

We start from a set of design parameters for the length, the detuning and the mirrors reflectance factors yielding the bandwidth and phase-space rotation of the two filter cavities that are required for ET-C LF. These parameters are listed in Table 12. The analysis of the impact on the achievable squeezing levels for a certain mismatch of the bandwidths will give the allowable tolerances of these parameters.

To demonstrate the effect of a mismatched bandwidth we calculate the squeezing spectra after reflection at two subsequent resonators– the required filter cavity and an auxiliary cavity which models the interferometer. For the filter cavity the design parameters (and a certain deviation of them) as listed in Table 12 are assumed. The auxiliary one has a bandwidth and detuning that models the transfer function and thus the phase-space rotation

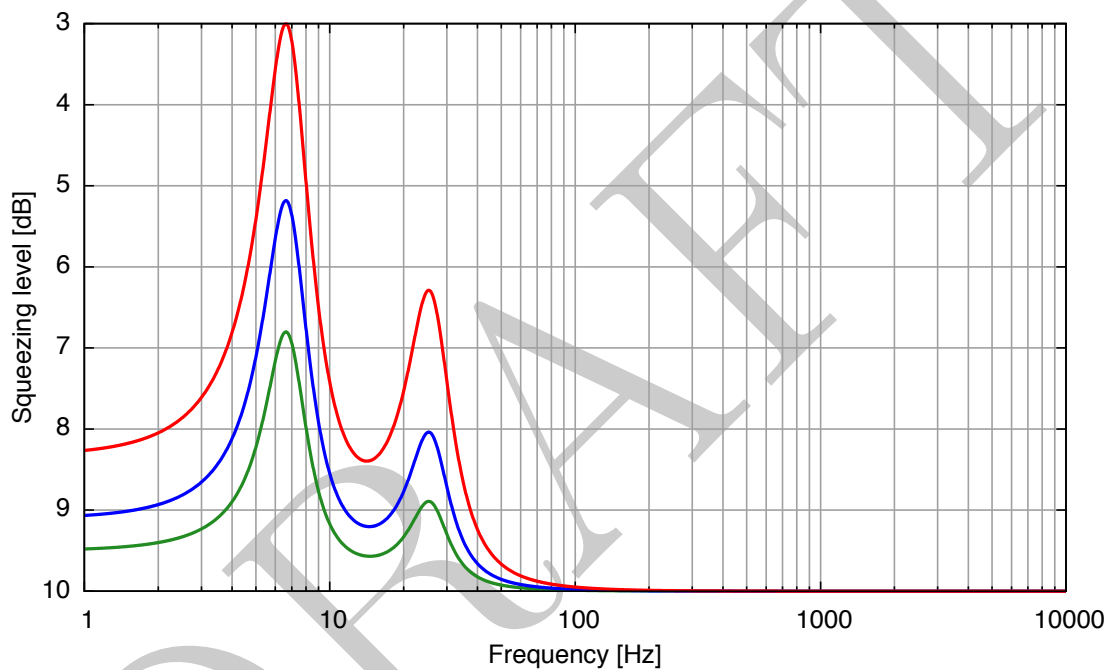


Figure 152: The figure shows the remaining squeezing level after reflection of two subsequent filter cavities FC_1 and FC_2 . Three cases were considered. The green curve is obtained for $L_{fc_1} = L_{fc_2} = 10$ km, the blue one for $L_{fc_1} = L_{fc_2} = 5$ km and the red one for $L_{fc_1} = L_{fc_2} = 2$ km. For each case the round-trip loss of the cavities was considered with 75 ppm. The filter parameters are those that are required for a broadband quantum noise reduction in the ET-LF detector, i.e. $\gamma_{fc_1} = 2\pi \cdot 1.4$ Hz, $\Phi_{fc_1} = 2\pi \cdot 6.6$ Hz $\cdot L_{fc_1}/c$ and $\gamma_{fc_1} = 2\pi \cdot 5.7$ Hz, $\Phi_{fc_1} = -2\pi \cdot 25.4$ Hz $\cdot L_{fc_1}/c$, respectively. In all cases, a white squeezed state with a quantum noise reduction of 10 dB was assumed. So far no additional propagation or detection loss was considered.

Parameter	FC ₁	FC ₂
length L_{fc} [km]	10	10
half-bandwidth γ_{fc} [Hz]	$2\pi \cdot 1.4$	$2\pi \cdot 5.7$
resonance frequency f_{res} [Hz]	$2\pi \cdot 6.6$	$-2\pi \cdot 25.4$
detuning Φ_{fc} [°]	≈ 0.1369	≈ 0.3026
round-trip loss $l_{rt,fc}$ [ppm]	75	75
coupling mirror reflectance R_c	99.8864 %	99.5323 %

Table 12: Design parameters / estimates for the two filter cavities FC₁ and FC₂ needed in the ET-C LF detector.

of the interferometer. Consistently, no phase-space rotation occur after subsequent reflection at these resonators if their bandwidths are matched. Note, that the auxiliary resonator is assumed to be loss-free so that the imperfections in the squeezing spectra can be clearly traced back to the respective deviation of the filter cavities design parameters. For an first illustration of the effect of a mismatched filter cavity's bandwidth, Fig. 153 shows the squeezing level (top) and the residual phase-space rotation (bottom) after subsequent reflection at both cavities. Note, that here *both* cavities were assumed to be loss-free.

Fig. 154 shows the performance of the filter cavities (FC₁ and FC₂) required for the ET- LF detector. Their bandwidth was varied according to a deviation of 1% to 5% from the designed value. In these plots, the round-trip loss of the filter cavities was considered with 75 ppm.

If a tolerable degradation of the squeezing by less than 2 dB (related to the squeezing levels achievable with the design parameters) is targeted, a deviation of the bandwidth by up to 5% is acceptable. From this value, the tolerances for the design parameters can be deduced.

5.7.3 Choosing the optical layout of the filter cavity

Author(s): K. Kokeyama

In this section, we compare the cavity geometry from the scattering-light noise point of view. The four geometries that are going to be compared: two-mirror cavity, triangular-cavity, rectangular cavity, and bow-tie cavity, as shown in Fig. 155. We categorize the scattering process into the following four kinds and derive the scattered field $\psi_{sc}(x, y, z_{sc})$ to obtain the coupling coefficient of the scattering field into the cavity resonant mode. Finally we will numerically evaluate the coupling coefficient for the four processes in each geometry.

To evaluate the effect of the scattering field, we calculate how much the scattered field couples into the cavity mode. The coupling factor between the scattered field is defined as a convolution between them:

$$X = \int_{-\infty}^{\infty} \int_{-\infty}^{\infty} \psi_{sc}(x, y, z_{sc}) \psi_{cav}^*(x, y, z_{cav}) dx dy, \quad (163)$$

where $\psi_{sc}(x, y, z_{sc})$ is the scattered-light field, z_{sc} is the location when the scattering process occurs, and z_{cav} is the locations of the target field coupled by the scattered light. $\psi_{cav}(x, y, z_{cav})$ is the Gaussian field which is the resonant mode in the cavity, and the scattered field $\psi_{sc}(x, y, z_{sc})$ coupled into this mode:

$$\psi_{cav}(x, y, z_{cav}) = \sqrt{\frac{k_0}{\pi z_R}} \frac{iz_R}{z + iz_R} \exp\left[\frac{-ik_0(x^2 + y^2)}{2(z + iz_R)}\right] \quad (164)$$

where z_R is the Rayleigh range of the cavity resonant mode and k_0 is the wave number of the laser. $\psi_{cav}(x, y, z_{cav})$ propagates in the normal or opposite direction ($+z$ or $-z$, respectively) depending on the scattered process (see following sections). Eq. (163) calculate the cross term between the scattered fields and the cavity resonant field since this cross term will appear on the photo detector when the light field is detected.

We consider following four kinds of scattering-coupling process, direct back scattering, diagonal path scattering I and II, and Gaussian tail effect.

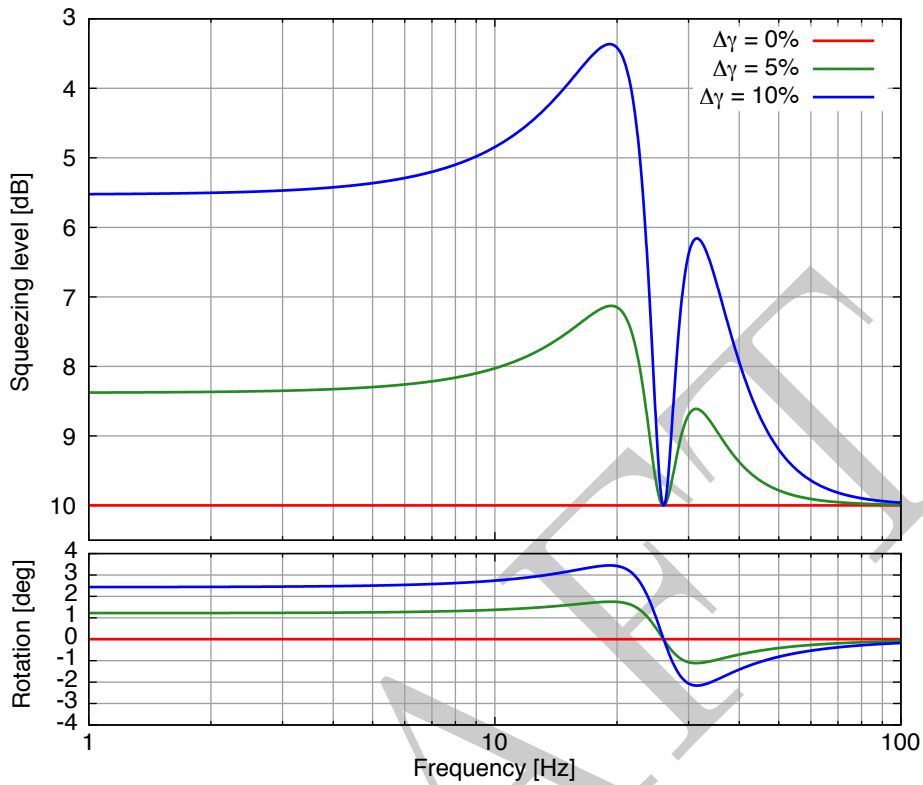


Figure 153: The figure illustrates the effect of a deviation of the required bandwidth. The lower graph show the resulting residual phase-space rotation of the squeezing ellipse, the upper graph the accordant squeezing levels. Please note, that the filter cavities are assumed to be loss less. Thus, the degradation of the squeezing level can be clearly traced back to the residual phase-space rotation.

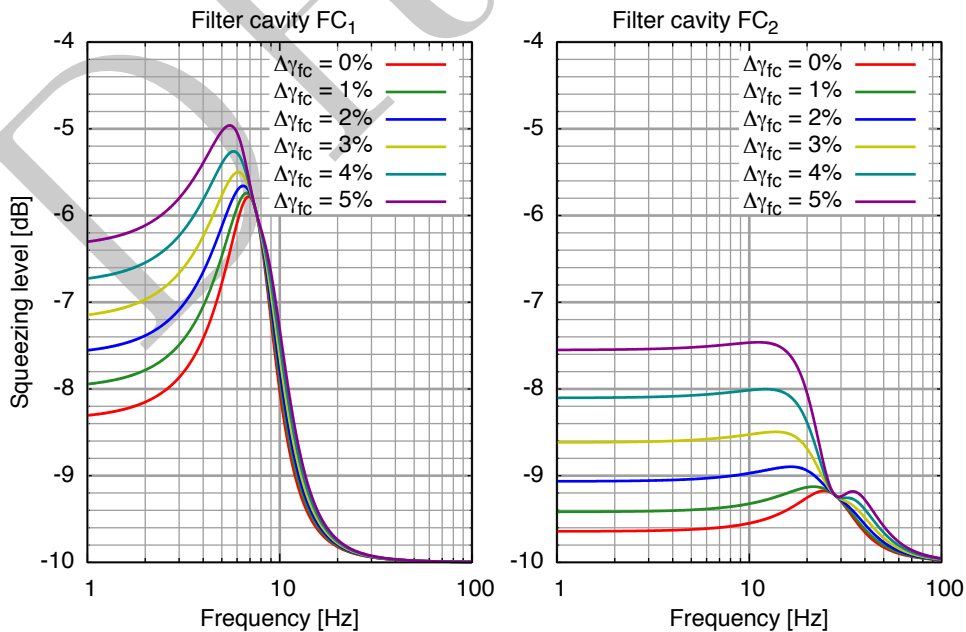


Figure 154: The figure shows the squeezing spectra for a deviation of the designed bandwidth of FC₁ (left) and FC₂ (right). Here, the filter cavities' round-trip loss was considered with 75 ppm.

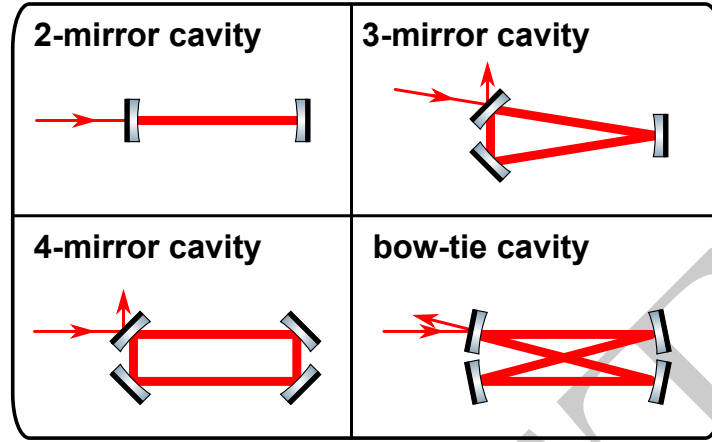


Figure 155: The scattering-light effect for these four geometries is analyzed.

Direct back scattering When the main beam is reflected by a mirror, some of the main light field is scattered back by the non-uniform distribution of the mirror surface. The scattered field couples with the cavity resonant mode in the opposite direction in respect to the propagation direction of the main beam, just after being scattered by one mirror. Direct back scattering occurs at each mirror in all geometries except the two-mirror cavity.

The scattered field is written as

$$\psi_{sc}(x, y, z) = \psi_{cav}(x, y - z) \exp[-2ik_0M(x, y)]m(x, y, \alpha) \tag{165}$$

where

$$m(x, y, \alpha) = \exp\left[-2ik_0x \tan \alpha + \frac{ik_0(x^2 + y^2)}{2r_C}\right], \tag{166}$$

where $M(x, y)$ is a surface map of the mirror where the scattering occurs, and $m(x, y, \alpha)$ describes the phase delay due to the mirror angle α in respect to the mirror normal, and the radius of curvature of the mirror r_C is taken into account as the phase delay due to the reflection surface geometry. The target field is the same mode as the main beam but in the opposite direction since the

Substituting Eq. (165) into Eq. (163), we obtain the coupling coefficient as

$$X_1 = \frac{k_0z_R}{\pi(z^2 + z_R^2)} \int_{-\infty}^{\infty} \int_{-\infty}^{\infty} \exp\left[-\frac{k_0z_R(x^2 + y^2)}{z^2 + z_R^2} - ik_0\left\{\frac{x^2 + y^2}{2r_C} + 2M(x, y) + 2x \tan(\alpha)\right\}\right] dx dy. \tag{167}$$

Diagonal-path scattering I In the rectangular cavity, diagonal lines of the rectangular geometry can be scattered light paths as depicted in the left panel of Fig. 156. When the main beam illuminates a mirror, some scattered light occurs by the mirror surface distribution. We assume that the light field is scattered and propagate along the diagonal path as a spherical wave. The spherical field is reflected by a mirror at the diagonal line end, and the field couples into the cavity Gaussian mode again. Although, strictly speaking, this coupling is occurred by the second scattering, we approximate this process is occurred by the reflection with the second mirror. It is because the longer and shorter paths in the rectangular geometry for the 10 km ET filter cavities are 1 m and 5 km, respectively, therefore the diagonal path is almost parallel to the longer path. The field propagating direction after the coupling determined when the second reflection. For example, the

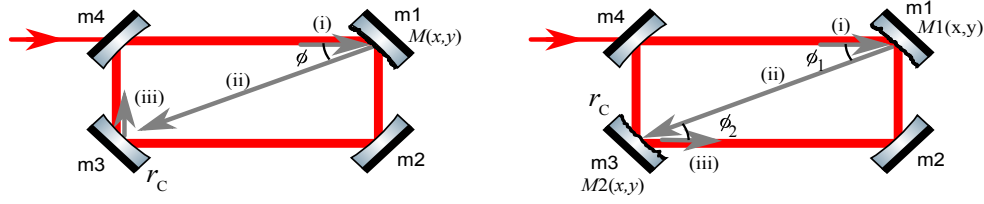


Figure 156: Left panel: scattering process of diagonal-path I. (i) Laser light is scattered when the main beam is reflected by mirror 1. The mirror surface distribution is $M(x, y)$. (ii) The scattered light propagates along the diagonal line of the rectangular as a spherical wave. (iii) the scattered field is approximately reflected by the mirror (m3) and couples into the Gaussian mode of the cavity. Right panel: scattering process of diagonal-path II. Processes (i) and (ii) are the same as diagonal-path I. (iii) the scattered field is scattered again by mirror m3 with its mirror map $M2(x, y)$ and couples into the Gaussian cavity mode.

scattered field propagating the paths shown in the left panel of Fig. 156 couples to the cavity mode in the normal direction. Here we assume that the amplitude of the scattered field is proportional to the bidirectional reflection distribution function (BRDF) which describes the scattering intensity distribution of the mirror. As BRDF of a ET mirror is unknown, we use a typical BRDF in a laser-interferometric gravitational wave detector measured by LIGO pathfinder [cite?]. Note that this is a BRDF of a silica mirror and can be very different from the advanced ET mirrors.

The scattered field is written as

$$\psi_{sc}(x, y, z) = \frac{\eta(\phi)}{R_d} \exp \left[-ik_0 R_d - 2ik_0 M(x, y) + \frac{ik_0(x^2 + y^2)}{2r_C} \right] \quad (168)$$

where R_d is a distance of the diagonal path and r_C is a radius of curvature of a mirror when the scattered field couples into the cavity. $M(x, y)$ is the mirror surface map of the mirror where the scattered light occurs (m1 in Fig. 156). The amplitude $\eta(\phi)$ is assumed using the BRDF: The scattered power that reaches the reflection mirror at the end of the diagonal path is written as

$$P(\phi) \sim P_0 \text{BRDF}(\phi) dS \quad (169)$$

where P_0 is the incident light power, dS is the mirror surface area receiving the scattered light, ϕ is the angle between the main incoming beam to the mirror and the diagonal path, and the BRDF is

$$\text{BRDF}(\phi) = \frac{1000}{(1 + 5.302 \times 10^8 \phi^2)^{1.55}}. \quad (170)$$

Therefore,

$$\eta(\phi) = \sqrt{P(\phi)}. \quad (171)$$

It is noted that the BRDF used here is valid when the incoming beam is perpendicular to the mirror surface, which is different from our situation. The bidirectional reflection distribution might be altered in our case in which the incoming beam and the mirror normal have an angle.

Substituting Eq. (168) into Eq. (163), The coupling coefficient is

$$X_2 = \sqrt{\frac{z_R k_0}{\pi}} \frac{\eta(\phi)}{R_d(z_R + iz_{cav})} \int_{-\infty}^{\infty} \int_{-\infty}^{\infty} \exp \left[-ik_0 \left\{ R_d + \frac{x^2 + y^2}{2r_C} - \frac{x^2 + y^2}{(z_{cav} - iz_R)} + M(x, y) \right\} \right] dx dy. \quad (172)$$

Diagonal-path scattering II In the rectangular cavity, there is another coupling process due to the diagonal path. The stray light scattered by one mirror propagate the diagonal path as a spherical wave as in the process considered in the previous section. In this case, the field couples into the Gaussian cavity mode not by reflected but by scattered again at the second mirror (right panel of Fig. 156).

The light field after the second scattering is written as

$$\psi_{sc}(x, y, z) = \frac{\eta(\phi_1)\eta(\phi_2)}{R_d} \exp\left[-ik_0\left\{R_d + \frac{x^2 + y^2}{2r_C} + M_1(x, y) + M_2(x, y)\right\}\right]. \quad (173)$$

where ϕ_1 is the angle between the main beam and the diagonal path when the first scattering, and ϕ_2 are the angles between the diagonal path and the cavity path when the scattered field couples again into the cavity mode.

Substituting Eq. (173) into Eq. (163), the coupling coefficient is derived as

$$X_3 = \sqrt{\frac{k_0 z_R}{\pi}} \frac{\eta(\phi_1)\eta(\phi_2)}{R_d(z_R + iz_{cav})} \int_{-\infty}^{\infty} \int_{-\infty}^{\infty} \exp\left[-ik_0\left\{R_d + \frac{x^2 + y^2}{2r_C} - \frac{x^2 + y^2}{2(z_{cav} - iz_R)} + M_1(x, y) + M_2(x, y)\right\}\right] dx dy. \quad (174)$$

Gaussian tail effect In the rectangular and bow-tie cavities, the tail of the Gaussian field is partially reflected by a mirror which is not the mirror for the next reflection, as shown in Fig. 157. The partially reflected field may coupled into the cavity. When the mirror (therefore the coupling point) is L m away in x direction, to the main beam, the coupling field is written as

$$\psi_{sc}(x, y, z) = \psi(x + L_s, y, z_{sc}). \quad (175)$$

The coupling coefficient is

$$X_4 = \frac{-k_0 z_R}{\pi(iz_{cav} + z_R)(iz_{sc} - z_R)} \int_{-\infty}^{\infty} \int_{-\infty}^{\infty} \exp\left[-ik_0\left\{\frac{x^2 + y^2}{2(iz_R - z_{cav})} + \frac{(L_s + x)^2 + y^2}{2(iz_R - z_{sc})}\right\}\right] dx dy. \quad (176)$$

Numerical evaluation In order to calculate X_1 - X_4 , we assume that the round trip of a cavity is about 10 km, and a waist position of the laser beam is at the middle point of the round trip for the all geometries, as shown in Fig. 8. The triangular cavity is an isosceles triangle with two 5km arms and with a 1 m base, and the beam waist is at the middle of the short path. The rectangular cavity has the long and short paths of 5 km and 1 m, respectively and the beam waist is at m2 in Fig. 158. The bow-tie cavity have four paths of 2.5 km and the separation between the closer mirrors is assumed as 1 m. For mode-matching, flat or a radius of curvature r_C was assumed for each mirror. And ET fake mirror maps simulated using a sum of Zernike polynomials with maximum 1 nm amplitude were used [97].

• X_1 : Fig. 159 shows X_1 over the mirror angle α for various positions where scattering occurs ($z=1, 1000, 2500,$ and 5000). X_1 is strongly depends on the angle between the mirror normal and the propagation direction of the beam, α . The coupling coefficient becomes rapidly zero when the angle is larger than 10^{-3} degrees. Since the mirror angles of all the ring cavities have much larger α , the direct back-scattering coupled to the cavity mode is negligible. However one have to be careful not to have mirror surface structures which may generates additional scattering light.

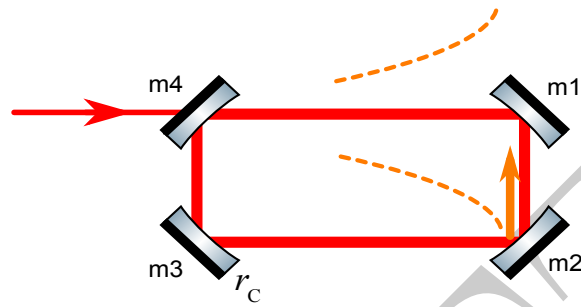


Figure 157: Simplified image of the Gaussian tail effect.

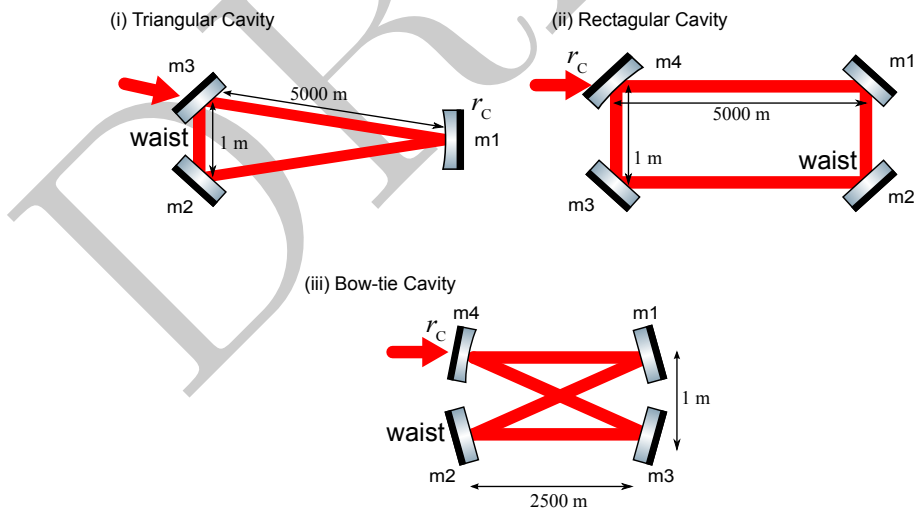


Figure 158: Cavity designs used for the numerical calculation. The cavities have a round trip length of approximated 10 km, and a beam waist at the middle point of the path.

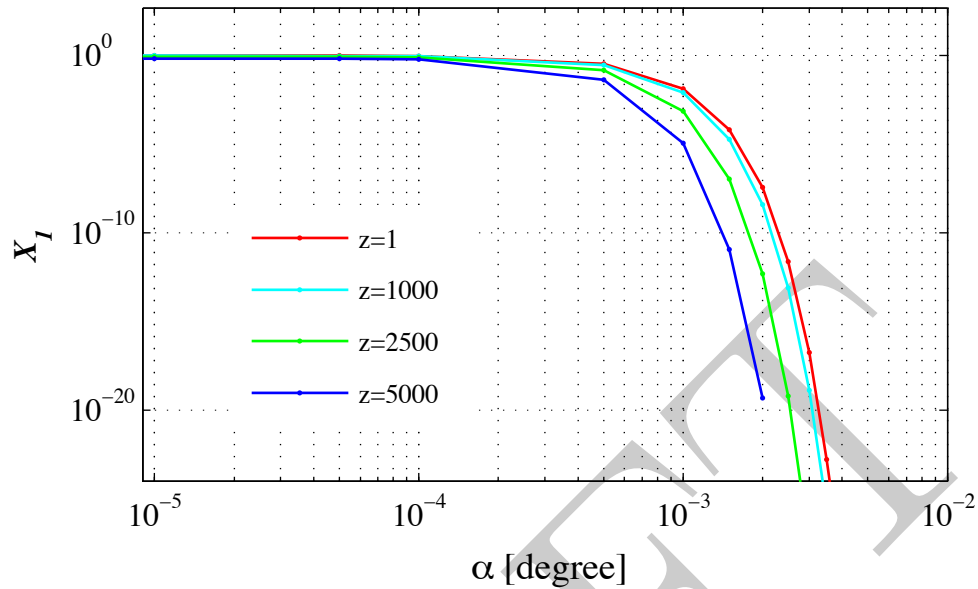


Figure 159: The coupling factor X_1 (direct back scattering) over the mirror angle where the scattering process occurs. The coupling factor rapidly goes to be zero after 10^{-3} degrees.

Type	direct-back scattering	Diagonal 1	Diagonal 2	Gauss. Tail
Two-mirror	N/A	N/A	N/A	N/A
Triangular	0	N/A	N/A	N/A
Rectangular	0	4.5×10^{-7}	1.0×10^{-8}	0
Bow-tie	0	N/A	N/A	0

Table 13: Summary of the scattering process for each geometry. The numbers are in amplitude while the light power is normalized to be unity inside the cavity.

- X_2 : X_2 is numerically evaluated using the ET fake mirror map. There are four diagonal paths in a rectangular cavity since the scattering process occur at each mirror. The total amplitude of the scattered field is 4.5×10^{-7} , while the laser power is normalized to be unity at each mirror.
- X_3 : X_3 is numerically evaluated using the two ET fake mirror maps. Similarly to the X_2 case, there are four diagonal paths in the rectangular cavity since the scattering process occur at each mirror. Using the same geometry of the rectangular cavity and the beam parameters, we obtained the total amplitude of the scattered field 1.0×10^{-8} , while the laser power is normalized to be unity at each mirror.
- X_4 : We found that X_4 is negligible with the beam and cavity parameters we are considering. The separation of the shorter paths in rectangular or bow-tie cavities of 1 m in the numerical evaluation, which turned to be enough. although this length should not be too close.

Table. 13 shows the summary of the numerical evaluation. The two-mirror cavity is the best configuration from the scattered-light point of view, since there is no spurious path in the geometry. For the other three configurations, the direct back scattering and the Gaussian tail effect are found to be negligible with the ET fake mirror maps. One has to be careful to the scattering field propagating along the diagonal paths in the rectangular cavity. Therefore one should block the diagonal paths by putting baffles inside the rectangular to prevent from the scattered light coupling back into the cavity.

5.7.4 Noise couplings

In this Section several noise mechanisms that potentially limit the detected squeezing levels are discussed. First, we discuss the effect of phase noise in the squeezing path. Assuming a self-homodyning readout (DC readout) of the interferometers signal field, the DC part of the interferometer's output field serves as local oscillator. The quadrature of the signal field, that is read out is determined by its relative phase with regard to this local oscillator. In order to reduce the quantum noise of this measurement, the relative phase of the injected squeezed field needs to be chosen such that the squeezed quadrature coincides with the readout quadrature. This required phase relation gets disturbed due to e.g. vibrating optical components in the squeezing path (displacement noise) or residual high frequency phase modulations that probably will be required for control purposes. If the measurement time is greater than the period of the phase jitter period, the homodyne read out is not a pure measurement of a certain quadrature Φ (e.g. the squeezed quadrature) but the integral over some span of $\Phi + \delta\Phi$. In this case, a certain fraction of the noise in the anti-squeezed quadrature is mixed into the measurement that was intended to be a measurement of the squeezed quadrature. It is obvious, that such a *phase diffused squeezed state* results in a degraded squeezing level. Accordingly, an upper limit for the overall tolerable phase noise in the squeezing path needs to be deduced with regard to the targeted quantum noise reduction of 10 dB.

The influence of phase noise on the squeezed field can be nicely illustrated by the accordant Wigner functions. We start from the Wigner function of a squeezed state that has a certain orientation (determined by the quadrature angle φ) in phase-space. It is given by

$$W(X_{1,\varphi}, X_{2,\varphi}, \varphi) = \frac{1}{2\pi\sqrt{V_s V_a}} \exp \left[-\frac{X_{1,\varphi}^2}{2V_s} - \frac{X_{2,\varphi}^2}{2V_a} \right]. \quad (177)$$

Here V_s and V_a denotes the variances in the squeezed and anti-squeezed quadrature, respectively (e.g. for a pure 10dB squeezed state $V_s = 0.1$ and $V_a = 10$ if normalised to the variance of the vacuum state $V_{\text{vac}} = 1$). The orientation in phase-space is accounted for by setting

$$X_{1,\varphi} = X_1 \cos(\varphi) - X_2 \sin(\varphi) \quad (178)$$

$$X_{2,\varphi} = X_1 \sin(\varphi) + X_2 \cos(\varphi). \quad (179)$$

Here, the local oscillator serves as reference for the phase-space with its amplitude (X_1) and phase quadrature (X_2). The corresponding probability distribution in the amplitude quadrature (X_1) can be obtained from the Wigner function by integrating over X_2 . One obtains

$$P_{X_1} = \int_{-\infty}^{\infty} W_d(X_1, X_2) dX_2 \quad (180)$$

$$= \frac{1}{\sqrt{2\pi V_{X_1}(\varphi)}} \exp \left[-\frac{X_1^2}{2V_{X_1}(\varphi)} \right]. \quad (181)$$

with the variance of the amplitude quadrature

$$V_{X_1}(\varphi) = V_s \cos^2(\varphi) + V_a \sin^2(\varphi) \quad (182)$$

$$= \frac{1}{2} [V_s + V_a + (V_s - V_a) \cos(2\varphi)]. \quad (183)$$

Now, to describe a phase diffused squeezed state, the quadrature angle φ needs to be replaced by a probability density for the phase denoted as $\Phi(\varphi)$. Then, the Wigner function is given by

$$W_d(X_1, X_2) = \int \Phi(\varphi) W_d(X_1, X_2, \varphi) d\varphi. \quad (184)$$

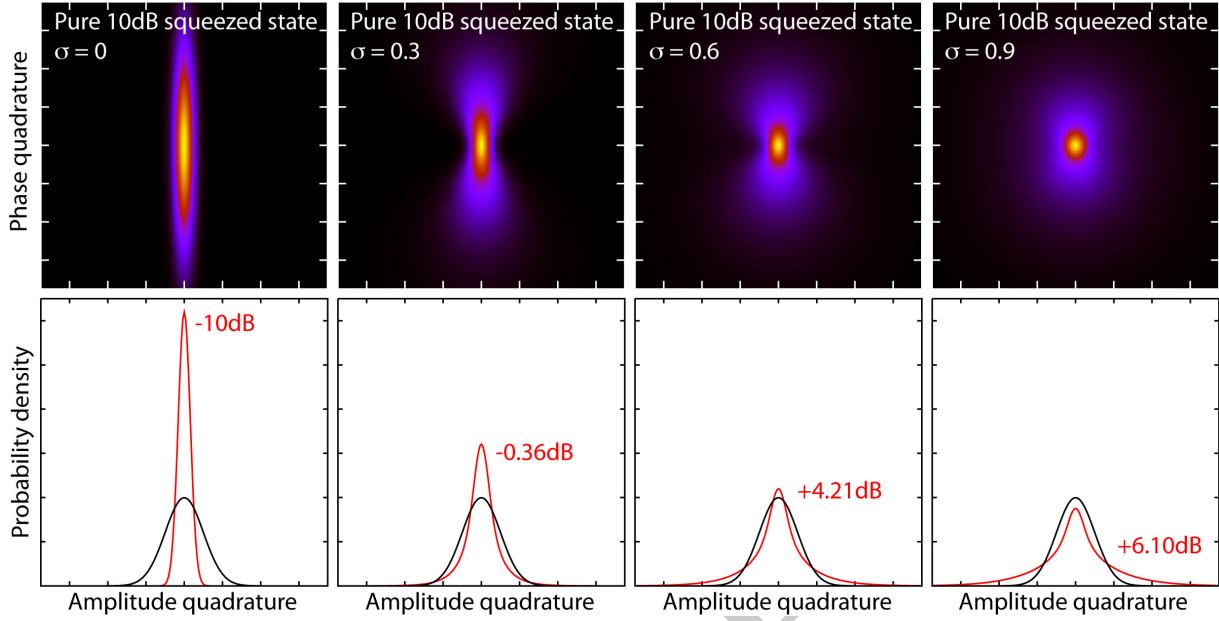


Figure 160: Illustration of the influence of a Gaussian distributed phase noise on the squeezed state. **Top:** Wigner functions for phase noise with a standard deviation σ of 0, 0.3, 0.6, 0.9. The initial, pure squeezed state was assumed with 10 dB. **Bottom:** The probability distribution of the phase diffused squeezed states and the corresponding squeezing levels (red curves and red labels, respectively) in the amplitude quadrature (X_1). For comparison, the distribution of a vacuum state is shown (grey curves).

Again, the corresponding probability distribution in the amplitude quadrature (X_1) can be obtained from the Wigner function by integrating over X_2

$$P_{X_1,d} = \int_{-\infty}^{\infty} W_d(X_1, X_2) dX_2. \quad (185)$$

Accordingly, the variance of a phase diffused squeezed state is given by

$$V_{X_1,d} = \int_{-\infty}^{\infty} \Phi(\varphi) V_{X_1} d\varphi \Leftrightarrow \int_{-\infty}^{\infty} P_{X_1,d} X_1^2 dX_1. \quad (186)$$

In Fig. 160 four Wigner functions (top) and the corresponding probability distribution in the X_1 -quadrature (bottom) are shown. We assumed and Gaussian distributed phase noise, i.e

$$\Phi(\varphi) = \frac{1}{\sqrt{2\pi\sigma^2}} \exp\left(-\frac{\varphi^2}{2\sigma^2}\right). \quad (187)$$

We have considered phase noise with a standard deviation σ of 0 (no phase noise), 0.3, 0.6 and 0.9 (from left to right in Fig. 160). The initial squeezed state (left figures) was assumed with $V_s = 0.1$ and $V_a = 10$, i.e. as a pure 10 dB squeezed state. The degradation of the squeezing level due to phase noise becomes obvious from the comparison with the probability distribution of a vacuum state (grey traces in the bottom graphs). The probability distribution are labelled with the corresponding squeezing level. For strong phase noise the initial squeezing is destroyed and the noise in the amplitude quadrature is even enhanced when compared to the vacuum noise (shot noise).

The illustration in Fig. 160 implies, that the larger the anti-squeezing level, the larger the effect of phase noise. In fact, in order to achieve the targeted quantum noise reduction of 10 dB, a squeezed light source needs to

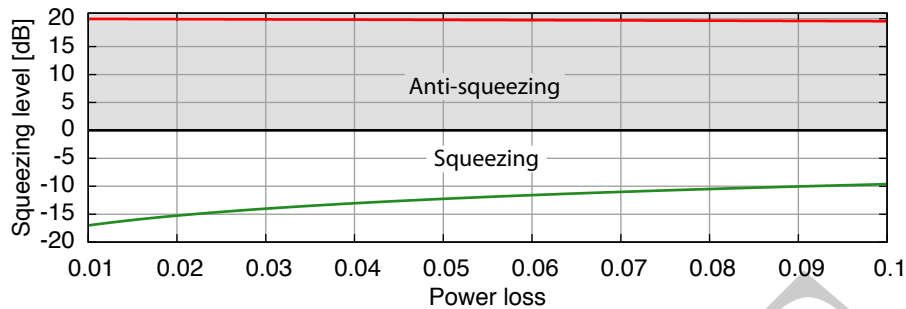


Figure 161: The degradation of the squeezing and anti-squeezing levels due to optical loss for an initially pure (no loss) 20 dB squeezed state.

be utilised that generates considerably more than 10 dB (anti-)squeezing to compensate for possible loss. If an overall optical loss of up to 10% in the squeezing path (including 1% loss in the squeezed light source itself) is assumed, an initially pure 20 dB squeezed state needs to be generated. The degradation of the squeezing (and anti-squeezing) level with optical loss is shown in Fig. 161. Whereas the squeezing level is strongly affected by optical loss, the anti-squeezing level is not considerably reduced. Considering an overall optical loss of 10% the squeezing level is reduced from 20 dB to about 9.6 dB, but the anti-squeezing level is still about 19.5 dB. In Fig. 162 the effect of phase noise on a initially 20 dB squeezed state is illustrated at which optical loss of 1%, 3%, 5% and 10% was considered. Here the phase noise was assumed with a standard deviation of $\sigma = 0.3$. Again, the top graphs show the Wigner functions and the bottom graphs the probability distribution in the amplitude quadrature. Here, in each case three traces are plotted. The red trace is the distribution of the phase diffused squeezed state and the black one that of a vacuum state. The grey curves correspond to the distribution without phase noise, i.e. the degradation of the squeezing level only due to the considered optical loss can be deduced. Again, it can be seen that the high phase noise destroys the squeezing. In each case, the resulting noise level is considerably enhanced when compared to the shot noise level. Please note the following: although the squeezing levels in the undisturbed case are ≥ 10 dB, the high anti-squeezing level of almost 20 dB leads to higher noise levels when compared to the pure 10 dB squeezed state (refer to Fig. 160). In presence of phase noise the achievable squeezing level can be optimized by reducing the anti-squeezing (and thus the squeezing) generated by the squeezed light source. On the other hand, that means that in presence of considerable phase noise a compensation of optical loss in the squeezing path is not possible by enhancing the squeezing (and thus the anti-squeezing) generated in the squeezed light source.

In the foregone investigation for illustration purposes comparatively high values for the phase noise was considered. Such high values are not expected to be present in a suitable experimental environment. However, the upper limit for the overall phase noise in the squeezing path depends on the squeezed state, that is generated by the squeezed light source. Table 14 lists the allowed phase noise (i.e its standard deviation) for several conditioned squeezed states. The states were constituted for several values of the optical power loss l^2 such that the squeezing level without phase noise is 10 dB. The required squeezing that needs to be generated inside the squeezed light source can be calculated according to

$$V_s = 0.1 - l^2 \quad \text{and} \quad V_a = \frac{1}{V_s}. \quad (188)$$

We relates the upper limit σ_{\max} for the phase noise to a squeezing level that is reduced to 9 dB due to the phase noise. As the phase noise is assumed to be Gaussian distributed with zero mean, Eq. (186) can be solved giving

$$V_{X_{1,d}} = \frac{1}{2} [V_s + V_a + (V_s - V_a) \exp(-2\sigma^2)]. \quad (189)$$

Solving Eq. (189) for σ yields

$$\sigma = \sqrt{-\frac{1}{2} \log \left[\frac{2V_{X_{1,d}} - V_s - V_a}{V_s - V_a} \right]}. \quad (190)$$

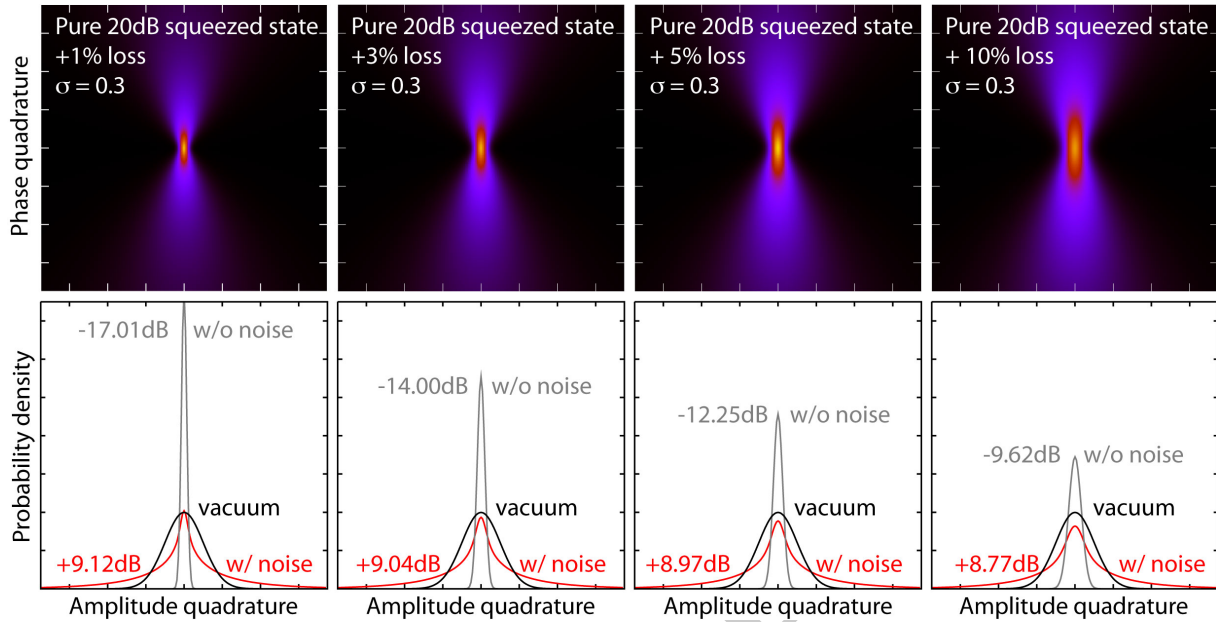


Figure 162: Degradation of a pure 20 dB squeezed state due to optical loss and phase noise.

From this equation the tolerable phase noise characterised by σ_{max} can be calculated for the targeted variance $V_{X_{1,d}} = 0.1$ and squeezing level of 10 dB, respectively.

optical loss [%]	initial squeezing [dB]	squeezing [dB]	anti-squeezing [dB]	σ_{max}
1	-10.41	-10	10.37	0.049
3	-11.41	-10	11.29	0.044
5	-12.79	-10	12.58	0.038
9	-19.59	-10	19.19	0.018
10	$-\infty$	-10	∞	0
20	$-\infty$	-6.99	∞	0

Table 14: The table lists the squeezing and anti-squeezing levels and the tolerable phase noise for several values of optical loss.

From the tolerable σ_{max} we will deduce in following investigations

- the allowed displacement noise in the filter cavities
- the requirements for the filter cavities' length stabilization
- the requirements of frequency noise of the squeezed light source related to main interferometer beam

5.7.5 Length control of the filter cavities

We will analyse

- the realisation of a locking scheme without introducing too much optical loss (due to pick-off mirrors needed for detection ports).
- the potential of using the orthogonal polarisation for error signal generation.

- the restrictions to RF sidebands. They need to be in the same mode as the squeezing, therefore generated in the squeezer by means of the coherent control beam.
- A ring -vs- a linear filter cavity design. If linear filter cavities are used additional Faraday rotators are required.

5.8 Optical layout

Author(s): S. Hild, A. Thuering, A. Freise

5.8.1 A xylophone design for ET

Spanning the detection band over four orders of magnitude in frequency, as is ~~ask~~ for third generation GW observatories such as ET, is technically extremely challenging: Different noise types dominate the various frequency bands and often show opposite response for different tuning of the same design parameter.

In the following we give some examples of fundamental issues of a broadband third generation interferometer that could be resolved by using a set of xylophone detectors:

- **High Power vs Cryogenic Temperature:** Using a single broadband ET observatory as described in [268] ~~features~~ the challenge of the simultaneous use of high optical power (a few megawatts) to ~~achieve~~ the required high frequency sensitivity and ~~is~~ masses at cryogenic temperatures in order to provide the required suppression of thermal noise. Even though tiny, the residual absorption of the dielectric mirror coatings deposits heat in the mirrors which is difficult to extract, without spoiling the performance of the seismic isolation systems. A possible solution for this problem would be to build a xylophone observatory consisting of a high frequency detector featuring high power and high temperature and a low frequency detector featuring low power and cryogenic temperatures.
- **Shot Noise vs Radiation Pressure Noise:** As already briefly described ~~in~~ above it ~~is~~ will be hard to obtain the desired bandwidth with a single detector due to inverse scaling of photon radiation pressure noise and photon shot noise with the circulating power. Therefore, again it might be useful to split ET into a low-power low-frequency and a high-power high-frequency companion.
- **Mixing Interferometer Topologies:** Xylophone configurations will also allow ~~to mix~~ alternative interferometer topologies, such as Sagnac interferometer [158] and optical levers [296], with the standard Michelson interferometer. For example one could imagine to accompany a standard high-frequency Michelson interferometer with a low-frequency optical lever detector.

The xylophone concept was first suggested for Advanced LIGO, proposing to complement the standard broadband interferometers with an interferometer optimized for lower frequency, thus enhancing the detection of high-mass binary systems [167, 487].

One may think that a xylophone might significantly increase the required hardware and its cost by the need to build more than one broadband instrument. However, such an argument does not take the technical simplifications that it would allow, the better reliability of simpler instruments, and the more extensive scientific reach allowable into account. For example splitting a third generation observatory in to a low-power, low-frequency and a high-power high-frequency interferometer, has not only the potential to resolve the above mentioned conflict of PSN and PRPN, but also allows to avoid the combination of high optical power and cryogenic test masses. To reduce thermal noise to an acceptable level in the low frequency band, it is expected that cryogenic suspensions and test masses are required. Even though tiny, the residual absorption of the dielectric mirror coatings deposits a significant amount of heat in the mirrors. Since this heat is difficult to extract, without spoiling the performance of the seismic isolation systems, it imposes a limit on the maximum circulating power of a cryogenic interferometer.

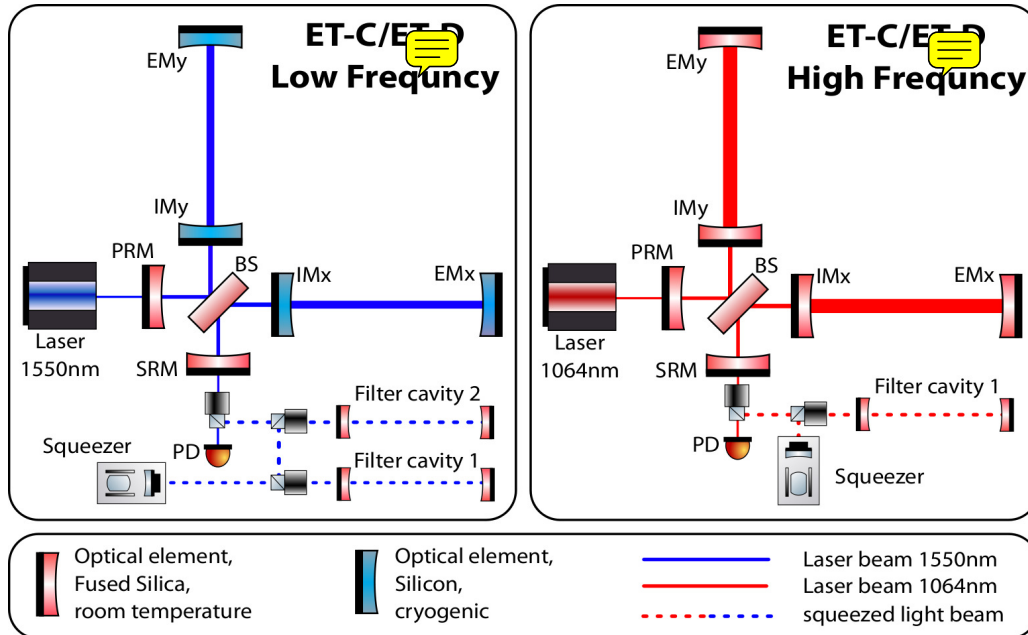


Figure 163: Simplified sketch of the ET low and high frequency core interferometers of a single ET-detector.

Parameter	ET-D-HF	ET-D-LF
Arm length	10 km	10 km
Input power (after IMC)	500 W	3 W
Arm power	3 MW	18 kW
Temperature	290 K	10 K
Mirror material	Fused Silica	Silicon
Mirror diameter / thickness	62 cm / 30 cm	min 45 cm/ TBD
Mirror masses	200 kg	211 kg
Laser wavelength	1064 nm	1550 nm
SR-phase	tuned (0.0)	detuned (0.6)
SR transmittance	10 %	20 %
Quantum noise suppression	freq. dep. squeez.	freq. dep. squeez.
Filter cavities	1 × 10 km	2 × 10 km
Squeezing level	10 dB (effective)	10 dB (effective)
Beam shape	LG ₃₃	TEM ₀₀
Beam radius	7.25 cm	9 cm
Scatter loss per surface	37.5 ppm	37.5 ppm
Seismic isolation	SA, 8 m tall	mod SA, 17 m tall
Seismic (for $f > 1$ Hz)	$5 \cdot 10^{-10} \text{ m}/f^2$	$5 \cdot 10^{-10} \text{ m}/f^2$
Gravity gradient subtraction	none	none

Table 15: Summary of the most important parameters of the ET-D high and low frequency interferometers. SA = super attenuator, freq. dep. squeez. = squeezing with frequency dependent angle.

The baseline for ET is a 2-band xylophone detector configuration, composed of a low-frequency (ET-LF) and a high-frequency (ET-HF) detector. Both interferometers are Michelson interferometers featuring 10 km arm-length and an opening angle of 90 degree. Due to their similar geometry both detectors will share a single facility. Table 15 gives a brief overview of the main parameters of the analysed low-frequency (ET-LF) and high-frequency (ET-HF) detector. Figure 163 shows sketches of the corresponding core interferometers and the filter cavities. The full layout of the two core interferometers of a single ET detector is depicted in Figure 164.

5.8.2 Arm cavity design

The size and shape of the laser beam inside the interferometer is defined by the surface shape of the cavity mirrors; the beam sizes at the IM and EM as well as the position of the cavity waist are determined by only two parameters, the radii of curvature (ROC) of IM and EM. Since inside the two Fabry-Perot cavities of the Michelson interferometer the GW interacts with the laser light, creating signal sidebands, the two arm cavities can be seen as the heart of the ET interferometers. The characteristics of the arm cavities have not only a high impact on the detector sensitivity and bandwidth, but also on the overall detector performance.

The choice of the beam size on the arm cavity mirrors is a trade-off process taking the following considerations into account:

- For a given cavity length there is a minimal achievable beam size, which is determined by the divergence of the beam.
- Above this minimal beam size, any further increase in beam size leads to ~~and~~ additional reduction of the various thermal noise contributions.
- Finally the upper limit for the manageable beam size is given firstly by the maximum available mirror substrate size and secondly by the approaching ~~the~~ cavity instability.

Beam waist of the arm cavity beam eigenmode

In the case of a two-mirror cavity the size of the beam can be computed conveniently from the stability parameters g_1, g_2 given as:

$$g_{1,2} = 1 - \frac{L}{R_{C1,2}} \quad (191)$$

with L the length of the cavity and $R_{C1,2}$ the radius of curvature of the input and end mirror respectively.

The waist size w_0 of the cavity eigenmode can then be computed as :

$$w_0^2 = \frac{L\lambda}{\pi} \sqrt{\frac{g_1 g_2 (1 - g_1 g_2)}{(g_1 + g_2 - 2g_1 g_2)^2}} \quad (192)$$

In many cases symmetric or near symmetric cavity layout will be used (or can be used to estimate design options). In that case we set $g = g_1 = g_2$ which leads to a much simpler equation:

$$w_0^2 = \frac{L\lambda}{2\pi} \sqrt{\frac{1+g}{1-g}} = \frac{L\lambda}{2\pi} \sqrt{\frac{2R_C}{L} - 1} \quad (193)$$

Beam size on the arm cavity mirrors

Typically we are interested in the size of the beam on the mirror, rather than the waist size directly. The beam size can be computed similarly as the waists; for the input mirror we get:

$$w_1^2 = \frac{L\lambda}{\pi} \sqrt{\frac{g_2}{g_1(1 - g_1 g_2)}} \quad (194)$$

And in the case of a symmetric cavity we obtain:

$$w^2 = \frac{L\lambda}{\pi} \sqrt{\frac{1}{1-g^2}} = \frac{\lambda}{\pi} \sqrt{\frac{RL}{2 - \frac{L}{R}}} \quad (195)$$

Arm cavity mirror size

A common method to define the mirror size is to demand the optical power loss due to clipping (light being lost because it ‘falls over the edge of the mirror’) to be less than 1 ppm. The computation of the scaling factors is described in [157] and results in:

mode	LG00	LG33
mirror radius to beam radius	2.63	4.31

Minimal mirror sizes for ET

Using the currently discussed options for ET we can compute minimal mirror sizes for various options, by using $L = R_C$ resulting in $w_{\min} = \sqrt{\frac{L\lambda}{\pi}}$.

setup	min beam radius [cm]	min mirror diameter [cm]
LG33, 1064nm	5.8	50.2
LG00, 1550nm	7.0	37.0

Realistic mirror sizes for ET

Using the minimal beam sizes is obviously not optimal in terms of thermal noise. Therefore we intend to push the beam sizes for ET towards the maximum feasible size, which corresponds to about 60 cm substrate diameter for fused silica mirrors and 50 cm for the silica mirrors. Assuming 9.3 km long arm cavities, we can derive the following arm cavity characteristics.

IFO	λ	beam shape	mirror diameter	R_C	w_0	z_0	w	z_R
ET-HF	1064 nm	LG ₃₃	62 cm	5147.7 m	2.27 cm	4650 m	7.25 cm	1521.3 m
ET-LF	1550 nm	TEM ₀₀	45 cm	5489 m	3.11 cm	4650 m	8.0 cm	1964 m

5.8.3 Central interferometer design

The central interferometers consist of the two recycling cavities and the central Michelson interferometer formed by the beam splitter and the arm cavity input mirrors. The design of the central interferometer is mainly determined by two constraints. First of all it should allow for the implementation of non-degenerate recycling cavities. Second, the central interferometer has to serve as mode matching telescope for the arm cavities.

The non-degenerate recycling cavity design used by the advanced detectors (see Figure 175) can probably not be directly adapted for ET, because no beam splitter substrates of the required dimensions would be available. For example the high frequency interferometer featuring an opening angle of 60 degree would require a beam splitter with a diameter of 115 cm.

Therefore we plan to investigate design options, making use of input mirror substrates including a focussing lens with a focal length of 0.5 to 1 km and shifting the input mirrors away from the beam splitter. Figure 164 illustrates how such a configuration would like. Please note that the arm cavity mirrors are the only full sized optical elements and that beam splitter and recycling mirrors can be significantly smaller. In addition in this scenario no additional folding mirrors are necessary in the recycling cavities.

Layout option for LG00, 1550nm

The optical parameters of a possible solution based on a arm cavity length of $L = 9.3$ km and a LG00 mode at 1550 nm are provided below:

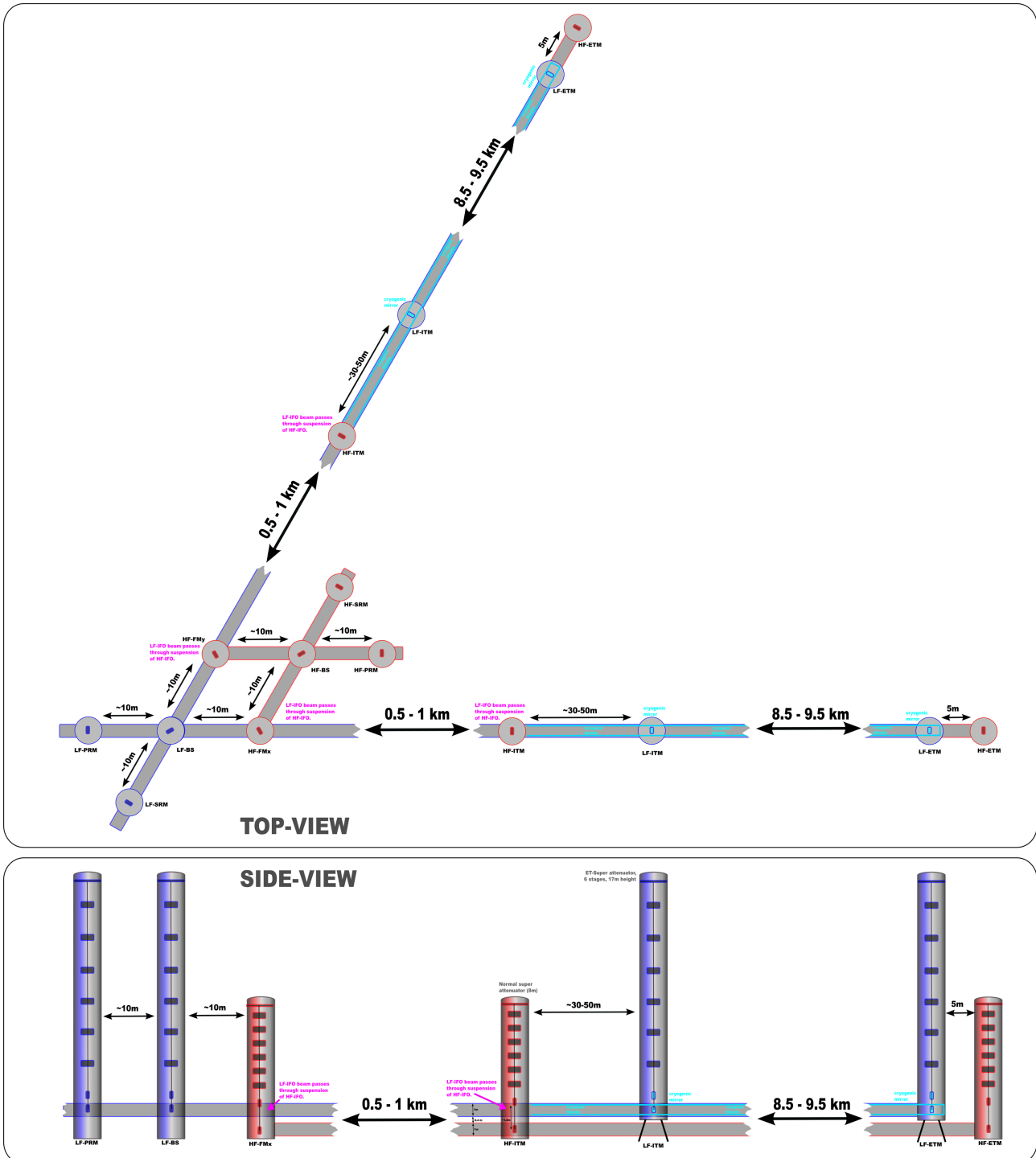


Figure 164: Simplified drawing of the low and high frequency core interferometers of a single ET-detector. Injection and detection optics as well as filter cavities have been omitted for clarity. Please note that the complete ET observatory consists of three such detectors.

- focussing element in or near the ITM with a focal length of $f = 685$ m
- distance ITM-BS: 700 m
- distance BS-MPR: 10 m
- beam size on BS: 0.95 cm
- beam size on MPR: 0.86 cm
- Rayleigh range in central interferometer: 47.0 m

The recycling cavity formed by MPR and ITM has a length of 710 m and a FSR of 211 kHz. The round-trip Gouy phase is given by ≈ 9.7 deg which corresponds to a mode separation frequency of 11 kHz.

Layout option for LG33, 1064nm

Using the same distances and focussing elements for the interferometer with a LG33, 1064 nm beam, we also obtain reasonable numbers:

- beam size on BS: 0.89 cm
- beam size on MPR: 0.81 cm
- Rayleigh range in central interferometer: 40 m
- Gouy phase: 7.6 deg
- mode separation frequency: 9 kHz

These layout options are not yet optimised in any way but they show that a separation between beam splitter and input optics in the order of 700 m represents a useful baseline. The numbers for the beam sizes at the beam splitter and recycling mirrors in both cases need to be checked against a detailed thermal noise computation.

Furthermore, the design needs to be evaluated for losses originating from astigmatism inside the recycling cavities as well as for scattered noise issues.

5.9 Main interferometer optical components

Author(s): K. Kokeyama, A. Freise, etc.

As the optical components for ET HF/LF interferometers, silicon, sapphire, and fused silica substrates have been proposed. The substrate materials show different properties and performances depending on the environment especially on the temperature, the material should be properly investigated. The most important elements to be considered are the thermal properties and the surface qualities attained by the material. The thermal and mechanical properties of silicon, sapphire, fused silica will be summarized in Appendix 5.16.

5.9.1 Bulk material selection

Authors: J. Franc, K. Kokeyama, R. Nawrodt

Different materials have been proposed in order to reduce thermal noise of the optics of future gravitational wave detectors. Three main candidate materials are the most promising ones to construct a 3rd generation detector: Fused Silica, Sapphire and Silicon.

Fused Silica is the favorite substrate material for an interferometer or components of an interferometer that operates at room temperature. It is the substrate material of the advanced detectors and will be used as test masses in Advanced LIGO and Advanced Virgo. Due to the extensive use of fused silica for first and second generations of gravitational wave detectors, this material has been extensively characterised at room

temperature. For example, fused silica exhibits very low optical absorption (as low as 1 ppm/cm at 1064 nm and below) with high homogeneity and low birefringence. Driven by the research effort for the Advanced detectors a state of the art polishing and coating technique exists that provide excellent specifications. Micro-roughnesses of better than 0.05 nm RMS and flatnesses of better 8 nm RMS on \varnothing 150 mm have been achieved. Moreover, Fused Silica is available in large pieces with an extremely high purity. Additionally, there exist techniques to fabricate quasi-monolithic suspensions based on pulled fused silica fibres and silicate bonding. These techniques have demonstrated their reliability for years in the GEO600 detector [412?]. This convincing result triggered the implementation of this technique in Advanced LIGO [173, 257, 449] as well as Advanced Virgo [336, 526]. Fused Silica has a very low mechanical loss at room temperature exceeding 4×10^{-10} at 100 Hz [406]. The coefficient of thermal expansion is extraordinary low at room temperature providing a small thermo-elastic noise of the bulk material. However, the mechanical loss increases as the temperature is decreased (see e.g. [36, 476]) reaching values as high as 10^{-3} at 10 K. This would result in a high substrate Brownian noise and makes Fused Silica not suitable for optics operated at low temperatures. Additionally, the thermal conductivity of Fused Silica decreases to 0.4 W/mK at 10 K [215] which is more than 1000 times smaller than for typical crystalline materials.

The second candidate material is Sapphire. This material ~~are~~ is under consideration as a test mass material for LCGT (Large-scale Cryogenic Gravitational-wave Telescope) in Japan [517]. Hence, Sapphire mirrors have been investigated regarding their performance at cryogenic temperatures. Sapphire has a small coefficient of thermal expansion. Below 20 K it can be approximated by $\alpha = 7.5 \times 10^{-13} T^3 [K^{-1}]$ [509]. This leads to a very small thermo-elastic noise at low temperature regime. The mechanical loss of Sapphire has been determined from Q-factor measurements. At 4.2 K losses of 4×10^{-9} and at 20 K of 10^{-8} have been observed [528]. The measured sample was a CSI (Crystal System) Hemlite grade. Additional excellent properties like the high thermal conductivity at low temperatures make Sapphire a good candidate as a bulk material for cryogenic optics. The optical absorption at 1064 nm has been measured by the LCGT group to be about 90 at 5 K [517]. They report that the absorption is temperature dependent reaching 168 ± 24 ppm/cm at room temperature. The value of the absorption is an important property influencing effects like thermal lensing and cooling the mirror. In both cases - at room temperature and cryogenics - the sapphire substrate has about ten to hundred times higher absorption than that of typical Fused Silica. This may cause ~~the~~ thermal lensing effects in a cryogenic interferometer based on Sapphire because the strain due to the thermal lens effect is proportional to the absorption, thermal coefficient of refraction, and input power. However, this does not completely deny the sapphire option, as there are investigations to lower the sapphire absorption by annealing [27]. As artificial sapphire crystals are broadly used in industries (e.g. as laser rods, heat sinks, etc.) there are many Sapphire manufacturers available. The biggest currently available crystal is \varnothing 330 \times 200 mm, 65 kg manufactured by an American company Crystal System (CSI) [165]. This size is not enough for a potential use in the ET LF interferometer. Here, a mirror with a minimum mass of 211 kg is proposed due to the suppression of the radiation pressure noise. This corresponds to a mirror of about \varnothing 620 \times 180 mm which is far away from a current availability. Additionally, the quality of such a large crystal is supposed to be not enough yet. When the c-axis of the crystal and the beam axis are different, optical losses occurs. Therefore the cylinder shape of the mirror must be produced precisely along the c-axis. Also, the deviation between the beam axis and the c-axis increases the birefringence. The currently measured birefringence of sapphire with 250 mm diameter indicated that the birefringence level exceeds the LCGT requirement of the fringe contrast by three times [514]. As another current technical issue, there is no known way to bond sapphire wires onto the sapphire substrate with sufficient strength which would be important for the fabrication of a low thermal noise quasi-monolithic suspension [185]. To suspend the mirror and to extract the heat from the substrate, the bonding should be done with the enough strength while keeping the thermal conductivity. Despite all the issues, it is still anticipated to have large crystals using the high-quality smaller crystals as a seed crystal and growing to a bigger crystal with keeping the quality [165], and sapphire mirrors will be employed by the LCGT interferometer within several years.

The third candidate material that has been proposed as a future detector material is silicon [424, 454]. Silicon has excellent mechanical and thermal properties and is available in high quality due to the large market of the semiconductor industry. The coefficient of thermal expansion is zero at two special temperatures around 18 and 125 K [495]. At these temperatures the contribution of thermo-elastic noise will therefore vanish. The mechanical loss of silicon has been studied by Q-factor measurements. It was experimentally shown that Silicon

bulk samples can reach mechanical losses as low as 5×10^{-10} at 2 K, 1×10^{-9} at 10 K, 4×10^{-9} at 20 K and 5×10^{-9} at 30 K [351]. Intensive studies are in progress to link the mechanical loss of the bulk samples with the purity, surface preparation or the crystal orientation of the sample. Due to the huge demand of high purity silicon wafers for the semiconductor industry silicon bulk samples are available in relative large pieces. The available sample diameter is dependent on the fabrication process. The two main growing processes for single crystal silicon used in semiconductor industry are the Czochralski (CZ) and the Float Zone (FZ) method. CZ grown silicon is grown from a silicon melt in a silica crucible. It results in relative large samples with a reasonable purity. The most dominant impurities in undoped CZ grown silicon are carbon (typically 10^{18} cm^{-3}) and oxygen (typically up to 10^{19} cm^{-3}). In contrast, FZ silicon contains these impurities typically with much smaller concentrations (up to 10^3 times smaller). Single or poly-crystalline silicon is remelt by means of inductive heating in vacuum or under an inert atmosphere during the FZ process. Impurities dissolve better in the melt than in the solid part. The re-crystallised material has therefore a higher purity than the initial one. By slowly sweeping the melt from one end to the other it is possible to purify in steps. The mechanism of inductive heating sets limits to the currently available setups and leads to smaller currently available samples⁸. Well established polishing methods exist for silicon due to the wafer fabrication. Micro roughnesses and flatnesses needed for optical applications can be achieved. Additionally, silicon provides the possibility of jointing pieces by means of bonding techniques (see also section 4.6). Two possible techniques under discussion are anodic bonding and the well establish hydroxide catalysis bonding [185, 544] currently in use in 1st and 2nd generation detectors. Using silicon as a test mass material demands a change in operational wavelength. Silicon is not transparent at 1064 nm (optical absorption: approximately 10^{-1} at 1064 nm [243]). Silicon has a smaller optical absorption at longer wavelengths. Erbium-fibre lasers provide a reliable light source in the IR spectrum. At 1550 nm silicon is transparent and can be used as an standard optical material in reflection and transmission applications. Optical absorption measurements based on the creation of electron-hole-pairs suggests a minimum absorption of 3.2×10^{-2} at 1450 nm at room temperature [293]. However, a detailed analysis of absorption processes and the total optical absorption of silicon at 1550 nm and low temperatures does not exist so far. A similar lack of parameters exists for other optical properties like the refraction index n or the thermo-refractive coefficient dn/dT [166, 221]. Currently, several institutions worldwide investigate these optical properties. Several institutions involved in this design study play a key role in this research.

A detailed description of the mechanical and thermal properties of Fused Silica, Sapphire and Silicon can be found in appendix 5.16.2 and appendix 5.16.3. Selected literature values at 10, 20, 30 and 300 K have been summarized in table 16 and 17. These values have been used for all thermal noise estimates presented within this document.

5.9.2 Coating material selection

J. Franc

Fabrication of 3rd generation of GWD has specific constraints on noise level. Several studies have already demonstrated that coating is the most important noise source in the frequency range of interest. To avoid that coating materials generate a noise level larger than the expected sensitivity, very high quality coating are needed. First, the absorption have to be less than 5 ppm and the loss angle of the material have to be as low as possible. To produce coating with such quality, an IBS coater is needed. Driven by the research performed for 1st and 2nd generation of GWD, a state of the art deposition technique exists that provide high performances coatings [?]. The concept of high reflective mirrors fabrication is based on the quarter-wavelength layer system composed from two materials, one with high refractive index and one with a low refractive index. At first, the work considered SiO_2 as the low refractive index material ($n=1.45$) and Ta_2O_5 as the high refractive index material ($n=2.03$). These two material were the oxide layers having the best optical and mechanical properties. In the past, this multilayer system has offered the best mirror quality for VIRGO interferometer but was improved in the future for the Advanced detector. The measurements made on the $\text{Ta}_2\text{O}_5/\text{SiO}_2$ coatings have shown that the lossier material is the Ta_2O_5 . The improvement has been focused on this latter. Several doped material were

⁸There is still no technical limit reached for the float zone process of silicon. The maximum diameter currently available is set by the demands of the semiconductor market.

Parameter	T (K)	Fused Silica		Sapphire		Silicon	
		Value	Ref.	Value	Ref.	Value	Ref.
heat capacity (J/kg K)	10 K	6.3	[521]	0.085	[559]	0.276	[280]
	20 K	25.2	[521]	0.72	[559]	3.41	[280]
	30 K	54.6	[521]	2.6	[559]	18.55	[280]
	300 K	738	[521]	781	[559]	713	[280]
thermal conductivity (W/m K)	10 K	0.098	[525]	2900	[525]	2110	[524]
	20 K	0.13	[525]	15700	[525]	4940	[524]
	30 K	0.18	[525]	20700	[525]	4810	[524]
	300 K	1.5	[525]	46	[525]	148	[524]
thermal expansion coefficient (1/K)	10 K	-2.2×10^{-7}	[523]	1.0×10^{-9}	[559]	8.8×10^{-10}	[280]
	20 K	-5.8×10^{-7}	[523]	4.0×10^{-9}	[559]	-2.5×10^{-9}	[280]
	30 K	-8.0×10^{-7}	[523]	1.6×10^{-8}	[559]	-5.3×10^{-8}	[280]
	300 K	5.0×10^{-10}	[523]	5.6×10^{-6}	[559]	2.7×10^{-6}	[280]
mechanical loss	10 K	7.9×10^{-4}	[476]	5×10^{-9}	[528]	1×10^{-9}	[351]
	20 K	1.0×10^{-3}	[476]	5.6×10^{-9}	[528]	4×10^{-9}	[380]
	30 K	1.0×10^{-3}	[476]	1.4×10^{-8}	[528]	5×10^{-9}	[351]
	300 K	4×10^{-10}	[406]	3.8×10^{-9}	[453]	1×10^{-8}	[380]
dn/dT (1/K)	10 K	–	–	$< 9 \times 10^{-8}$	[518]	$< 1 \times 10^{-6}$	–
	20 K	–	–	$< 9 \times 10^{-8}$	[518]	1×10^{-6}	–
	30 K	1×10^{-6}	[330]	$< 9 \times 10^{-8}$	[518]	3.3×10^{-6}	[221]
	300 K	8×10^{-6}	[166]	1.3×10^{-5}	[342]	1.9×10^{-4}	[221]

Table 16: Temperature dependent thermal parameters for fused silica, sapphire and silicon bulk material used for thermal noise estimates at selected temperatures. dn/dT is given at 1064 nm for Fused Silica and Sapphire and at 1550 nm for Silicon.

Parameter	Fused Silica		Sapphire		Silicon	
	Value	Ref.	Value	Ref.	Value	Ref.
density ρ (kg/m ³)	2202	[166]	3980	[166]	2330	[166]
Youngs modulus Y (GPa)	72	[166]	400	[166]	188	[166]
Poisson ratio ν	0.17	[166]	0.24	[495]	0.22	[166]
refractive index	1.45	[166]	1.75	[166]	3.453	[166]

Table 17: Parameters of bulk materials that are assumed to be temperature independent for the thermal noise calculations. The refractive index of Fused Silica and Sapphire is given at 1064 nm whereas this parameter is listed at 1550 nm for Silicon.

tested to improve the mechanical losses of Ta₂O₅. By doping Ta₂O₅ with Ti and with an optimization of the deposition process, it is possible to decrease the losses of high refractive index material from 3.8×10^{-4} [166] to 2×10^{-4} [166]. To date, other materials were considered for doping the Ta₂O₅ layers [?]. New materials should be also considered to replace the Ta₂O₅ layers with another high refractive index material. In this context, a table with the parameters values needed for thermal noise calculation for different coating materials is presented [215]:

I. Martin

Extensive studies of the temperature dependence of the mechanical loss of tantala (Ta₂O₅) have been undertaken and the effects of post-deposition heat-treatment and of doping with titania (TiO₂) have been investigated [166, 166, 166]. In general the loss increases at low temperature, with three loss peaks observed to occur at different heat-treatment temperatures. Tantala heat-treated at 300°C and 400°C exhibited a loss peak at approximately 35 K. A larger and narrower loss peak was observed at 20 K in tantala coatings heat-treated at 600°C. There is some evidence that the 35 K peak may also be present in tantala heat-treated at 600°C, underlying the peak at 20 K. It is known that ion-beam sputtered tantala crystallises at when heated above

X	SiO ₂	Al ₂ O ₃	Ti : Ta ₂ O ₅	Ta ₂ O ₅	TiO ₂	Nb ₂ O ₅
Loss angle	0.5×10^{-4}	2.4×10^{-4}	2×10^{-4}	3.8×10^{-4}	6.3×10^{-3}	6.7×10^{-4}
Density ($kg\ m^{-3}$)	2200	3700	6425	6850	4230	4590
Thermal conductivity ($Wm^{-1}K^{-1}$)	0.5	3.3	0.6	0.6	0.45	1
Specific heat ($JK^{-1}kg^{-1}$)	746	310	269	306	130	590
Thermal expansion coefficient (K^{-1})	0.51×10^{-6}	8.4×10^{-6}	3.6×10^{-6}	3.6×10^{-6}	5×10^{-5}	5.8×10^{-6}
Thermo-optic coefficient (K^{-1})	8×10^{-6}	1.3×10^{-5}	14×10^{-6}	2.3×10^{-6}	-1.8×10^{-4}	1.43×10^{-5}
Young modulus (GPa)	60	210	140	140	290	60
Poisson's ratio	0.17	0.22	0.23	0.23	0.28	0.2
Refractive index	1.45	1.63	2.06	2.03	2.3	2.21

Table 18: List of the optical and mechanical values of different coating material at 300 K.

approximately 650°C [166]. A large and very broad loss peak has been observed in tantala heat-treated at 800°C. While of interest for studies of the loss mechanisms in tantala, crystallised tantala is not suitable for use in an HR coating due to its poor optical properties.

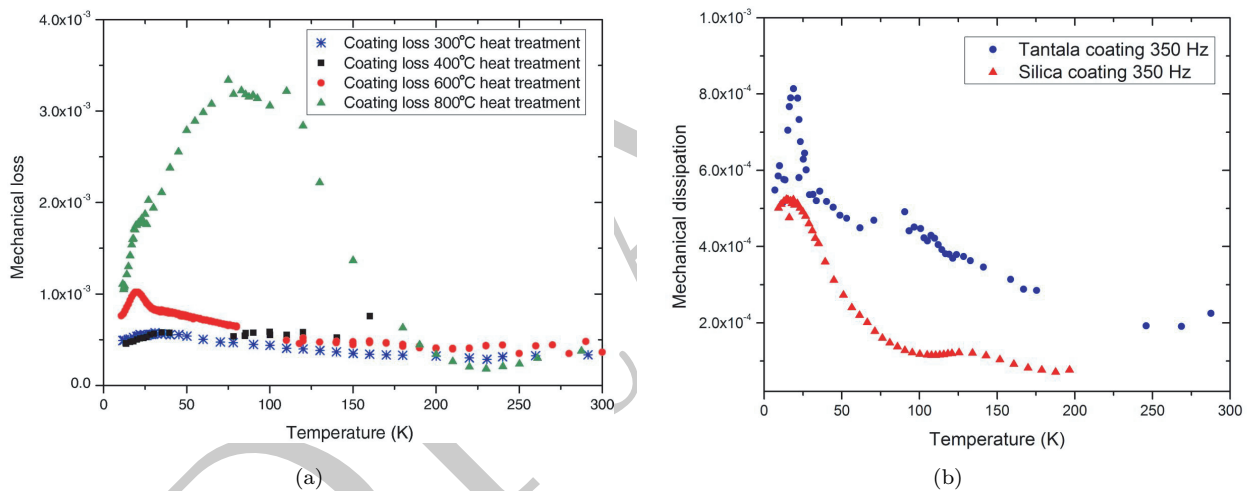


Figure 165: (a) - Measured values of the coating loss of tantala annealed at different temperatures. (b) - Comparison of 600°C heat treated tantala and silica coatings at low temperatures and 350 Hz.

Further work may be required to establish the optimum heat-treatment temperature for a silica/tantala multilayer coating for use at cryogenic temperature. High heat-treatment temperatures are generally desirable for optimal optical properties. Furthermore, studies of the mechanical loss of ion-beam sputtered silica coatings have shown a systematic reduction in the loss at room temperature with increasing heat-treatment temperatures. Thus carrying out heat-treatment at the maximum temperature which can be achieved without inducing crystallisation in the tantala layers may be desirable. However, as shown in Figure 165(a), tantala has a significantly lower loss at temperatures below 100 K when heat-treated at lower temperatures (300 or 400°C) than when heat-treated at 600°C. While the loss of the tantala layers dominate the loss of a multilayer silica/tantala coating at room temperature, the loss of ion-beam sputtered silica has a similar magnitude as the loss of tantala at temperatures below 50 K. Thus further studies of the effect of heat-treatment on the temperature dependence of the mechanical loss of ion-beam sputtered silica are also required to allow the optimal heat-treatment temperature to be chosen. In addition, measurements of the temperature dependence of the optical properties of the coating may be required.

Parameters of coatings and choice of silica/tantala to be included here. Description of current work into the R&D section.

5.9.3 Thermal noise estimates for reflective components

Author: R. Nawrodt

Thermal noise of a fully reflective mirror comprises of thermal noise arising from the bulk material and the coating. The bulk material thermal noise itself consists of Brownian thermal noise and thermo-elastic noise. Brownian noise represents the thermal fluctuations ('Brownian motion') of the atoms within the bulk material and is dependent on the sample temperature T and the mechanical loss of the bulk material ϕ [258, 259]:

$$S_x^{\text{bulk}} = 2k_B T \frac{1 - \nu}{\pi^{3/2} f Y w} \phi \quad (196)$$

with the Boltzmann constant k_B , the frequency f , the beam radius w , the substrate Poisson ratio ν and Youngs modulus Y . It is obvious that the Brownian thermal noise is only dependent on mechanical properties of the material.

The thermo-elastic noise of the bulk material is created by statistical temperature fluctuations. By means of the coefficient of thermal expansion α these fluctuations are translated into displacement noise. The thermo-elastic spectral noise density is given by [114]:

$$S_{\text{TE}}^{\text{bulk}} = \frac{4k_B T^2 \alpha^2 (1 + \nu)^2 \kappa}{\sqrt{\pi^5} \rho^2 C^2 f^2 w^3} \quad (197)$$

with the coefficient of thermal expansion α , the thermal conductivity κ , the heat capacity C and the mass density ρ . This equation is valid if the thermal diffusion lengths

$$l_{\text{th}} = \sqrt{\frac{a^2}{f}} \quad (198)$$

of the material is smaller than the beam diameter. The parameter $a^2 = \kappa/(\rho C)$. This assumption is called the adiabatic case. During one period of oscillation all temperature fluctuations that are present at the observation volume stay inside this volume. If the thermal diffusion lengths gets larger (e.g. by means of high thermal conductivity or low frequencies) the thermo-elastic effect gets weaker. Especially, for low temperature applications this non-adiabatic correction becomes important and reduces the contribution of thermo-elastic noise further. This correction has been taken into account for all calculations presented in this document. Details of the calculation can be found in [152, 382].

Figure 166 compares the Brownian and thermo-elastic noise of one single mirror made of fused silica, sapphire or silicon at 10 and 300 K. The parameters used for the calculation are listed in table 16 and 17.

At room temperature fused silica provides the lowest level of thermal noise due to its low mechanical loss and small coefficient of thermal expansion (see figure 166(a)). All crystalline materials show a high coefficient of thermal expansion and thus a large thermo-elastic noise. Therefore, crystalline materials need to be avoided at room temperature detectors in order to achieve the minimum thermal noise level of a mirror substrate.

In contrast, at low temperatures fused silica has a large mechanical loss reaching values of 10^{-3} around 10 K. Crystalline materials behave differently resulting in a low mechanical loss of better 10^{-8} at low temperatures (see tab. 16). Additionally, the coefficient of thermal expansion is very small at low temperatures. This reduces dramatically the thermo-elastic noise contribution compared to room temperature operation (see figure 166(b)). Thus, using cryogenic temperatures and crystalline materials will result in a low total bulk thermal noise.

Figure 167 compares the total bulk thermal-noise consisting of thermo-elastic and Brownian thermal noise for sapphire and silicon at selected temperatures. Due to the small mechanical loss and coefficient of thermal expansion a low thermal noise level is achieved. At 20 K both materials show a comparable thermal noise level. At higher temperatures thermo-elastic noise becomes dominant. Here, sapphire has a slightly lower level of

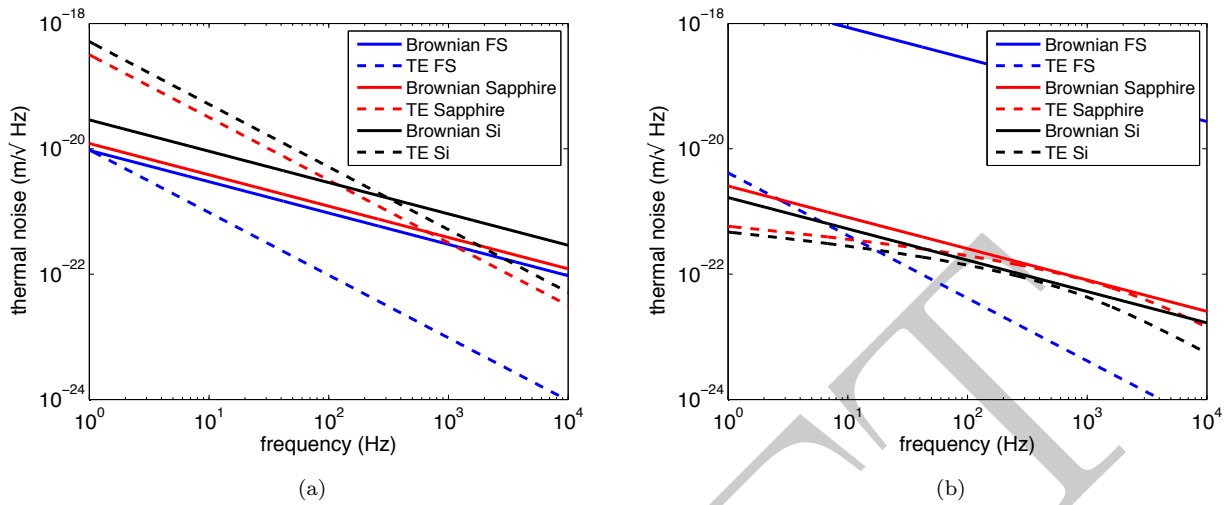


Figure 166: Comparison of the Brownian and thermo-elastic noise for fused silica, sapphire and silicon at 300 K (a) and 10 K (b) (TE - thermo-elastic noise, FS - fused silica). At room temperature the crystalline substrate materials show a large thermo-elastic noise. In contrast, at cryogenic temperatures fused silica has a large Brownian thermal noise due to its large mechanical loss.

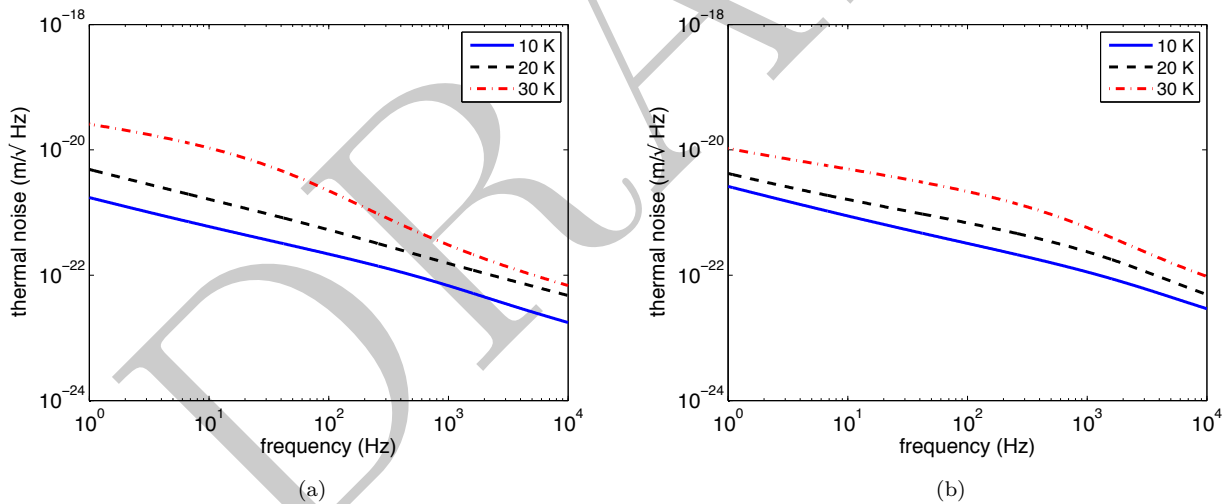


Figure 167: Comparison of the total bulk thermal noise of a mirror substrate made of silicon (a) and sapphire (b) at different temperatures. The parameters used for this calculation are summarised in table 16 and 17.

thermo-elastic noise due to the combination of its thermal properties (mainly the high thermal conductivity). At 10 K silicon has a slightly lower total thermal noise as a sapphire mirror substrate.

All calculations so far are based on semi-infinite mirror substrates. This assumption is true for a first comparison of the materials and in cases where the beam radius compared to the mirror radius is small. However, for an application in gravitational wave detectors it is preferable to increase the beam diameter to the maximum possible size that is in agreement with the optical clipping losses. The corrections for finite size test masses has been made by different authors for the different noise contributions. The calculations are quite long and thus only the results are shown here. The detailed discussion can be found in the literature [98, 335].

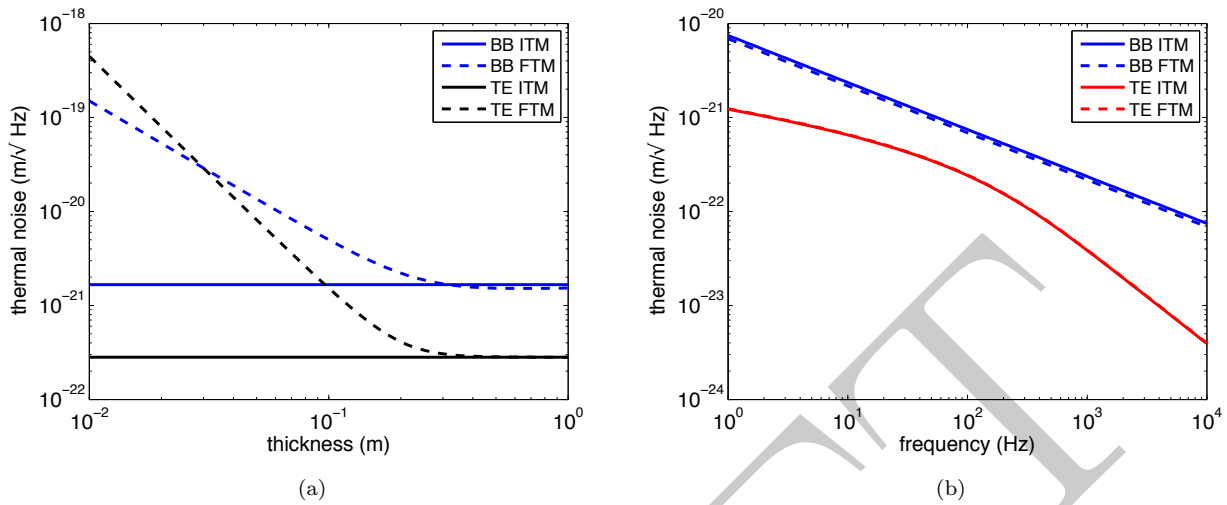


Figure 168: Finite size test mass mirror thermal noise. (a) - Dependence of the mirror Brownian and thermo-elastic thermal noise of the thickness of the substrate (silicon, 10 K, diameter: 0.5 m, frequency 10 Hz). (b) - Effect of the finite size correction for a typical ET end mirror geometry (silicon, 10 K). BB - bulk Brownian, TE - thermo-elastic, ITM - inner test mass, ETM - end test mass.

Figure 168 gives the dependence of the substrate thermal noise. It is obvious that for reasonable thicknesses ~~the~~ substrate the correction is small. Only for very thin substrates a strong deviation from the simplified infinite half space model appears. At larger thicknesses the finite sample correction leads to a small decrease in thermal noise (approx. 5...10% for bulk Brownian and less than 1% for bulk thermo-elastic noise).

Optical components being used in GW detectors consist of a bulk material and a coating. The coating usually comprises of several alternating dielectric layers formed by high and low refractive index materials. Typically, these layers are formed by amorphous tantala and silica layers with an optical thickness of $\lambda/4$. The circulating laser beam of the interferometer interacts mainly with the coating ~~point of first contact between light and matters~~. Thus, it can be expected that the optical coating contribute strongly to the total thermal noise of a mirror.

Similar to the thermal noise of the bulk materials coatings show Brownian thermal noise. It is again dependent on the temperature T and the effective mechanical loss ϕ_{eff} of the coating [258, 259]:

$$S_x^{\text{coating}} = 2k_B T \frac{1 - \nu}{\pi^{3/2} f Y w} \phi_{\text{eff}} \quad (199)$$

with the Boltzmann constant k_B , the frequency f , the beam radius w , the Poisson ratio ν and the Young's modulus Y of the substrate bulk material. The effective mechanical loss contains all coating relevant parameters and is given by:

$$\phi_{\text{eff}} = \frac{t}{\sqrt{\pi} w} \left(\frac{Y}{Y_{\perp}} \phi_{\perp} + \frac{Y_{\parallel}}{Y} \phi_{\parallel} \right). \quad (200)$$

This description of the effective mechanical loss assumes small Poisson ratios of the coating materials which is usually fulfilled. t is the total thickness of the coating layer. The Young's moduli Y_i , the thicknesses t_i and the mechanical losses ϕ_i are combined as follows (i=1,2 to indicate the different coating layer properties):

$$Y_{\perp} = \frac{t_1 + t_2}{\frac{t_1}{Y_1} + \frac{t_2}{Y_2}}, \tag{201}$$

$$Y_{\parallel} = \frac{Y_1 t_1 + Y_2 t_2}{t_1 + t_2}, \tag{202}$$

$$\phi_{\perp} = \frac{Y_{\perp}}{t_1 + t_2} \left(\frac{t_1}{Y_1} \phi_1 + \frac{t_2}{Y_2} \phi_2 \right) \tag{203}$$

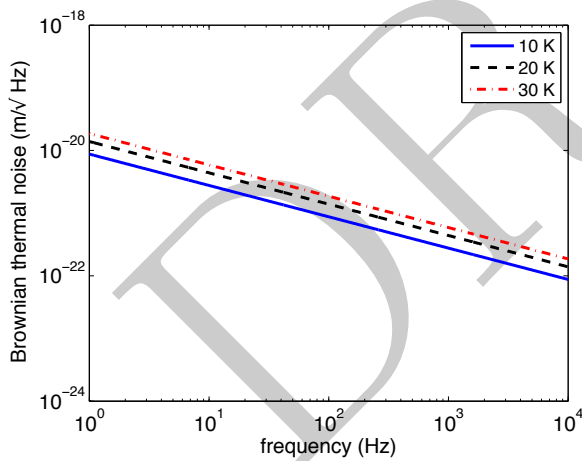
$$\phi_{\parallel} = \frac{Y_1 t_1 \phi_1 + Y_2 t_2 \phi_2}{Y_{\parallel} (t_1 + t_2)} \tag{204}$$

Light penetrates the first dielectric layers of a high-reflective mirror and thus interacts not only with the front surface. Here, a fluctuating local temperature causes a change in the thickness of the layer by means of the coefficient of thermal expansion α and additionally a change of the refractive index n of the materials. In total, these two effects sum up and change the optical path of the light being reflected. This statistical process combining effects of thermo-elastic (due to α) and thermo-refractive (due to the change of n) is called thermo-optical noise. Depending on the sign of α and dn/dT these two effects can result in a smaller noise than the two terms predict separately.

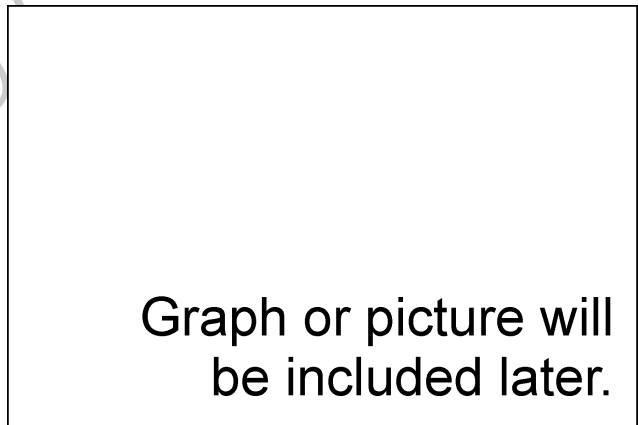
Thermo-optical noise can be calculated following [?]:

$$S_{TO}^{coating} = \dots \tag{205}$$

with ... [equation from ET note](#)



(a)



(b)

Figure 169: (a) – Comparison of coating Brownian noise at different temperatures. (b) – Comparison of coating thermo-optical and Brownian noise at room temperature.

Figure 169 compares the Brownian and thermo-optical noise levels of different coatings at low temperatures and room temperature. Parameters are used from table X and Y [include link](#). A direct comparison reveals that the thermo-optical noise is much smaller than the coating Brownian noise. The level of coating Brownian noise is additionally larger than the total noise level of the bulk material presented in figure 167. Thus, coating Brownian noise is the most important type of thermal noise of a high reflective mirror and great care must be taken in choosing the optimum operational temperature and to choose the appropriate material combination. Details of the ongoing and future research are given in section 5.15.

5.9.4 Thermal noise estimates for transmissive components

J. Franc

The total thermal noise of a transmissive component considers the noise contribution described in the previous subsection and additionally the thermo-refractive noise that occurs from statistical fluctuations of the refractive index n due to its temperature dependence dn/dT . A temperature fluctuation produces a small change of n which leads to phase changes detected by the interferometer.

The thermo-refractive noise has been calculated by equations given by Braginsky [112] in addition with correction terms developed by Benthem and Levin [80].

Taking into account the configuration of Einstein telescope given in figure ?? and table ?? results in the following equation for the thermo-refractive noise in an interferometer with arm cavities of a finesse F :

Crosscheck by Janyce - break up equation into two lines if needed

$$\sqrt{S_h(f, T)} = 2\sqrt{2} \sqrt{1 + \left(\frac{f}{fc}\right)^2} \frac{1}{L} \frac{\lambda}{8F} \sqrt{(kl\beta)^2 \frac{4kbT^2\kappa}{(C\rho)^2 l} \left(1 + \frac{(kn)^2 w^2}{\left(1 + \left(2kn\sqrt{\frac{\kappa}{C\rho\omega}}\right)^4\right)}\right) \int_0^{\infty} \frac{k_i dk_i}{2\pi i} \exp\left(\frac{-Rb^2 k_i^2}{2}\right) \frac{k_i^2}{\omega^2 + a^4 k^4}} \quad (206)$$

with : l is the thickness of the input mirror, β the thermo-optic coefficient of the substrate material, T is the temperature, k_B the Boltzmanns constant, κ the thermal conductivity, C the specific heat, ρ the density of the substrate material, R_b the size of the laser beam which one?, L the arm length of the interferometer and the refractive index n of the substrate material. Details of this equation can be found in [214].

The thermo-refractive noise is compared here for silicon and sapphire as the most promising test mass materials at cryogenic temperatures. The substrate thermo-refractive noise is largely dependent on the thermo-optic coefficient. This values has been measured for sapphire at low temperature and reaches $9 \times 10^{-8} 1/K$ at around 20 K [?]. For silicon the parameter is not very well known. The currently only literature source reports values of n and dn/dT down to 30 K [221]. However, the values reported for dn/dT do not agree with the slope of the $n(T)$ curve. Thus, the knowledge of the parameter is strongly limited. A detailed discussion what can be estimated at temperatures below 30 K can be found in [?]. At temperatures around 20 K a value of $1 \times 10^{-6} 1/K$ can be assumed as an upper limit of dn/dt based on the experimental values given in [221]. At even lower temperatures it is reasonable to assume a further decrease due to thermodynamical assumptions (see [?] for details).

Figure 170(a) shows the thermo-refractive noise of silicon and sapphire at 10 K based on equation (206) given above. Recently, a new estimation of ET detector has been provided (referred to ET-D sensitivity). This new sensitivity assumes a reduced radius beam size of 9 cm, corresponding to an effective test mass diameter of 45 cm, but at the same time keep the overall test mass weight at about 200 kg ([?]). This mass leads to a thickness for a future silicon test mass of 50 cm approximately. The thickness drops to more or less 30 cm for Sapphire due to the higher material density. In the case of substrate thermo-refractive noise is dependent on the thickness of the mirror. The thickness of the future test mass will be confirmed subsequently. The following simulation are therefore given for information only and are open to improvement in the next months.

We should rewrite this section. This optimization within the next month is our job. At the end we need one design. Here we should only show the comparison of materials. Optimization will be the task of section 5.9.5.

The sapphire substrate shows a very small thermo-refractive noise that is well below the sensitivity curve of ET. The silicon substrate also shows a low thermo-refractive noise at low frequencies. The operational frequency of the LF detector is between 1 and 250 Hz. Above this frequency the HF detector takes over and limits the sensitivity of the Einstein Telescope. Therefore, a cooled silicon mirror provides a low enough thermo-refractive noise in the frequency band covered by the LF detector. These estimates are based on reasonable upper limit

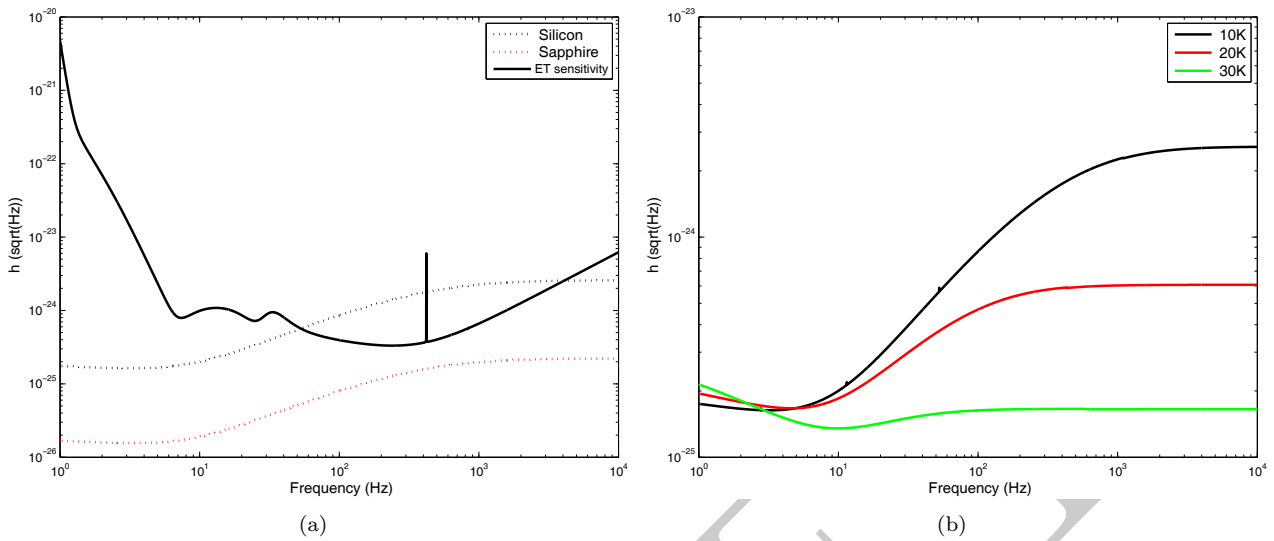


Figure 170: (a) - Substrate thermo-refractive noise of silicon and sapphire at 10 K (diameter: 45 cm, beam size: 9 cm, mass ~ 200 kg). (b) - Substrate thermo-refractive noise of silicon at 10 K, 20 K, 30 K.

extrapolation values for dn/dT [?]. It can be expected that an experimental values for the thermo-refractive coefficient of silicon is even lower than given here.

Figure 170(b) shows the evolution of the thermo-refractive noise for different temperatures (10 K, 20 K, 30 K). It shows that the thermo-refractive noise decreases with the temperature. Thus, operating at the highest possible temperature that allows a low thermal noise operation is preferred. This leads to an optimization process that is described in section 5.9.5.

In conclusion, both materials - sapphire and silicon - provide low thermo-refractive noise levels that are compatible with the requirements for the Einstein Telescope. An exact estimate of the thermo-refractive noise level of silicon will not be possible until the thermo-refractive coefficient is measured for different types of silicon. It can be expected that this parameter strongly depends on the level of doping. Several institutions are currently working on experiments to extend the existing parameters to temperatures below 30 K.

5.9.5 LF interferometer large mirror definition

Author(s): R. Nawrodt, J. Franc

final definition of a low temperature end mirror and input coupler based on the above estimates, this section is the result of all thermal noise analysis and will be included at the end

5.9.6 HF interferometer large mirror definition

Author(s): J. Franc

final definition of the high temperature end mirror and input coupler based on the above estimates, this section is the result of all thermal noise analysis and will be included at the end

Fused Silica is the material of choice for the high frequency detector operating at room temperature. This material has already proven its reliability in GW detectors currently under operation (e.g. LIGO, VIRO,

GEO600) due to its excellent optical properties. Fused Silica is one of the commonly used materials in optics and has been improved during many decades. Appropriate polishing methods exist to obtain a very high surface quality. Fused Silica has remarkable properties at room temperature: low mechanical loss (see section 5.16.2) which leads to a small substrate Brownian noise and an exceptional low coefficient of thermal expansion (see section 5.16.3) which results in a small thermo-elastic noise.

Parameter	ET-HF
temperature	290 K
arm length	10 km
mirror material	Fused Silica
mirror diameter	62 cm
mirror thickness	30 cm
mirror mass	200 kg
laser wavelength	1064 nm
beam shape	HG ₀₀
beam radius	12 cm
coating high index	Ti : Ta ₂ O ₅
coating low index	SiO ₂

Table 19: Summary of the parameters used for the thermal noise estimate of the HF interferometer.

The assumed parameters for the HF interferometer are listed in Table 19. The mirror geometry was chosen that the mass reaches 200 kg (to suppress radiation pressure noise) and that the mirror has 1 ppm diffraction loss [546]. In order to compare the behaviour of different substrate materials the thermal noise of a high reflectivity mirror was calculated using the same 'standard' coating and different substrate materials. The 'standard' coating is a multilayer (HL)17HLL coating made of Ti : Ta₂O₅ and SiO₂ quarter wavelength layers. On a fused silica substrate this coating corresponds to a transmission of 6 ppm. The lowest mechanical losses have been considered for the coating materials (see section 5.16.2). The result of this comparison is shown in Figure 171. The graph compiles different noise sources in the substrate material as well as the coating.

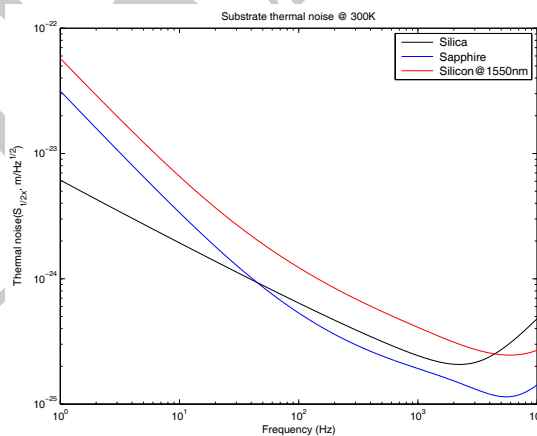


Figure 171: Total thermal noise of 3 different substrates at 300K: Silica, Sapphire and Silicon @ 1550 nm.

At 300 K, silicon is unsuitable due to its large mechanical loss angle. The total thermal noise for silicon is limited by two substrate thermal noises: substrate brownian noise at high frequency and substrate thermo-elastic noise at low frequency. Sapphire must be also turned down due to its large thermoelastic noise at low frequency. Therefore, the most adapted substrate at room temperature is fused silica. In this case, coating limits the sensitivity of the future detectors only through the Brownian motion. The fused silica thermal noise does not play a role in the sensitivity limitation that is why this substrate has been chosen for a GWD working at 300 K [215].

Mirror coating Author(s): J. Franc

As explained above, the total thermal noise of the test masses is a combination of coating Brownian, substrate Brownian, substrate thermo-elastic, substrate thermo-refractive noise and thermo-optic noise. Taken into account this five noises, the coating Brownian noise is the most important one and can limit sensitivity target. A state-of-the-art of different coating material have been realized in order to compare different combination of multilayer stacks. Figure 172 shows the total thermal noise for different coatings on a silica substrate at room temperature. The calculations are based on the currently best available data of the materials (18). Each coating correspond to a transmission of 6 ppm on a fused silica mirror. Therefore, all multilayer are different according to materials taken into account. We need (HL)17HLL for coating made of Ti : Ta₂O₅ and SiO₂ quarter wavelength layers, (HL)13HLL for coating made of TiO₂ and SiO₂, (HL)13HLL for coating made of TiO₂ and SiO₂ (HL)13HLL for coating made of Nb₂O₅ and SiO₂, (HL)13HLL for coating made of TiO₂ and SiO₂ (HL)16HLL for coating made of ZrO₂ and SiO₂, (HL)24HLL for coating made of Ti : Ta₂O₅ and Al₂O₃ and (HL)22HLL for coating made of ZrO₂ and Al₂O₃. According to refractive index value of material the number of layer can double.

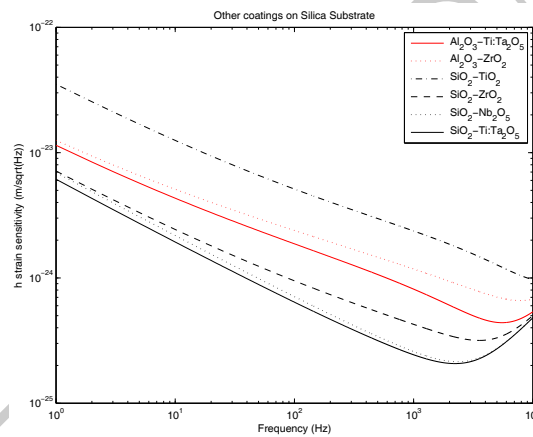


Figure 172: Comparison of the thermal noise of different coating materials on a fused silica substrate.

There is a clear advantage for the SiO₂ – Ti : Ta₂O₅ coating. The results obtained for SiO₂ – Nb₂O₅ and SiO₂ – ZrO₂ are encouraging as well. However, including the optical absorption of the coatings even stronger supports the use of the standard coating. So far, there is no better coating to be used at room temperature than the Ti : Ta₂O₅ – SiO₂. Therefore according to the results demonstrated in this section, the figure 173 show the different thermal noises contribution for this kind of mirror.

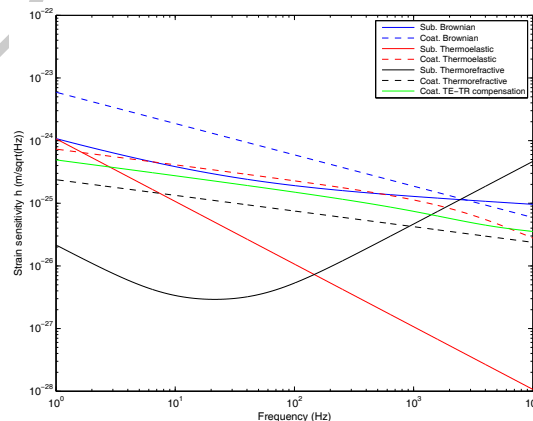


Figure 173: Contribution of the different thermal noises for a silica mirror.

In conclusion, we have evaluated the total mirror thermal noise at room temperatures by implementing a model that includes Brownian noise, thermo elastic and thermo refractive noise. The different simulations presented and calculated with the parameters listed above allows understanding that silica is the good test mass material for the High frequency detector of the 3rd generation of GWD. The optimized mirror for the HF interferometer is, at present, a silica test mass with a diameter of 62 cm and a thickness of 30 cm. The best coating remains a multilayer system made of seventeen doublets of Ti : Ta₂O₅ and SiO₂.

5.9.7 Mirror surface defects

Mirror surface defects are investigated in order to understand their effects on cavity resonance and losses, and to define requirements for surface polishing. For convenience, the mirror surface deviations from the perfect surface can be classified in two categories, depending on their spatial frequencies. Defects in the high frequency range (above a few hundred m⁻¹) will scatter light outside the cavity and thus generate cavity losses and scattering noise. Defects in the spatial low frequency range (between 1 and 100 m⁻¹) may induce resonance of unwanted modes in the cavity, and thus degrade the mode purity inside the cavity.

The ET arm cavities were simulated by FFT propagation using the simulation software *SIESTA* [145]. Artificial mirror maps were applied to both mirrors of the cavity. The artificial maps were randomly generated in order to reproduce a defect distribution similar to that found in actual VIRGO and LIGO mirrors [227–229].

Table 20 shows the cavity gain and round-trip losses for the fundamental mode resonating in the cavity (wavelength of 1064 or 1550 nm), with varying RMS flatness of the surface defects. The defects distribution considered here goes as f^{-2} , where f is the spatial frequency. It has been shown in [229] that such a distribution, with a RMS of 1.0 nm, overestimates the low-frequency defects with respect to what has already been obtained for the Advanced LIGO mirrors. Therefore the surfaces obtained by current polishing techniques seem already good enough to obtain reasonably small round-trip losses for the fundamental mode. Using a wavelength of 1550 nm is particularly favourable from this point of view (smaller losses).

The situation for LG₃₃ is more delicate. It has been shown [229] that LG₃₃ is significantly more sensitive than the fundamental mode to surface defects in the low spatial frequency range. Essentially, since a cavity tuned for LG₃₃ is degenerate for all modes of order 9, the low-frequency defects induce the coupling between the injected LG₃₃ and the other modes of the same order. Polishing techniques such as corrective coating or ion beam polishing are able to reduce the amount of defects in the low-frequency region, approximately below 100 m⁻¹ (1 cm⁻¹). Ion beam polishing has currently been used for Advanced LIGO, whereas corrective coating is under evaluation for Advanced VIRGO. Preliminary results indicate that a further improvement is required for LG₃₃ with respect to the state of the art of such techniques. More work is planned to verify the agreement of FFT simulations with experiments on LG₃₃ (see section 5.15.1).

In addition to the above work, the coupling between higher-order modes due to mirror surface defects was investigated using a frequency domain simulation tool, *Finesse* [97]. In this work, similarly to the simulation mentioned above, a Fabry-Perot cavity with imperfect mirrors was simulated. Real surface maps of VIRGO mirrors were reconstructed by fitting with Zernike polynomials, and an artificial map was built by a sum of Zernike polynomials. A LG₃₃ beam was injected into a cavity where a surface map was applied on one of the two cavity mirrors. The light field inside the cavity was analyzed and found not only the couplings between the same order, but also the frequency split of the resonant frequency which will result in quasi-degenerate modes.

The next step is to expand the optical configuration to a realistic topology such as an RSE interferometer in order to obtain practical requirements for the mirror surface. Also, the effects of advanced polishing techniques such as corrective coating or ion beam polishing need to be better understood.

Reminder during writing

- coating TN as serious noise candidate
- description of all dependencies from equations (links to ET notes), optimisation plots

RMS flatness	LG ₀₀ 1064 nm		LG ₀₀ 1550 nm	
	cavity gain	r.t. losses [ppm]	cavity gain	r.t. losses [ppm]
0 nm	567.4	2	567.4	3
0.5 nm	564.5 ± 0.9	20 ± 6	566.7 ± 0.3	7 ± 2
1.0 nm	555.9 ± 3.7	73 ± 24	564.4 ± 0.9	21 ± 6

Table 20: Cavity gain and round-trip losses for the arm cavities, computed from FFT simulations, as a function of surface defects RMS. The fundamental LG₀₀ mode is considered, for the wavelengths 1064 and 1550 nm. Data are expressed as mean ± standard deviation on an ensemble of 10 different cavities. For each cavity, random surface maps with a given RMS amount of defects are applied to both mirrors. The random surface maps are generated from a f^{-2} spectral distribution.

- possible coating materials for cryogenic operation (tantala, silica, hafnia, etc. - link to appendix with parameters)
- discussion of properties, links into (near) future R&D (links to Sec. 5.15)
- definition of coatings (number of layers, optimisation due to reflectivity, absorption and TN), include options (layer thickness) and give estimates on the influence
- ...
- silicon as test mass material → limitations (TR noise, size, absorption), sapphire option
- LF interferometer at low temperatures - thermal properties and parameters at low temperatures (link to appendix)
- definition of geometry, availability (several size options for comparison)
- temperature stabilisation (cooling) - limits in laser power due to absorption (links to suspension and cooling definition)
- ...

5.10 Injection system

Author(s): *S. Hild, A. Thuering*

5.10.1 Pre-stabilized laser

At the development time of second generation GWDs, neodymium doped yttrium aluminum garnet (Nd:YAG) was the best choice as the gain material for 100 W class lasers. However, in the last years, particularly thin disc lasers based on ytterbium doped crystals have been undergoing a rapid development. While the pure power scaling of these systems into the multi-kW range was mainly driven either by material processing or defense applications [188, 291] which do neither require single-frequency nor fundamental mode output, good progress has also been achieved in the power scaling of high beam quality laser systems. In particular, near fundamental mode operation with more than 200 W of output power and up to 98 W of single-frequency output power has been demonstrated [237]. Further possible advantages are that the 940 nm pump diodes used for e.g. Yb:YAG have potentially longer lifetimes than their 808 nm Nd:YAG counterparts and that the lower quantum defect of Yb:YAG causes less thermal effects. However, its main disadvantage is that Yb:YAG is a quasi-3-level system and thus more sensitive to increased temperatures within the gain medium.

Different design concepts are proposed to produce lasers with power levels of several 100 W and to amplify these systems into the kW region. The main concerns are the thermal management in the gain material and to reduce beam aberrations. In particular, Nd:YAG suffers from a significantly higher quantum defect compared

to Yb:YAG making the thermal management even more important. One way to reduce the thermal effects is to use a zig-zag beam path to average over the thermal gradient in the laser crystal. Edge-pumped slab geometries can be combined with conduction-cooling techniques which avoid vibrations introduced by cooling fluids in conventional layouts. However, one of the main challenges in using slabs is to avoid parasitic oscillations within the high gain regions.

Problems caused by depolarization and by defocusing can be addressed in different ways. In principle, an efficient birefringence compensation can be implemented [339]. However, better than compensating effects is to reduce these. For this, there are in principle two different options. Firstly, Koechner and Rice [308] and Soms et al. [498] have shown that the amount of depolarization depends on the Nd:YAG crystal orientation. Therefore, crystal orientations other than the standard [111]-cut could be an option to reduce the depolarization intrinsically. Shoji and Taira [488] suggested the use of [110]-cut crystals in combination with small beam size in the high pumping regime to reduce depolarization. In recent experiments [421], the [100]-, [110]- and [111]-crystal orientations were compared in a single pass configuration in the pump power regime relevant for 2nd generation GWD. Although these results are very promising in terms of intrinsic reduction of depolarization effects, they also show that the non-symmetrical shape of the thermal lens in unconventionally cut crystals might limit the achievable beam quality in laser oscillators.

The second option is to reduce the thermal gradients which cause the stress-induced birefringence effects. By the use of multi-segmented laser rods, the maximum peak temperature of an end-pumped laser rod or slab can be reduced as shown in the work by Wilhelm et al. [560, 561]. To decrease the overall heat load in a Nd:YAG laser media the pump wavelength can be changed from 807 nm to 885 nm which reduces the quantum defect and therefore the overall heat load by more than 30% (see e.g. [216, 327]). Core doped rods can be used (see e.g. [314]) to achieve an easier and more stable fundamental mode operation. These rods are comparable to a double clad fiber as described by Bedö et al. [68] where only the inner core of the rod is doped and the outer core is used as a waveguide for the pump light. As the gain is only present in the doped inner core of the rod, this concept is similar to mode selective pumping, but has the advantage that no high brightness pump source is required.

Optical fiber amplifiers have a high potential to offer single-frequency output at higher efficiencies and at lower cost than solid-state amplifiers at similar power levels (see for example the overview paper by Limpert et al. [331]). Until several years ago diode-pumped fiber amplifiers were limited to power levels of several Watts due to the unavailability of high brightness pump diodes and due to nonlinear effects in the fiber such as stimulated Raman scattering and stimulated Brillouin scattering (SBS). The invention of large mode-area (LMA) fibers and of photonic crystal fibers (PCF) has enabled output powers of single-mode fiber lasers to exceed 1 kW while retaining excellent efficiencies (see for example Jeong et al. [287]). The large effective core diameter of these fibers decreases the average intensity of the light at the laser wavelength in the fiber and thereby increases the threshold of nonlinear processes. The large outer cladding of the double-clad LMA fibers allows high power multi-mode pumps to be coupled into the fiber. Bending losses can be used to ensure that the output remains single-mode, despite the large diameter of the core. The limiting factor for narrow-linewidth high-power fiber lasers for the use in GWDs is the onset of SBS.

A state-of-the art single-frequency fiber amplifier system with 150 W of output power with a good output beam profile (92% in TEM₀₀) is described in [269]. The optical-to-optical efficiency of this system with respect to incident pump power is 78% for a 195 W pump source. A good polarization ratio of about 100/1 was achieved. Recently, the output power of single-frequency, PCF-based, ytterbium-doped fiber amplifiers has been scaled to more than 400 W of output power [450].

A different approach to realize LMA fibers with excellent output beam quality and simultaneously larger mode areas are multifilament-core (MFC) fibers with core regions consisting of many small doped filaments. In contrast to conventional multi-core design, the multifilament core fibers aim for strong coupling between smaller filaments resulting in the propagation of only one supermode by adequately choosing diameter and spacing of the filaments. In the last years, MFC fibers with active and also with passive filaments were demonstrated, which enabled transversely single-mode output with nearly Gaussian-shaped intensity mode profile [139, 551]. The main advantage of this new fiber type is the low effective core numerical aperture which can be achieved without the need of flattening the refractive index profile as it is crucial for PCFs. Important properties of the

MFC fibers, e.g. the low bending losses, can be explained using an equivalent step index based on the theory of the fundamental space filling mode [140]. Recently, it has been demonstrated that a TEM₀₀ mode content of more than 95% can be achieved with such an actively doped fiber [317].

Novel ideas to increase the SBS threshold are under investigation. A promising concept is to shift the Brillouin frequency along the fiber to lower the effective Brillouin gain for each frequency component. This could be achieved by temperature or strain gradients, or by varying doping concentrations along the fiber. In addition to the reduction of nonlinear scattering effect, the reliability and noise performance of high power fiber lasers need to be further analyzed and possibly improved to meet the requirements of third generation gravitational wave detectors. Especially thermal effects and contamination at the air-glass interface have to be considered. The main problem is the large light intensity at these interfaces which could be reduced by undoped beam expansion section at the fiber ends or by all-fiber solutions for the pump-light coupling. One big advantage of fiber lasers is that they are compact and simple compared to the complex solid-state laser systems. Furthermore, modern splice techniques allow one to produce an all-fiber system including the master oscillator, the high power stage and possibly even a mode-cleaning fiber if required.

Erbium-doped fiber lasers emit around 1.56 μm where the absorption in silicon is small compared to the initially used silica at 1 μm wavelength. For an efficient design with low nonlinear effects in single frequency operation, the erbium-doped fiber should have high pump absorption and should be as short as possible. Unfortunately, the pump absorption cross sections of erbium are about a factor of 10 lower than those of ytterbium. In addition, quenching effects also limit the sensible doping concentrations to about a factor of 10 below that of ytterbium. This combined factors result in an about two orders of magnitude lower pump absorption of erbium doped fibers, if similar fiber geometries as used with ytterbium doped fibers are assumed. In order to avoid excessive fiber lengths, which is necessary to circumvent the onset of SBS, either the single-core to pump-core ratio has to be adapted or the amplifier has even to be pumped into the single-mode signal core. For this reasons, pump sources with very brightness or even single-mode beam quality are needed. This becomes even more obvious if the typically achieved optical-to-optical efficiencies of about 25%-30% (50% for 1480 nm pumping) are compared with the typical value of > 70% for ytterbium. Recently, a single-mode output power at 1480 nm was demonstrated with a Raman fiber laser [385] which can be used as a pump source for single-mode Er based systems. However, commercially available single-mode Raman fiber laser modules are currently limited to an output power of 10–20 W.

In order to overcome these limitations, Yb codoping of the Er-doped fiber and pumping at 980 nm can be used. This allows high pump absorption but also implicates a second gain band at the Yb wavelength around 1 μm . This second gain bands limits the achievable output power due to the onset of massive amplified spontaneous emission (ASE) which finally leads to pulsing instabilities of the amplifier system. The highest single-frequency output power of 151 W achieved with this concept was accompanied by more than 70 W of ASE at 1 μm [288]. Nevertheless in recent experiments a new scheme was demonstrated by which the 1 μm oscillation in an Er-Yb codoped fiber amplifier could be effectively suppressed [316].

Concerning the direct generation or the amplification of spatial beam profiles other than the fundamental (fiber) mode, only very limited experimental results have been published. A good overview is given in the review article by Ramachandran et al. [430]. For the generation of the higher order mode, the laser light is first coupled into the fundamental LP₀₁ mode of a single-mode fiber. Then, an in-fiber long-period Bragg grating converts the LP₀₁ into the desired LP_{0m} mode. This process can be very efficient with peak efficiencies of more than 99%. The usage of higher order modes in the optical fibers has several advantages compared to the fundamental mode. Firstly, the effective mode area is significantly enlarged increasing the threshold for SBS. Furthermore, the higher order modes are less sensitive to mode distortions due to fiber bending or refractive index profile imperfections due to the fiber fabrication process. Recently, fiber amplifiers have been demonstrated employing this technique for the first time in an active fiber with several Watts of output power [384, 386]. However, the used higher order LP_{0m} modes all have a central high intensity peak in common which is undesirable for the use in GWD [549]. Thus, some research both on the generation of axisymmetric fiber modes with an intensity minimum in the center as well as on the amplification of these modes will have to be carried out. Most probably, this will also involve some special design of active fibers in which the active dopant distribution favors the amplification of the mode of interest.

As many different applications drive the laser development worldwide, many laser concepts at different wavelength and power levels are already available and advances in several fields are to be expected. Even though the large variety of optical layout and topology options for GWDs require a similarly large range of different laser parameters, we expect that at least one, if not more laser designs will allow one to build a laser source with the required power, wavelength and spatial profile.

5.10.2 Injection optics

Overview and General requirements

The Input Optics system (IO) of ET takes care of the optics downstream of the high power laser (1064nm) and low power one (1550nm). The whole system must deliver a beam with the required power, geometrical shape, frequency and angular stability at the Interferometer input. The general requirements for ET-LF and ET-HF IO system are listed in Table 21.

Requirement	Value at 1064 nm	Value at 1550 nm
Laser power available at the ITF input	500W	3W
Intensity noise	TBD	TBD
Beam jitter noise (misalignment mode amplitude)	TBD	TBD
IMC cavities throughput	>80% on LG_{33}	>80% on LG_{00}
IO overall throughput	>50% on LG_{33}	>50% on LG_{00}

Table 21: Requirements for the ET Input Optics (IO) system

An Electro-Optic Modulation (EOM) system should provide the needed RF phase or amplitude modulations (to sense longitudinal and angular degrees of freedom). Two in-vacuum suspended input mode cleaners (IMC) in series will be used to geometrically clean the beam and reduce its amplitude and lateral fluctuation. The resonant IMC could also serve in the loop of laser frequency stabilization. After the IMC an intensity stabilization section will provide the signal for stabilizing the laser RIN and reach the requirements. An in-vacuum Faraday isolator will prevent interaction of the ITF (interferometer) reflected light with the IMC and laser system. Finally, a mode matching telescope will give to the beam the correct dimension for matching it onto the interferometer. It is planned to use super-polished optics for ET-HF and ET-LF in order to lower as much as possible diffused light noise that could become a limiting noise. Moreover the beam pointing noise created in components in free-space propagation (mirrors, lenses, EOM, FI, etc. . .) can be dominated by acoustic, seismic and thermal noise. A particular care should be given to isolate the optics from seismic noise and as often as possible install all the sensors used in the control loops on suspended benches in the vacuum vessel of ET.

Input Mode Cleaner (IMC)

The laser light must be frequency and spatially stabilized before it can be used in the interferometer. The input mode cleaner (IMC) provides active frequency stabilization through feedback to the laser, passive frequency noise suppression above its cavity pole frequency, and passive spatial stabilization at all frequencies. The input mode cleaner also reduces higher order modal content of the laser light, suppressing beam jitter by a factor depending of the cavity Finesse.

The baseline configuration of the IMC for ET-HF is to use two 20 meter long IMC cavities placed in series (as done in GEO interferometer). Due to the high laser power that should be stored in the IMC cavity, radiation pressure effect and absorption in IMC cavity input and output mirrors should be the main limiting effects with such a high power. The radiation pressure effect will depend on the cavity finesse chosen. In Advanced Virgo, with about 60 kW power stored in this cavity it has been shown that the radiation pressure effect on angular degrees of freedom is manageable by using at least 3 kg mirror [233]. This means that this effect could be overcome by increasing the IMC mirrors weight or reducing the Finesse if possible. For the lock acquisition of the cavity it is likely that we need to lock the cavity at a lower power and go to full power once the cavity is locked [233]. Radiation pressure noise (linked to power fluctuation in the cavity) could also be responsible for

frequency noise since it can affect the length of the IMC cavity and the angular control of the IMC end mirror if the beam is not well centered on this mirror. In linear regime, it has been shown that radiation pressure noise was not an issue for Initial Virgo sensitivity [423] and Advanced Virgo [141]. Specifications on this noise will have to be given for ET. Concerning input and output mirrors absorption, in order to avoid beam distortion induced by photothermal effect a low absorption fused silica with good homogeneity should be chosen as mirror substrate and coating absorption lower than 1 ppm is mandatory [234]. In order to cope with higher order Laguerre-Gauss modes, the resonant mode cleaner should be made with an even number of mirrors as explained in [63][155]. Cavity parameters (Finesse, Round-trip losses and cavity pole) will have to be defined according to the beam jitter, amplitude and frequency noise requirements at the interferometer input.

Due to the fact that a lot of things have been developed in the 1550 nm wavelength range for telecommunications, we should try to use as much as possible already existing components for the IMC of the ET-LF interferometers. For ET-LF, we have 2 possibilities to make a spatial filtering of the laser beam:

- use a resonant mode-cleaner as done in ET-HF
- use an optical fibre.

Some R&D activity is needed on this subject to see if the optical fibre is able to fulfill ET requirements. In any case, a resonant cavity will probably be needed at least to stabilize the laser frequency. The baseline solution remains to use two 20 meter long triangular cavity in series where we have more experience and now that this kind of suspended cavity should fulfill our requirements. As for ET-HF, IMC parameters should be defined according to beam stability, laser frequency and amplitude stability required at the interferometer input port.

Faraday isolator

Light back reflected by the interferometer should be picked up before being coupled back in the IMC cavities. The solution adopted in first and second generations of Gravitational wave detectors is to install a Faraday isolator in vacuum on the beam path between the interferometer and the Input mode cleaner cavity.

Faraday isolator for ET-HF: Faraday isolator design has evolved to cope with the increase of power between first and second generation detectors. An R&D program put in place at the European Gravitational Observatory has developed in collaboration with the Institute of Applied Physics (Nizhni Novgorod Russia) a Faraday isolator with reinforced magnetic field and using thermal depolarization compensation technique [302]. This isolator uses Terbium Gallium Garnet (TGG) as magneto-optic material and the design has been optimized for thermal depolarization, thermal lensing and Verdet constant change compensation [142]. This device is able to achieve very good isolation performances (>38dB) in vacuum from low power up to 250W laser power [232]. We could use this experience and the same kind of design and scale it up to get the expected performances of the Faraday isolator in the 1kW power range. For ET-HF we could expect that the in-vacuum Faraday isolator should have the following characteristics:

- withstand high average power (1kW) on long periods;
- an optical isolation higher than 30 dB at full power;
- residual thermal lensing higher than 100 m;
- provide good transmission (at least 95%)

Faraday isolator for ET-LF: In the telecom wavelength range, TGG cannot be used due to its higher absorption at 1550nm. Fortunately, in the field of telecommunications a lot of possible materials to be used in Faraday isolator are available [350]. In any case, as for the high power Faraday isolator needed for ET-HF, the development of vacuum compatible Faraday isolator for 1550 nm wavelength requires to build up a test facility and collaborative work with laboratories or companies having experience with free space Faraday isolator adapted to telecom wavelength. The relatively low power used in the configuration will probably simplify the design of such isolator with respect to the high power compatible one.

RF-Electro optical modulation system

In ET, RF modulation of the laser beam will be used in the control of the interferometer, both for longitudinal and angular controls.

RF modulation system for ET-HF: The main difference between the Electro Optical Modulation (EOM) system to be used in ET-HF respect to first and second generation detectors is the laser power that the EOM system will have to withstand (up to 1 kW for ET-HF). Thermal effects become more significant [344] and the choice of the appropriate material (electro-optic (EO) crystal) becomes crucial to limit as much as possible the consequence of these thermal effects on EOM properties. Indeed, it is important to select the right material not only to limit wavefront aberrations but also because it is a proof of local heating of the material. This heating can induce slow variation of the modulation index and disturb the ITF control. Requirements in ET for the electro optical modulation system (oscillator phase noise, modulation index and modulation index noise, ...) will have to be defined. Many of these parameters will affect the driving electronics and signal generator choice.

RF modulation system for ET-LF: The experience of telecommunication field should be used extensively in the RF-modulation system of ET-LF. It is likely that integrated fibered optical components will be used to modulate the laser light.

Other high power compatible components

The selection and development of high power compatible components suitable for ET-HF is essential. Experience acquired during AdV Highpower input optics R&D program should be a good starting point in the selection of waveplates, polarizers and for the design of High power low diffusing beam dumps [142, 232].

R&D work needed for ET

Laser and Injection optics of ET can benefit of the many years of R&D already performed by LIGO and EGO for respectively aLigo and Advanced Virgo projects in investigating high power compliant components such as electro-optical modulators, Faraday isolator. For ET, it is necessary to fund two R&D programs one focussed on ET-HF components that have to be compliant with high power laser and LG33 mode. The second one should concern ET-LF and the development and selection of IO components (Faraday isolator, EOM, Mirrors, waveplates and polarizers). Laser beam cleaning through a fiber has also to be studied for this configuration. Collaboration with experienced people (labs or companies) is essential in the success of these two R&D programs.

5.11 Detection system

Author(s): S. Hild, A. Thuering

5.11.1 Readout options for the gravitational wave signal

Figure 174 shows simplified schematics of three different readout methods applied to a basic Michelson interferometer. Usually Michelson interferometers used for gravitational wave detection are operated at a dark fringe⁹. The differential arm-length is controlled to give destructive interference at the output port; ideally no carrier light (f_c , red solid line) reaches the photo detector. The interaction of a gravitational wave with the Michelson interferometer can be considered as shortening of one interferometer arm, whilst the perpendicular one is elongated. This change of the differential arm length causes phase modulation sidebands, i.e. gravitational wave signal sidebands (blue dashed line). In contrast to the carrier light the gravitational wave signal sidebands interfere constructively at the beam splitter, exit the interferometer at its output port and finally reach the photo detector. The absolute frequency of the gravitational signal sidebands given is by $f_{\text{sig}} = f_c \pm f_{\text{gw}}$, where f_{gw} is the frequency of the gravitational wave (usually in the audio-band) and f_c the frequency of the main laser light (carrier). Since f_{sig} is a few hundred Terahertz, the photo diode cannot directly detect the gravitational wave

⁹Operating at the dark fringe has the advantage of providing good suppression of common mode noise and allows to make use of power recycling.

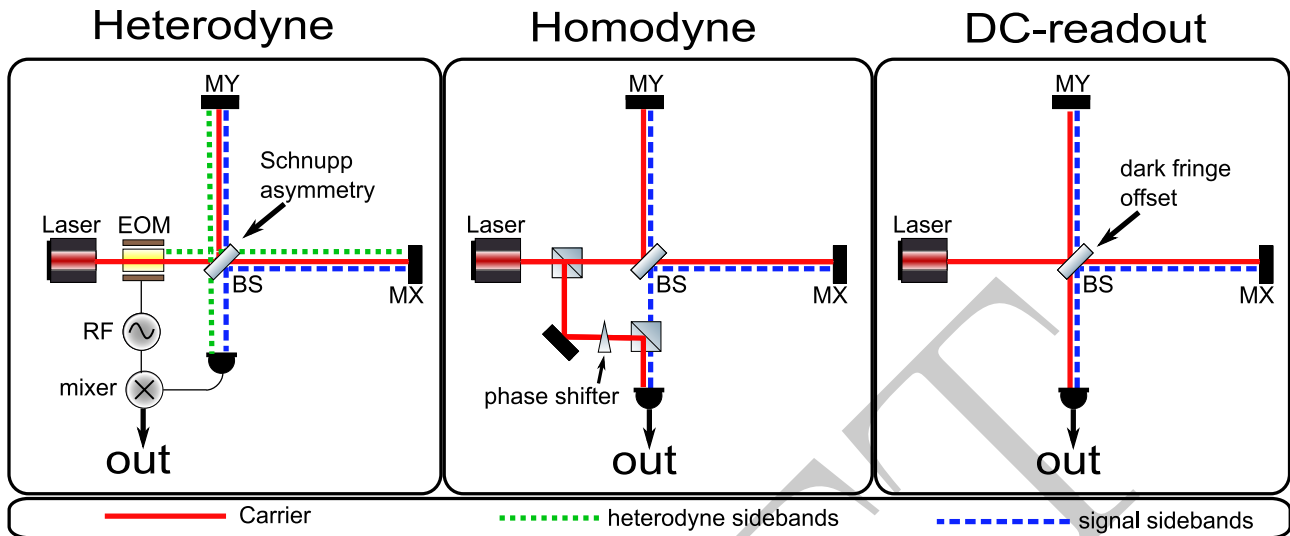


Figure 174: Illustration of three different readout methods of a Michelson interferometer: heterodyne, homodyne and DC-readout. A detailed explanation is given in the text.

signal, unless the presence of an optical local oscillator is provided. Heterodyne, homodyne and DC-readout use different concepts to ensure the presence of a low-noise optical local oscillator at the output port photo diode.

In the heterodyne schemes, commonly used by the first generation gravitational wave detectors, radio frequency (RF) sidebands (f_{het} , green dotted lines) are modulated onto the light at the input of the Michelson interferometer (Schnupp modulation [473]). Introducing a macroscopic arm length difference of several centimeter (so-called Schnupp asymmetry) allows the modulation sidebands to be transferred through the interferometer to the output port, where they serve as optical local oscillator for the gravitational wave signal. The photo-current produced by the beat between the different optical field components (optical demodulation) contains a radio frequency component at $f_{\text{het}} \pm f_{\text{gw}}$. In a second demodulation process the photo-current is then electronically demodulated at f_{het} (using a mixer) in order to finally derive a signal stream at f_{gw} .

In the homodyne readout scheme (center plot of Figure 174) a small fraction of the carrier light is split off in front of the interferometer and guided directly to the output photo detector without passing through the interferometer. The big advantage of this form of homodyne readout is that a phase shifter, placed in the local oscillator path, allows an easy change of the optical demodulation phase, i.e. the readout quadrature, without any hardware changes. On the other hand homodyne readout has the disadvantage that the length and the alignment of the local-oscillator path needs to be highly stable. In practice this usually implies that the local-oscillator path length as well as its alignment need to be actively stabilized by a low-noise control system, and all components of the local-oscillator path must be seismically isolated inside a vacuum system. Due to these demanding noise and hardware requirements, so far there have been no serious plans to change the readout scheme of the currently operating gravitational wave detectors from heterodyne to homodyne readout.

DC-readout is a special case of homodyne readout which is much easier to combine with the existing elements of currently used gravitational wave detectors. In a DC-readout scheme the operating point of the Michelson interferometer is slightly shifted off the dark fringe, by introducing a so-called *dark-fringe offset*, thus a certain amount of carrier light leaves the interferometer at the output port and can serve as local oscillator. Compared with the previously described homodyne readout, DC-readout has the advantage that no additional local oscillator path outside the main interferometer is required. On the other hand, DC-readout offers no easy way to vary the phase of the optical demodulation.

DC-readout was already used in the first ‘Michelson’ interferometer ever by Michelson and Morley in 1887 [361]. It is probably the simplest way to read out a Michelson interferometer, but was considered to be unsuitable for the first generation of gravitational wave detectors due to the strong coupling of laser power noise. However,

increased stability of the laser power inside future instruments gives hope for a renaissance of DC-readout for gravitational wave detectors, which was first proposed by Fritschel 2000 [222]. A demonstration of a DC-readout in a suspended prototype interferometer (without signal recycling) has recently been performed [448].

The next section briefly summarises the general advantages and disadvantages of DC-readout compared with heterodyne readout, especially taking into account the implications for an interferometer with tuned or detuned signal recycling [266].

5.11.2 Motivation for DC-readout

DC-readout has many advantages over the commonly used heterodyne readout:

1. When going from the currently-used heterodyne readout scheme to a DC-read scheme, the ratio of signal to shot noise will increase [130]. This is due to the fact that in the homodyne detection the shot noise contribution from frequencies twice the heterodyne frequency does not exist.
2. A reduced number of beating light fields at the detection port potentially reduces and simplifies the couplings of technical noise [266]. Especially the coupling of amplitude and phase noise of the heterodyne modulation is strongly reduced in a DC-readout scheme. In addition the frequency noise coupling to the gravitational wave channel is also expected to be reduced in DC-readout.
3. A simpler calibration procedure can be applied, because the GW-signal is present in a single data-stream even for detuned signal-recycling (and not spread over the two heterodyne quadratures as described in [265]).
4. As the main photo diode(s) and electronics for the detection do not need to be capable of handling RF signals, they can be simplified.
5. Large-area photo diodes¹⁰ may be used. These should offer reduced coupling of beam-pointing noise, due to decreased beam clipping and decreased influence of photo diode inhomogeneity (by averaging over a larger area).
6. As in the homodyne readout the local oscillator and the GW-signal pass the same optical system an optimal spatial overlap is guaranteed. (Due to thermal distortion current GW detectors employing arm cavities encountered the problem of imperfect spatial overlap of the carrier light (GW signal) and the heterodyne sidebands (local oscillator) [447])
7. Finally, the realization of a squeezed light enhanced interferometer is simpler using DC-readout rather than heterodyne readout. DC-readout requires squeezed light to be present only at frequencies in the GW signal bandwidth compared to heterodyne readout which requires squeezed light around twice the heterodyne frequency as well [545].¹¹

This long list of advantages has to be compared with the drawbacks of DC-readout. Even though power fluctuations of the carrier light (i.e. the local oscillator) are strongly filtered by the cavity poles of the power recycling cavity and the high-finesse arm cavities, the major disadvantage of DC-readout is an increased coupling of laser power noise. In addition there is the potential problem that the response from DC-readout is not completely linear, due to the operating point sitting on the near-quadratic slope close to the dark fringe. However, this should not be a significant problem as long as the mean deviation from the differential arm length operation point is not too large.

¹⁰RF photo diodes are required to have a low electrical capacitance.

¹¹A squeezed light source working only in the GW signal bandwidth would result in the DC-readout case in a sensitivity enhancement limited by the squeezing strength generated, whereas the same source would act in a heterodyne-readout based interferometer as if 50% of the squeezing was reduced due to losses. Hence, a sensitivity improvement by a factor of 6 dB in the DC-readout case would result in the heterodyne case in an improvement factor of only 2 dB.

5.11.3 Output mode cleaner

5.12 Main control and alignment strategies

Author(s): C. Graef, M. Mantovani, S. Hild

As a matter of fact, in interferometric GW detectors – the highly complex optical instruments they have grown – it is a crucial requirement for the multitude of their degrees-of-freedom (DOF) that they are held tightly at predefined operating points, to allow for full internal power build up, to enable active null operation, etc. ~~Provided this~~, the instrument can unfold its full potential for ultra high sensitivity measurements. To fulfill this requirement for stable lengths and frequencies, electronic feedback control has proven as an essential tool, making a deterministic and reliable operation of a GW detector possible.

The task of controlling an interferometer can further be sub-divided in the control of longitudinal DOF and alignment control. In the following three subsections we will focus on aspects of controlling the longitudinal degrees of freedom, i.e. only variations along the axis of the optical mode in the interferometer will be considered. Alignment control will be treated in Section 5.12.4.

5.12.1 Fundamentals of length sensing and control

A successful length sensing and control system for an interferometric GW detector has to satisfy three basic requirements: First, starting from a random initial state it must bring the instrument to a predefined operating point (“lock acquisition”). Second, it must prevent disturbances of any kind from causing deviations of the instrument from its operating point by an amount larger than specified. Finally, it must provide a low-noise electronic signal which contains the GW signal. In this discussion we will focus on the first two aspects.

A crucial element of a ~~successful~~ longitudinal control scheme is the extraction of a complete set of signals which reflect the dynamical state of the longitudinal degrees-of-freedom and which, in particular, are a measure for the deviation of each of the interferometric degrees-of-freedom from its desired operating point. Generally, this is achieved by employing variants of the fundamental Pound-Drever-Hall technique [194]. The Pound-Drever-Hall scheme builds on imprinting radio-frequency (RF) phase modulation sidebands on the carrier beam prior to its injection into the optical cavity to be controlled. Cavity length fluctuations are efficiently converted to carrier phase shifts, which occurs near resonance as a linear effect. The RF sidebands in contrast do not experience a phase shift, as their frequencies are generally chosen off-resonant in the cavity. Pure phase modulation is thus partially converted to amplitude modulation. Heterodyne readout of the reflected beam provides a signal which is a direct measure for the cavity’s deviation from resonance and which can further serve as an error signal for electronic feed back controls.

Ideally, a sensing system would provide a number of independent outputs, one for each DOF in the detector. However, in practice error signals obtained from an interferometer by means of heterodyne detection show more or less strong coupling. This is acceptable as long as these signals are at least linearly independent, due to the fact that this class of signals can be electronically post-processed, i.e. linearly transformed, resulting in separated signals. The underlying transforms can easily be implemented in the form of matrices in digital data processing systems. However, care must be taken to provide ~~robustness~~ of the transformations under parameter changes of the optical plant and the sensing electronics. This is why in practice optically separated signals are usually preferred over signals obtained via electronic separation. Further potential disadvantages of electronically separated signals are a reduced signal-to-noise ratio and more complex dynamics during lock acquisition [464]. Generally, providing too few modulation frequencies or extraction ports complicates the task of finding a set of independent length signals and, in the worst case, leaves the optical system underconstrained due to a lack of information about its internal state.

A valuable form of description for the design of a sensing scheme is the *sensing matrix*. The sensing matrix describes the ~~relation~~ between the interferometer’s degrees-of-freedom and the signal extraction ports. In the ideal case this matrix would be ~~diagonal~~ which would read as all sensing signals being fully decoupled. Likewise,

the control problem would decouple to a single-input single-output problem for each degree-of-freedom in the interferometer. Contrasting this, the signal mixing of length error signals one encounters in practice would yield non-vanishing off-diagonal elements in the sensing matrix. This is tolerable, as long as the off-diagonal elements are smaller in magnitude than the diagonal ones as in this case a technique referred to as *gain hierarchy* can be applied to solve the control problem. This technique is based on suppressing a large signal that appears in more than one port by closing a control loop around the DOF that causes it. A small signal, previously covered by the large one, can in this way be dissected from the signal mixture and serve as an error signal for another, by then uncontrolled, degree-of-freedom.

The classical approach of implementing servo controllers by means of analog electronics is driven from predominance more and more by digital control systems. At the expense of their higher cost and obvious bandwidth limitation, digital systems provide a high precision and low noise environment allowing for rapid design and easy duplication of solutions. Massively multiple-input multiple-output systems become feasible and instrument automation can be easily implemented. Unlike analog electronics digital servo systems exhibit a high immunity to environmental parameter changes which makes them predestinated for applications which require long-term stable operation. Despite all these obvious advantages, it is fair to say that digital system complexity, in practice, rivals analog controls.

5.12.2 Longitudinal sensing and control in Advanced generation detectors

With increasing complexity and a growing number of degrees-of-freedom in the instruments comes the need for highly sophisticated length sensing and control schemes, which are substantial to setting the detector into operation. The interferometric topology that will be adopted by the Einstein Telescope is the cavity-enhanced dual recycling Michelson interferometer, which is also the underlying topology of the Advanced GW observatories currently under construction. In this section a review of central aspects of the sensing and control concepts of a typical Advanced generation GW observatory is given, focussing on Advanced LIGO [22] as an example. The optical setup is schematically depicted in Fig. 175.

For Advanced LIGO different modes of operation are foreseen, each of them involving e.g. different input laser power levels, signal recycling tunings, homodyne detection phases, etc., to yield optimum signal-to-noise ratio, depending on the cosmological source under investigation [8]. The main differential control requirement for Advanced LIGO is 10^{-15} m rms, yielding a shot noise limited sensitivity of 4×10^{-21} m/ $\sqrt{\text{Hz}}$.

At the detector's operating point the carrier laser light is resonant in the power recycling cavity (PRC) and in the arm cavities. The signal recycling cavity (SRC) is tuned to carrier resonance only if the detector is operated in tuned mode. Two pairs of phase modulation sidebands, locked by a PLL, are imprinted on the input laser, forming the basis of the sensing scheme. The frequencies were chosen to be $f_1 = 9$ MHz and $f_2 = 45$ MHz, both nearly anti-resonating in the arms to reduce arm-cavity induced phase shifts.¹² Both pairs of modulation sidebands are resonant in the power recycling cavity. The signal recycling cavity, however, is arranged to be nearly resonant for the f_2 sidebands while the f_1 sidebands do not resonate.

A typical property of the recycling cavities is their potential to cause mixing of modulation sidebands which immediately leads to coupled error signals. To prevent this effect from rendering the control scheme more complicated than necessary it is crucial to arrange for a configuration that reduces this mixing to the largest possible extent.

The Schnupp asymmetry – a macroscopic offset in the arm lengths of the central Michelson – is set to 5 cm to provide nearly critical coupling of the f_2 sidebands in the dual recycling cavity, with the implication of simultaneous resonance of the power recycling and the signal recycling cavities for this sideband frequency. By choosing an appropriate value for the Schnupp asymmetry one can arrange for a large modulation sideband power ratio in the SRC, providing improved signal separation. In this case the resulting power ratio is of the order of 10^3 , in favor of the f_2 sidebands.

¹²This turns out to have a positive effect on the shot noise sensitivity of the Michelson (MICH) degree-of-freedom.

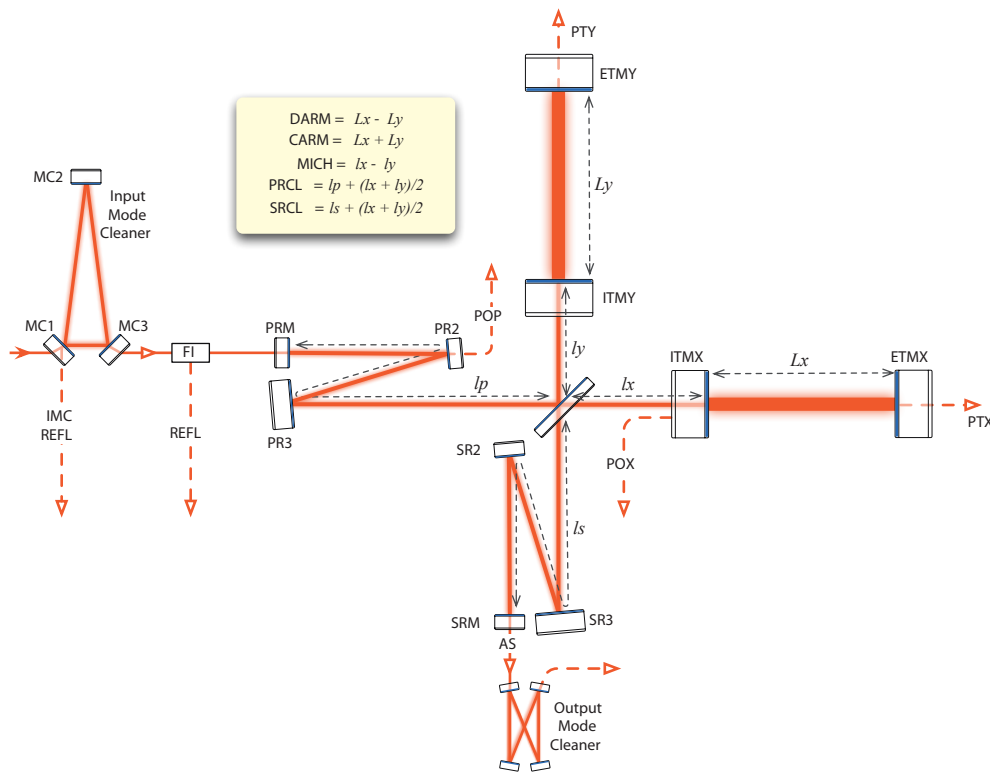


Figure 175: Schematic drawing of the Advanced LIGO optical layout, degrees-of-freedom and sensing ports [8]. Error signals for the control of the five longitudinal degrees-of-freedom are extracted from the four ports REFL, AS, POP and POX.

A variety of ports in the interferometer are read out to obtain a complete set of control signals for all longitudinal degrees-of-freedom. Besides the asymmetric port (AS), signals are extracted from the symmetric port (REFL) and from pick-off ports from within the power recycling cavity (POP) and a reflection of one of the arm cavities (POX). These beams are directed to photodetectors and the resulting signals are in turn demodulated at f_1 , f_2 , $f_2 - f_1$ or $f_1 + f_2$, at appropriately set demodulation phases. Demodulation at the sum or difference frequency of two modulation sidebands, i.e. at their beat frequency, is a key concept in modern interferometric control system design and is often referred to as *double demodulation*.

The signal obtained in the symmetric port, after demodulation at the lower sideband frequency f_1 is used for common mode arm cavity (CARM) control. Consequently, the differential arm cavity mode control signal is obtained in the asymmetric port from the AS DC photodetector. For the DC readout scheme of the asymmetric port, which also contains the GW signal, a differential arm length (DARM) offset of the order of 10^{-11} m will be applied, yielding a DC power level in the asymmetric port of the order of 0.1 W of carrier light. The intra-cavity POP port yields signals for the PRC and the Michelson degrees-of-freedom, after demodulation at f_1 and f_2 , respectively.

For controlling the signal recycling cavity, the optimum signal extraction port as well as the demodulation frequency depends on the mode of operation, i.e. the tuning of the SR cavity. Whereas for zero detuning an appropriate error signal can be extracted in the symmetric port in reflection of the interferometer or at the arm cavity pick off port, for detuned operation analyses have shown that double demodulation of the asymmetric port signal yields better error signals. Thus, if it is desired to continuously tune the SR from tuned mode to a detuned science mode, at a detuning of about 5 deg it is necessary to switch between error signals for the control of the signal recycling cavity.

The underlying sensing matrix shows well-separated error signals for the arm cavities' degrees-of-freedom. The power recycling cavity is sufficiently decoupled from the other degrees-of-freedom but shows strong coupling to the ports where the Michelson and signal recycling cavity error signals are obtained. The most worrisome degrees-of-freedom are the Michelson phase and the signal recycling cavity which exhibit comparably large amount of cross-coupling. However, control of the interferometer can be gained i.e. with a gain hierarchical approach in conjunction with the arm length stabilization system (ALS) which is discussed in Sec. 5.12.3.

The control signals derived from the error signals are applied to the end mirrors in the case of the DARM degree-of-freedom, to the beamsplitter for Michelson phase feedback and to the recycling mirrors for SR and PR length stabilization. However, the common mode arm cavity length control loop is the most elaborate one. The CARM error signal is fed back to the main laser via multiply cascaded frequency loops, providing the final level of frequency correction. The required unity gain frequencies of the servo controllers are of the order of tens of Hz for PRC, SRC and MICH, hundreds of Hz for DARM and tens of kHz for the CARM degree-of-freedom.

With the exception of the arm cavity common mode controller all servo loops are realized using digital controls. The more demanding (in terms of bandwidth) CARM servo will be implemented in analog electronics. The digital feedback loops are implemented in a custom-made real-time control system with typical sampling rates of up to 65536 samples per second at up to 18 bit resolution. Digital control systems have proven to be a powerful solution with high flexibility. Complex filter structures, e.g. with blending of sensors and signals, can be conveniently realized and changed on-the-fly with little effort.

Similar to the initial LIGO control scheme, correction paths are included in the Advanced LIGO scheme. Correction signals are filtered copies of sensing noise limited MICH and SRCL control signals. To cancel the effects of known couplings, correction signals are fed from SRCL to DARM and from MICH to DARM at a precision of 1%. An additional correction path will feed signals from PRCL to DARM, at a lower precision of 10%.

5.12.3 Detector lock acquisition

Lock acquisition is the process of bringing an interferometer from its uncontrolled, initial state to a controlled state in which the instrument is fully operable. As in a GW detector lock acquisition has a direct impact on its duty cycle, this subject demands attention as early as the design phase of the instrument. Contrasting the case of a servo loop operating near resonance, where the error signal for an optical cavity shows a linear response to length changes, during lock acquisition one has to generally deal with highly nonlinear signals. Servo loops are usually optimized for control on resonance, resulting in a poor performance during acquisition. The determining quantity in lock acquisition of an optical cavity system are the mirrors' relative velocities. Further, the *threshold velocity* is usually referred to as a measure which quantifies the performance of an acquisition scheme. By definition the threshold velocity is the maximal relative velocity of two cavity mirrors below which lock acquisition is successful. The threshold velocity strongly depends on the bandwidth of the underlying control loop. Only if the servo response time is sufficiently short to follow the transient error signal it is capable of "capturing" an optic. As the probability for all DOF being simultaneously at their operating points is very small, a sequential approach must be taken, bringing the DOF to the locked state one after another.

The simplistic approach to lock acquisition, e.g. practiced in the early detector prototypes, is to wait for the instrument's DOF, driven by random ground motion, to move close to their operating points and then swiftly engage the control loops. As with this method lock acquisition of an interferometric GW detector would be a pure matter of coincidence more deliberate approaches were strongly desired. For initial LIGO an acquisition algorithm was developed which is based on a real-time estimate of the time-evolving sensing matrix, derived from measurable signals during lock acquisition [204]. With the implementation of this scheme on the LIGO digital control and data system lock of the detector was on average acquired on timescales of ~ 1 min. The Virgo approach to lock acquisition was to effectively decouple the instrument's DOF which is achieved by a deliberate misalignment of optics. This technique is often referred to as *variable finesse locking* [20]. Lock was usually acquired within a few minutes.

The Advanced LIGO quadruple suspension provides isolation to the test masses with respect to ground motion at

frequencies above 10 Hz. Even though the active internal seismic isolation (ISI) platforms provide additional low frequency isolation, low frequency disturbances are expected to cause significant test mass displacement of the order of $10^{-7} \text{m}/\sqrt{\text{Hz}}$ at 0.5 Hz. This is due to the fact that at the suspension system's resonance frequency or at lower frequency perturbations are not well attenuated and couple into the test masses' positions as displacement noise. Besides this, the test masses will have electrostatic actuators instead of coil-magnet actuators which were used in initial LIGO. Electrostatic actuators deliver lower actuation noise, at the expense of significantly lower actuation force they can exert on the test masses. The Advanced LIGO electrostatic actuators are expected to saturate at forces of $\sim 200 \mu\text{N}$ [62]. This severely complicates the process of lock acquisition.

In order to ease the difficulties of lock acquisition in the Advanced detector generation, auxiliary laser based schemes will be employed to complement the well-established techniques. This discussion focusses on the Advanced LIGO ALS (arm length stabilization) system [203]. For Advanced Virgo it is anticipated to employ a similar scheme. Other systems to aid lock acquisition, that were considered for use in Advanced LIGO, such as the suspension point interferometer or digital interferometry are described in [493]. The underlying idea of ALS is to provide for more deterministic lock acquisition by locking the arm cavities independently of the remaining degrees-of-freedom. The ALS system builds on frequency doubled laser beams launched into the arm cavities through the end test masses for pre-stabilization of the interferometer arms, independent of the science laser circulating in the interferometer. By applying additional coatings on the arm cavity mirrors the properties of the arm cavities, as seen from the ALS, can be shaped in accordance to the pre-stabilizations scheme's requirements. The choice of reflectivities for the input mirror and the end mirror results in an overcoupled cavity for the auxiliary laser, seen from the end mirror. The Finesse of the arm cavities for the 532 nm ALS beams is ~ 100 . A simplified schematic of the ALS principle setup is depicted in Fig. 176.

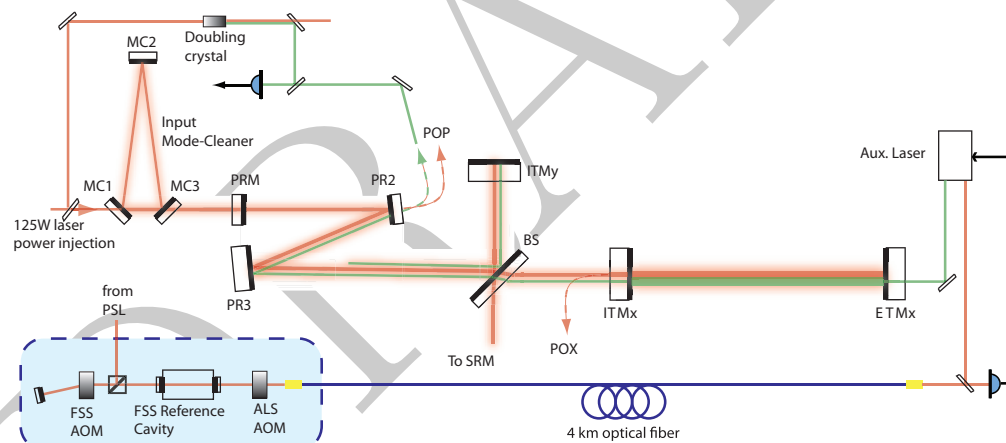


Figure 176: Schematic drawing of the Advanced LIGO arm length stabilization (ALS) subsystem [203]. The test mass motion is reduced prior to lock acquisition by a combined scheme of PDH reflection locking of an auxiliary laser to the arm cavities and heterodyne detection of the transmitted beams. The optical fiber is necessary to provide an optical reference at the end stations, to lock the auxiliary lasers' phases to the science laser.

The initial step in the acquisition process is to hold the arm cavities on anti-resonance for the main science laser. In the next step the recycling cavities are brought to the locked state, before the ALS brings the arm cavities onto resonance with the main laser and hands over the control authority to the global interferometer sensing and control scheme. For effectiveness, the ALS must reduce the residual arm cavity length fluctuations to a displacement of no more than one cavity line width, which is approx. 1.3 nm in the case of the Advanced LIGO arm cavities. Estimations have shown that with ALS engaged a level of displacement fluctuations of 0.115 nm rms can be reached.

Technically, once the arm cavities are locked with the 532 nm beams, a heterodyne measurement is performed on the ALS beam transmitted by the x-arm cavity and a frequency doubled sample of the main laser beam. A second one is performed between the x-arm and the y-arm transmitted beams. These measurements yield

common and differential mode error signals which are in turn fed back to the corresponding actuators. By introducing a tunable offset into the heterodyne locking loop, the arm cavities can thus be adjusted to arbitrary tunings.

For a smooth transition from ALS arm cavity control to global control a robust phase-locked loop (PLL) is crucial, to provide a well-defined phase relationship between auxiliary lasers and the main science laser. Once the PLL is closed, the auxiliary lasers are locked to the arm cavities using PDH reflection locking. The resulting control signal acts on a voltage-controlled oscillator (VCO) which supplies the electronic local oscillator for the PLL. In this way the offset frequency of the auxiliary laser with respect to the reference is tuned. An analog servo is foreseen for this loop and is expected to have a bandwidth of a few kHz.

To provide a stable frequency standard for the auxiliary laser PLL, a technique based on the LISA (Laser Interferometer Space Antenna) back-link measurement is employed. Mullavey et al. [373] have experimentally demonstrated a scheme based on counter propagating two laser beams through an optical fiber and subsequent measurements of each of the outputs with LISA-style phasemeters. By subsequent combination of the output signals an error signal can be obtained which can be utilized to eliminate fiber induced phase noise. Their setup consisted of 4.6 km single mode optical fiber and two Nd:YAG lasers – operated in a master-slave configuration. To circumvent nonlinear forms of noise such as stimulated Brillouin scattering, the transmitted laser power was reduced to $\sim 50 \mu\text{W}$. In the underlying bench top experiment a relative frequency noise of $0.5 \text{ mHz}/\sqrt{\text{Hz}}$ was reached for Fourier frequencies between 5 Hz and 20 Hz which is well below the Advanced LIGO requirements, with a margin of more than an order of magnitude.

5.12.4 Angular control - Automatic Alignment control system

The angular control system has to be implemented in order to reduce the mirror misalignments in the frequency region in which the seismic attenuation system does not fulfill the alignment requirements, i.e. below the mechanical resonances, to reduce the fluctuations of the mirror angular positions with respect to the beam, to maintain the overall alignment of the optical elements, ensuring long data taking periods, and to reduce the noise at the dark fringe port. The mirror angular positions in data taking mode can not be locally controlled because the long term drifts of the local references spoil the overall alignment. After the lock has been acquired the angular control has to be switched to a global control system, the *Automatic Alignment*, which uses error signals coming from the interferometer itself with a modulation-demodulation technique based on differential wave front sensing. The control scheme chosen for the second and third generation of gravitational wave interferometer is a Ward-like scheme where the sideband modulation frequencies are chosen to do not have any any sideband and higher order modes resonating in the cavities [370].

The main differences between the third generation and the first generation of gravitational wave detectors, which are already commissioned, are: the presence of stable Recycling Cavities; the higher circulating power; and the presence of the Signal Recycling cavity. These modifications produce an improvement in the interferometer stability and sensitivity but an increase of complexity for the development of the Automatic Alignment control system.

Stable Recycling cavities issue

The stable recycling cavities reduce the higher order modes content to be less affected by the point of view of thermal effects. This behavior influences the Automatic Alignment control system since the amplitude of the alignment error signals is proportional to the amount of the $\text{TEM}_{01/10}$ modes. For example in the case of the recycling cavity with a Gouy phase of 15 deg the TEM_{01} mode is attenuated by a factor of about 6 while for 25 deg the attenuation factor is about 9. For this reason the choice of the recycling cavity Gouy phases has to be done taking into account both the stability requirements and the amount of first order higher order modes to ensure the angular controllability of the system.

High circulating power issue

In a high power interferometer the *radiation pressure* plays an important role. The light beam acts on the mirror such as an optical spring with strength increasing with the power. The higher effect would be in the long

arm Fabry-Perot cavities, since there the higher amount of light power is stored, but the effect has to be also evaluated on the central interferometer mirrors.

The circulating power inside the arm interacts with the suspended mirrors via radiation pressure. The two cavity mirrors become coupled and their angular motion must be described in terms of two linear combinations [489]. When the circulating power becomes large enough one of the angular modes can become dynamically unstable.

As derived in [489], the interaction of beam and mirror can be written in term of the stiffness matrix:

$$\mathbf{k} = \frac{2PL}{c(1 - g_1g_2)} \begin{bmatrix} -g_2 & 1 \\ 1 & -g_1 \end{bmatrix} \quad (207)$$

where $g_i = 1 - L/R_i$ are the G-factors of the two mirrors. The eigenvectors and eigenvalues of the stiffness matrix determines the physical angular degrees of freedom and the corresponding stiffness applied to the mechanical system.

The normal stable situation corresponds to a positive stiffness of the system, given by the contribution of the mechanical stiffness of the mirror suspension and the extra-stiffness due to the radiation pressure, which gives a resonance made of a pair of complex poles with negative real part and quite large quality factor. The case of negative stiffness instead leads to an unstable system described with two real poles, one with positive and one with negative real part, with very close absolute frequency. The radiation pressure effects have then to be taken into account in the design of the control system.

Moreover the presence of the Signal Recycling mirror increases the number of degrees of freedom to control with respect the first generation of gravitational wave interferometers.

The design of the Automatic Alignment control system will be challenging because of the above mentioned issues and of the control accuracy and noise requirements to reach the ET sensitivity. From the other hand all these effects and problematics will be studied for the commissioning of the second generation interferometers, as Advanced Virgo and Advanced LIGO, gaining experience to deal with all these difficulties.

5.13 Thermal effects and their compensation

Author(s): V. Fafone, A. Rocchi

5.14 Rough cost evaluation

Author(s): A. Freise and H. Lueck

The maximum size for Suprasil 3001 is the advanced LIGO size of 40kg. The heavier substrates for ET can only be made either of Suprasil 3002 which has inhomogeneities in the direction of the beam or from fused pieces of thinner Suprasil 3001. The price quoted by Heraeus for a substrate of 600mm in diameter and 400mm in thickness made of composite Suprasil 3001 is 700000 Euro.

At present Silicon is only available in Chzochalski grown crystals to a size of up to ??? 450mm, the maximum resistance available for this type is ??? In Floating zone crystals the maximum size at present is 200mm. The interest of the semiconductor industry in ultra-pure crystals is very limited and will most likely not drive the development of bigger size single crystals.

Costs of silicon are comparable to the one of ultra-pure fused silica.

The cumulative costs can be obtained from table ...

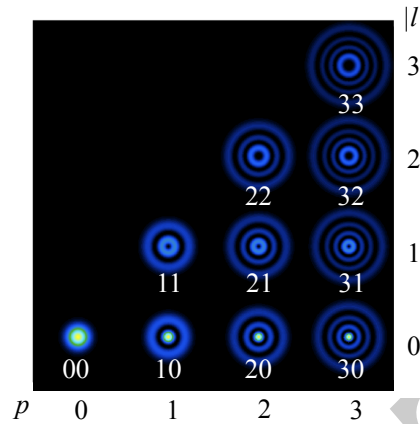


Figure 177: Power distributions of LG_{pl} mode. p is the radial mode index ($p \geq 0$), and l is the azimuthal mode index. The power distribution of LG_{00} mode is equivalent to that of the conventional HG_{00} mode.

5.15 Technologies to be developed/RND

Author(s): K. Kokeyama, S. Hild, A. Thuering, J. Franc, R. Nawrodt

5.15.1 Thermal noise reduction due to the LG modes

Author(s): K. Kokeyama

Since ET HF interferometer targets the gravitational waves at lower frequencies where the mirror thermal noise dominates (30 - 300 Hz) the sensitivity, the thermal noise should be removed. Higher-order Laguerre-Gauss (LG) mode beams have been proposed and investigated for the reduction of mirror ~~the~~ thermal noise for the ET HF interferometer [372, 546]. LG modes are solutions of the paraxial wave equation in cylindrical coordinates, in a similar way to the Hermite Gaussian modes which are the solutions in Cartesian coordinates. They have radial power distributions as shown in Fig. 177 which are more uniform than those of the conventional fundamental mode (LG_{00} or TEM_{00} mode). Therefore, higher-order LG mode beams allow to reduce the thermal noise without introducing higher clipping-losses. Although flat-top and conical beams have been proposed for future gravitational-wave detectors, higher-order LG mode beams have the strong advantage that they have ~~the~~ spherical wave fronts, and so should be compatible with conventional optics such as spherical mirrors and lenses. On the other hand, flat-top and conical beams require non-spherical complex mirrors. Such mirrors were tested and found not to satisfactory for the requirement of angular alignment issues [466] and they are difficult to manufacture with the current technology.

Previous investigations  shown that the LG_{33} beam can realize a factor of seven smaller power spectral density of displacement equivalent coating Brownian thermal noise in comparison to the fundamental LG_{00} mode [157]. In addition, higher-order LG beam are fully compatible with the conventional length and angular sensing signals. This fact indicates that changing over from the fundamental mode to the higher-order LG mode should not require any new control strategy. Ref. [157] analyzed the control signals using numerical simulation tools and found that the performance of the LG_{33} beam in tilt-to-longitudinal phase coupling, generation of angular control signals, and the corresponding control matrices, was equivalent to or better than that of the LG_{00} beam.

LG mode technology for gravitational wave detectors is currently in a transition phase from the theoretical and simulation investigation to the experimental investigation phase. The first table-top experiment has been demonstrated the generation of a LG_{33} beam and the mode cleaner cavity performance with the generated LG_{33}

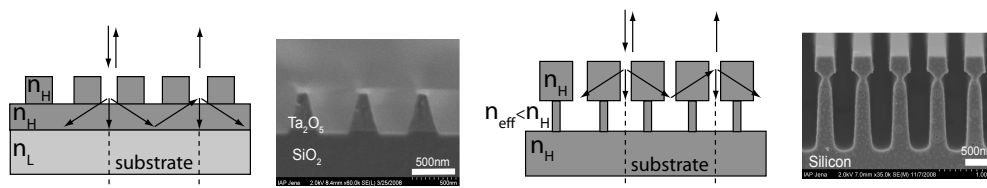


Figure 178: Single layer and monolithic waveguide grating architectures.

beam [223]. The LG_{33} beam was generated by converting the LG_{00} beam to LG_{33} beam using a computer-controlled liquid-crystal-on-silicon spatial-light modulator (SLM). The PDH error signal was properly obtained with LG_{33} beam, and successfully used to control the longitudinal degree of freedom of the mode-cleaner cavity. The mode purity of the generated LG_{33} beam was increased from 66% to 99% upon transmission through the linear mode cleaner, demonstrating that very high-purity LG_{33} mode light sources can be produced in this way. Further experimental investigations, such as diffractive optical elements instead of SLM for the higher generation efficiency, are underway in order to determine the suitability of the technique for the ET HF interferometer.

One must note a practical problem which is the mode degeneration of higher-order beams. Several modes of (l, p) exists being the same order, $2|l| + p$, and they have identical Gaussian beam parameters, such as radius of curvature and Gouy phase. Therefore these modes can all resonate in the same mode-cleaner cavity, and not be rejected or cleaned away. They may contaminate the purity of the desired mode and may require a higher quality of a mirror surface deviation. It does not happen for the fundamental mode, since there is only one mode the in zeroth order.

5.15.2 Coating research

Author(s): I. Martin, R. Nawrodt

current and ungoing plans on coating research, correlation between loss and microscopic structure, including optical properties (absorption, scattering, etc.)

5.15.3 Waveguide grating mirrors

Author(s): D. Friedrich

Test mass mirrors used in gravitational wave detectors are subject to several sources of thermal noise. A dominant contribution is given by Brownian thermal noise caused by mechanical loss of the high reflective multilayer coatings. These conventionally are made of up to 20 double layer of tantala (Ta_2O_5) and silica (SiO_2) each having a quarter wavelength optical thickness. Hence, concepts for a reduction of the mechanical lossy materials or for coating free mirrors are investigated to provide alternative mirror architectures in order to improve a detector sensitivity in its mid frequency band. For this purpose broadband waveguide grating (WG) structures have been proposed [123], which are based on resonant excitation of light fields in a nanostructured surface that theoretically allow for a perfect reflectivity under normal incidence without implementing multilayer stacks.

The basic principle of WGs is shown in Fig.178 using a ray picture [452].

WGs are basically constructed of a substrate with low index of refraction n_L and a nanostructured layer having a higher index of refraction n_H . The grating can be designed that only specular reflection and three transmitted orders exist. The first order beams in the nanostructured layer are totally reflected at the substrate and partially coupled out at the surface. By adjusting the grating dimensions (optical properties) the outcoupled light fields can be forced to interfere constructively giving a perfect reflectivity. For dielectric materials Rigorous-Coupled-Wave Analysis (RCWA) [367] is a numerical method to investigate the optical properties of WGs depending on

their material and geometrical parameters and was used to optimize waveguide gratings in terms of parameter tolerant designs.

It was found that even a zero waveguide layer thickness (only ridges on top of a substrate) can show high reflectivity [123], which has experimentally been demonstrated using tantala ridges on a silica substrate for the prominent wavelength of 1064 nm [120]. The fabricated waveguide grating (see Fig. 178) was incorporated as a coupling mirror into a linear Fabry-Perot cavity together with a conventional high-reflectivity mirror. From the measured finesse of ≈ 660 the reflectivity of the waveguide grating was determined to be $(99.08 \pm 0.05) \%$.

Recent theoretical work [120] has shown that also monolithic waveguide grating structures are feasible by directly etching a T-shaped structure into a substrate (see Fig. 178). Here, the lower grating is chosen to have a small enough fill factor (ratio of groove width to grating period) to act as an effective medium, namely having a lower index of refraction than the material used. This structure has been fabricated based on a silicon substrate aiming at a high reflectivity for a laser wavelength of 1550 nm. Therefore two etching steps were applied. In a first step the upper grating was defined via anisotropic etching and then protected on its sidewalls. Afterwards an isotropic etching was used to realize the low fill factor grating beneath. The reflectivity was determined in a table-top cavity setup to be $(99.79 \pm 0.01) \%$ [121] in full agreement with numerical simulations (RCWA) [367].

While the thermal noise models for conventional multilayer coatings and material parameters are well studied, the thermal noise performance of nanostructured surfaces is still to be investigated. It was experimentally shown that a nanostructured surface does not affect the mechanical quality of a substrate significantly [381]. However, the mechanical loss and other material parameters such as thermal conductivity of a nanostructure need to be further investigated in order to estimate the actual level of thermal noise. Also a direct measurement of thermal noise of a WG compared to a multilayer coating is of great interest.

Further, the fabrication process needs to be improved to meet the requirements for test masses used in gravitational wave detectors. Besides the optical quality in terms of high reflectivity and homogeneity over the grating area, techniques have to be developed to handle actual substrate dimensions. One approach being investigated is the bonding of a thin nanostructured waver on a thick substrate.

5.15.4 Speedmeter topology

Author(s): K. Kokeyama and H. Mueller-Ebhardt

As was reviewed in Section 5.4, speed meters are considered as the ET interferometer due to the strong advantage to surpass the quantum noise limit broadly in the low frequency region. However, few practical experience of speed meter technology has been accumulated, in contrast to well-studied Michelson-interferometer (MI) -type position-meter with currently operated gravitational-wave detectors. Practical speed meter characterization such as quantum noise surpass-ability and a capability to optical losses have to be examined in order to select the ET topology.

Speed-meters are realized by either MI-type or Sagnac-interferometer (SI) -type topology, and only few part of them is experimentally demonstrated:

Michelson-interferometer type A typical configuration of a MI type speed meter [426, 427] is depicted in the left panel in Fig 179. The configuration employs an RSE interferometer with the sloshing cavity at the anti-symmetric port. The south port of the RSE part is kept to be the dark fringe (destructive interference between the north and east arms). When the end mirror of one cavity moves, some light goes through to the south port, and enter into the sloshing cavity. The light comes back from the sloshing cavity and enter the RSE part from the south port. This field is 180 degrees different in phase and cancel the position information leaving only the phase shift proportional to the relative velocity of test masses. The sloshing cavity adds more complexity such as the length and alignment degrees of freedom to be controlled, compared with an RSE topology whose technology is mature and already being installed in, e.g., Advanced LIGO, therefore, it is necessary to examine the practical capability of ET.

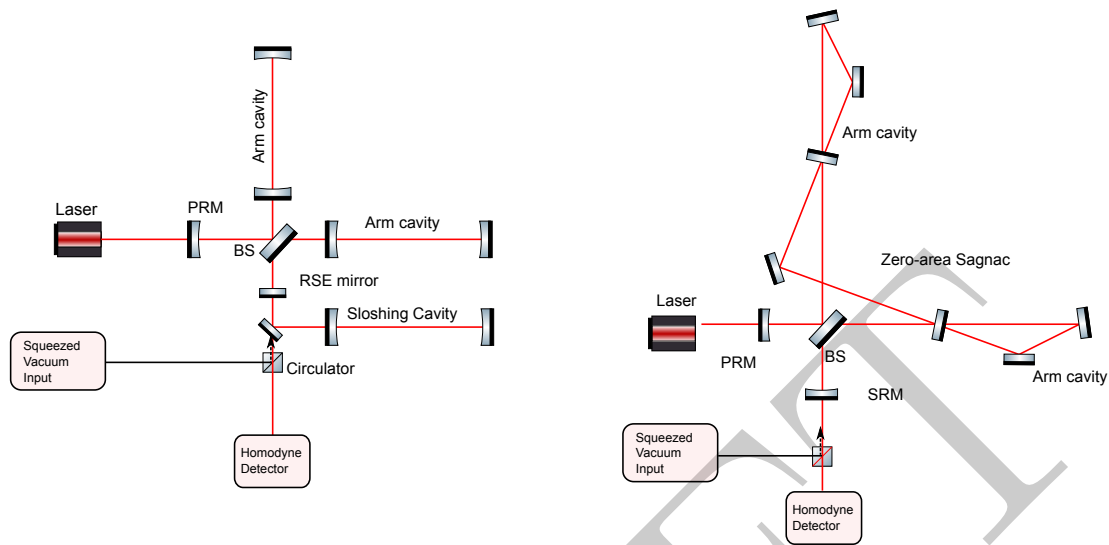


Figure 179: Left panel: An example configuration of a Michelson-interferometer-type speed meter. Right panel: A typical configuration of a Sagnac-interferometer-type speed meter with two ring cavities.

Sagnac-interferometer type The SI-type speed meter [158] is depicted in the right panel in Fig 179. A SI is a more straightforward way to realize a speed meter than the MI-type. A basic SI is a ring interferometer (see, the middle panel in Fig. 143 in Section 5.4) and it is a speed meter by itself. The laser light is split into two paths by a beam splitter, then one of the two light fields propagates the ring path in the clockwise whereas the other in counter-clockwise. These two fields interfere at the same beam splitter. The two fields experience the same path but at the different timing depending on the path differences. Therefore the interference intensity depends only on the time depending part of the test masses. For an ET topology, a zero-area SI in which the area enclosed by the two counter-propagating beams is zero, will be preferable because it is insensitive to the interferometer rotation.

Before one realized that the speed meter is free from the quantum back-action noise, Sagnac interferometer has been investigated as a candidate topology for the ground based gravitational-wave detectors. The shot-noise-limited phase sensitivities were demonstrated by [501] and [?] at high or low frequency region, respectively.

The squeezed-vacuum will be necessary to be injected from the dark port to enhance the ability for surpassing the SQL in the broadband frequency region. This technique has been already demonstrated experimentally for a zero-area Sagnac interferometer by a table-top experiment [201]. The non-classical sensitivity improvement of up to 8.2 dB with a simple zero-area Sagnac interferometer was experimentally verified.

5.16 Appendix

5.16.1 Optics properties data base

refractive index at 1064 nm, 1550 nm, dn/dT (T), absorption, etc.

The following two subsections might move directly into 5.9. Otherwise overview here and values at selected temperatures in main part of the section.

5.16.2 Mechanical properties of optical materials

Authors: R. Nawrodt, J. Franc, etc.

summary of mechanical data (TN relevant parameters) used for TN calculation parameters: Young's modulus, mechanical loss,...

bulk materials: fused silica, sapphire, silicon coatings: latest results on room temperature and cryogenic coating measurements (contrib. from *I. Martin*, ET note *J. Franc et al.* [215], *R. Nawrodt et al.* [382])

5.16.3 Thermal properties of optical materials

Authors: R. Nawrodt, J. Franc, etc.

summary of thermal properties used for the heat extraction estimates parameters: thermal conductivity, heat capacity, thermal expansion,...

Comparison of values and reasons for the selection of certain values at given temperatures (e.g. thermal conductivity [280])

DRAFT

6 Overall budget and timeline considerations

The evolution toward the Einstein Telescope observatory has been, is and will be a long path. After a series of preliminary activities supported by the European Commission within the Framework Programme 6 (FP6), this conceptual design study is currently funded under FP7.

Although the efforts and the attention of the worldwide GW scientific community are currently focused on the realisation of the advanced detectors (Advanced LIGO, Advanced Virgo and LCGT), the activities devoted to the third generation must continue with increasing speed. In Fig. 180 the expected evolution of the GW detectors in the World is shown. The last line of the table shows the long path still in front of the European project ET. After the current conceptual design study phase, a preparatory phase is expected to be necessary to define the technological details, and the legal and organizational issues. The start of construction (2018–2019) is expected to occur after the first detection of GWs, which is reckoned to happen within at most one year after the advanced detectors will have reached their nominal sensitivity. The construction and commissioning phase is expected to be of about 6–7 years of intense activity, before collecting the first science data with the Einstein Telescope ET. In table 181 the cost summary and the time distribution of the expenditures are shown.

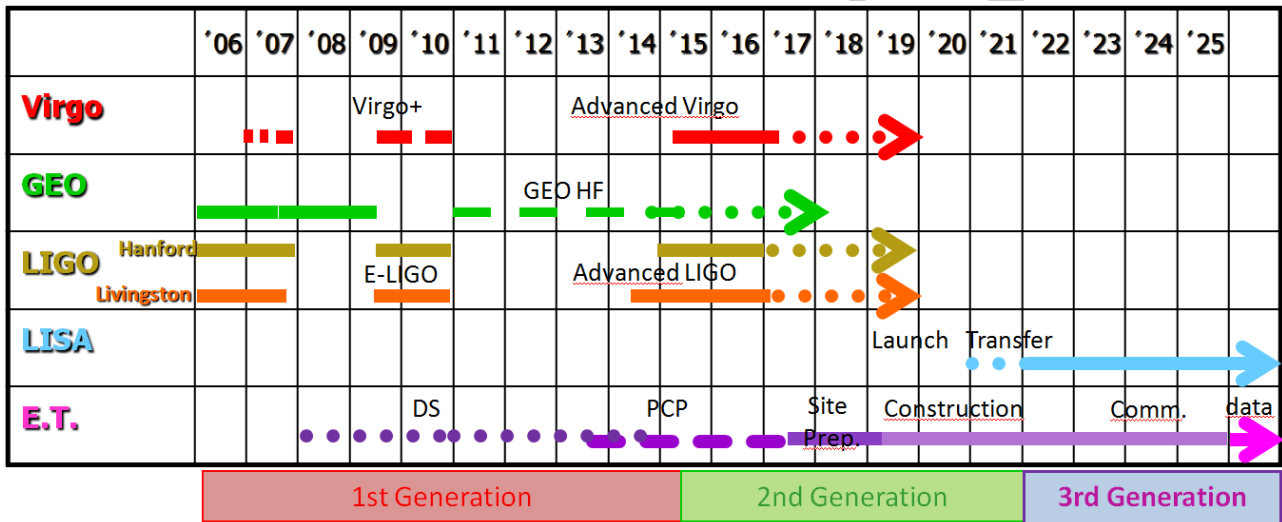


Figure 180: Roadmap for the evolution of some of the GW detectors in the World. In the last line the expected evolution of the third generation observatory ET (Einstein Telescope) is shown. After the current conceptual design phase (DS), and before the construction, a preparatory construction phase (PCP) is expected, where the detailed technical, legal and organization aspects of the project will be defined. In the evolution timeline of the Virgo and LIGO detectors are shown the (current) Virgo+ and E-LIGO phases, corresponding to a limited upgrade of the initial interferometers, with input laser power increased by about a factor 2–3 and other technical improvements preparatory of the “advanced” phase. The time evolution of the Japanese interferometers (TAMA, LCGT, DECIGO) and of the other projects like ACIGA in Australia are not plotted.

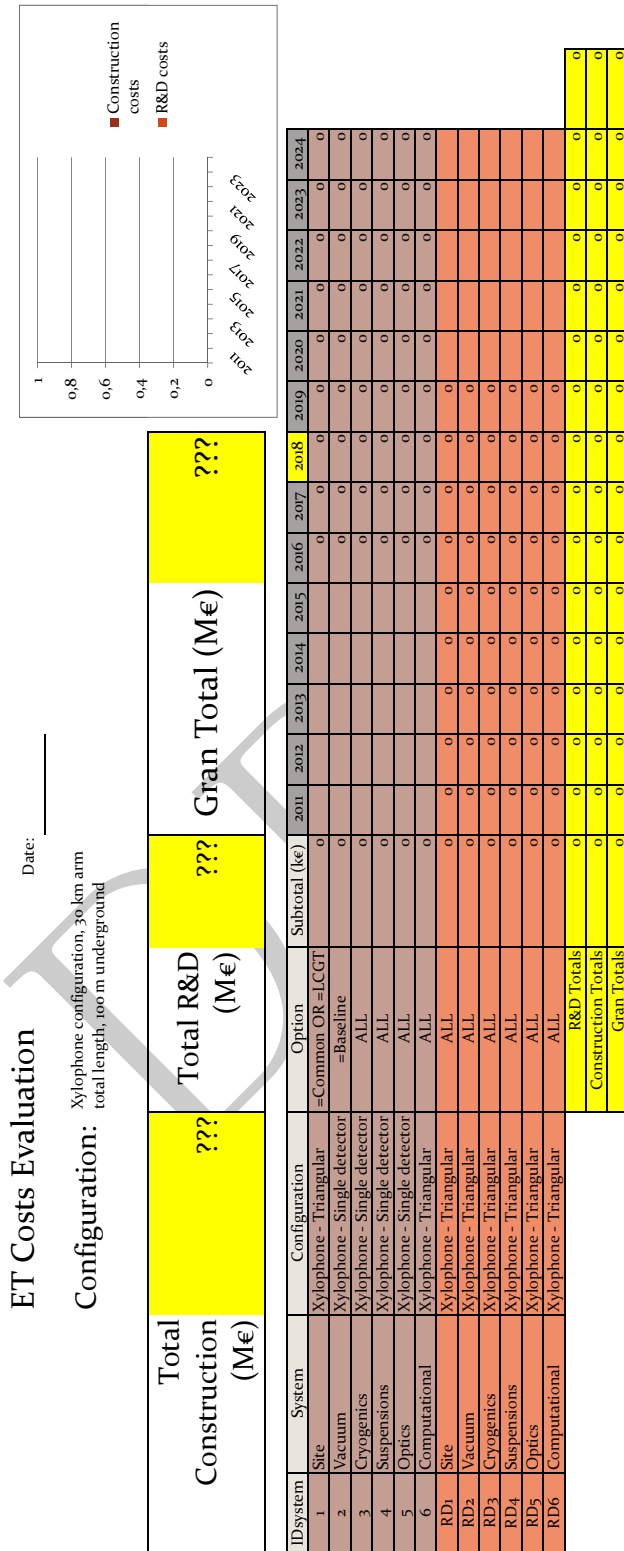


Figure 181: Cost summary and time distribution